2009

Biotextured Nanocrystalline Materials with Superhydrophobic Surfaces and Controlled Friction and Wear

Mehdi Shafiei
University of Windsor

Follow this and additional works at: http://scholar.uwindsor.ca/etd

BIOTEXTURED NANOCRYSTALLINE MATERIALS WITH SUPERHYDROPHOBIC SURFACES AND CONTROLLED FRICTION AND WEAR

by

Mehdi Shafiei

A Dissertation
Submitted to the Faculty of Graduate Studies
through Engineering Materials
in Partial Fulfillment of the Requirements for
the Degree of Doctor of Philosophy at the
University of Windsor

Windsor, Ontario, Canada
2009

APPROVED BY:

Dr. G. Botton, External Examiner
McMaster University

Dr. S.H. Eichhorn
Department of Chemistry & Biochemistry

Dr. D.O. Northwood
Department of Mechanical, Automotive & Materials Engineering

Dr. A. Edrisy
Department of Mechanical, Automotive & Materials Engineering

Dr. A.T. Alpas, Advisor
Department of Mechanical, Automotive & Materials Engineering

Dr. B. Budkowska, Chair of Defense
Department of Civil & Environmental Engineering

04 May 2009

DECLARATION OF CO-AUTHORSHIP/
PREVIOUS PUBLICATION

I. Co-Authorship Declaration

I hereby declare that this thesis does not incorporate material that is result of joint research. In all cases, the key ideas, primary contributions, experimental designs, data analysis and interpretation, were performed by the author and Dr. A.T. Alpas as advisor.

I certify that, with the above qualification, this thesis, and the research to which it refers, is the product of my own work.

II. Declaration of Previous Publication

This thesis includes 6 original papers that have been previously published/ submitted for publication in peer reviewed journals/conference proceedings, as follows:

Thesis Chapter	Publication title/full citation	Publication status
Chapter 2	M. Shafiei and A.T. Alpas, Friction and Wear Mechanisms of Nanocrystalline Nickel in Ambient and Inert Atmospheres, Metallurgical and Materials Transactions A38 (2007) 1621-1631.	Published
Chapter 3	M. Shafiei and A.T. Alpas, Effect of Sliding Speed on Friction and Wear Behaviour of Nanocrystalline Nickel Tested in an Argon Atmosphere, Wear 265 (2008) 429-438.	Published
Chapter 4	M. Shafiei and A.T. Alpas, High-Temperature Friction and Wear Mechanisms of Nanocrystalline Nickel Composite Coatings, Surface & Coatings Technology.	To be submitted
Chapter 5	M. Shafiei and A.T. Alpas, Friction and Wear Behaviour of Nanocrystalline Cobalt, Proceedings of the STLE/ ASME International Joint Tribology Conference, San Diego, CA, USA, October 2007, Paper # 44131.	Published
Chapter 6	M. Shafiei and A.T. Alpas, Fabrication of Biotextured Nanocrystalline Nickel Films for the Reduction and Control of Friction, Materials Science and Engineering C28 (2008) 1340-1346.	Published
Chapter 7	M. Shafiei and A.T. Alpas, Nanocrystalline Nickel Films with Lotus Leaf Texture for Superhydrophobic and Low Friction Surfaces, Applied Surface Science.	To be submitted

I certify that I have obtained a written permission from the copyright owner(s) to include the above published material(s) in my thesis. I certify that the above material describes work completed during my registration as graduate student at the University of Windsor.

I declare that, to the best of my knowledge, my thesis does not infringe upon anyone's copyright nor violate any proprietary rights and that any ideas, techniques, quotations, or any other material from the work of other people included in my thesis, published or otherwise, are fully acknowledged in accordance with the standard referencing practices. Furthermore, to the extent that I have included copyrighted material that surpasses the bounds of fair dealing within the meaning of the Canada Copyright Act, I certify that I have obtained a written permission from the copyright owner(s) to include such material(s) in my thesis.

I declare that this is a true copy of my thesis, including any final revisions, as approved by my thesis committee and the Graduate Studies office, and that this thesis has not been submitted for a higher degree to any other University or Institution.

ABSTRACT

This study aimed to develop new wear-resistant materials with superhydrophobic surfaces and low friction by combining the high strength of nanocrystalline (NC) materials with the biological surface textures. This goal was accomplished in three stages.

First, the tribological properties of electrodeposited NC Ni and NC Co were studied, and the role of the oxide-rich tribolayers in reducing the friction and wear rates was delineated. For the NC Ni, micromechanisms of wear in different testing environments were characterized, and the sliding-speed sensitivity of friction and wear rate was investigated. A modified Archard equation was proposed to predict the wear rates of NC Ni as a function of grain size and sliding speed. Additionally, it was found that the high-temperature wear resistance of NC Ni could be improved by using SiC nanoparticles as reinforcements.

In the second stage, NC Ni replicas of the surface textures of a lotus leaf and a snake skin were fabricated through replication and electrodeposition. The NC Ni snake skin replica displayed anisotropic frictional properties, due to the asymmetric shape of the protrusions at the scales' ridges. The NC Ni lotus leaf replica featured a high density of microscale conical protuberances that prompted a 30% lower peak coefficient of friction (COF) compared to a smooth surface, due to a smaller real area of contact.

In the third stage, the surface texture of the NC Ni lotus leaf replica was modified using a short-duration electrodeposition process that increased the radius of the protuberance tips, followed by a perfluoropolyether (PFPE) solution treatment that reduced the surface energy and resulted in a multi-level surface roughness consisting of a nanoscale surface texture superimposed on microscale protuberances. The produced

surfaces had a high water contact angle of 156°, similar to that of the natural lotus leaf, and had a 60% lower steady-state COF.

DEDICATION

I would like to dedicate this dissertation to my parents for their unconditional love, support and encouragement.

ACKNOWLEDGMENTS

TABLE OF CONTENTS

LIST OF TABLES

LIST OF FIGURES

CHAPTER 2

CHAPTER 3

CHAPTER 4

CHAPTER 5

CHAPTER 6

CHAPTER 7

LIST OF ABBREVIATIONS

ARB	accumulative roll-bonding
ASTM	American society for testing and materials
BSE	backscattered electron
COF	coefficient of friction
COF_p	peak coefficient of friction
COF_{ss}	steady-state coefficient of friction
CVD	chemical vapour deposition
DSC	differential scanning calorimetry
ECAP	equal channel angular pressing
EDS	energy dispersive spectroscope
FCC	face centred cubic
FIB	focused ion beam
FTMP	friction thermomechanical processes
GB	grain boundary
HCP	hexagonal close-packed
HPT	high pressure torsion
HV	Vickers microhardness
IDB	incidental dislocation boundaries
LB	lamellar boundaries
MC	microcrystalline
MEMS	micro-electro-mechanical systems
MP SiC	microparticles of SiC
NC	nanocrystalline
NP SiC	nanoparticles of SiC
NSERC	natural sciences and engineering research council of Canada
PED	primary electrodeposition
PEMFC	proton exchange membrane fuel cell
PFPE	perfluoropolyether
PVD	physical vapour deposition
R_a	roughness

RH   relative humidity

SAED   selected area electron diffraction

SE   secondary electron

SED   secondary electrodeposition

SEM   scanning electron microscopy

SMAT   surface mechanical attrition treatment

SPD   severe plastic deformation

TEM   transmission electron microscopy

USSP   ultrasonic shot peening

XRD   X-ray diffraction

NOMENCLATURE

a_c	radius of projected contact area
a_c'	actual radius of projected contact area
A'	cross-sectional area of indentation
A^{real}	real area of contact
B_M	half peak breadth
B_S	instrumental broadening
c^2	dimensionless parameter to account for oiling-up and sinking-in
C	effective elastic modulus
d	grain size
D	counterface ball diameter
E	elastic modulus
f	frictional force
f_{air}	fractional contact area between liquid and air
f_S	fractional contact area between liquid and solid
h	indentation depth immediately before partial unloading
h_c	indentation contact depth
h_c'	actual indentation contact depth
h_f	residual depth after complete unloading of indenter
h_i	indentation depth extrapolated to zero load along linear fit of upper one-third of unloading curve
h_{max}	maximum indentation depth
H	hardness
H_0	single crystal hardness
k	constant for grain boundary strengthening
K	wear coefficient
n	strain hardening exponent
N	sliding cycles
P	applied normal load (Chapters 1,2,3); ploughing component of frictional force (Chapter 6)
r	counterface ball radius (Chapters 2,3,4); roughness ratio (Chapter 7)

r_{ind}	indenter radius
R	wear track radius
S	shear component of frictional force
v	sliding speed
V	volumetric wear loss
w	wear track width
W	wear rate
W_0	grain-size independent component of wear rate
α	wear exponent
γ_{sv}	solid-vapour surface energy
γ_{sl}	solid-liquid surface energy
γ_{lv}	liquid-vapour surface energy
δ	elastic depth recovery ratio
θ	peak's Bragg angle (Chapters 2,3); actual contact angle (Chapter 7)
θ_T	thermodynamic contact angle
λ	X-ray wavelength
μ	coefficient of friction
ν	Poisson's ratio
σ_0	lattice frictional stress
σ_H	Hertzian stress
σ_y	yield strength
τ	shear strength

CHAPTER 1

INTRODUCTION

1. GENERAL OVERVIEW

Nanocrystalline (NC) materials provide great potential for improving the performance and extending the capabilities of products in many industrial sectors, because of novel properties that mostly originate from a large volume fraction of grain boundaries [1-3]. It is known that dislocation nucleation and motion are both necessary for plastic deformation, but activation of dislocations in grains smaller than 100 nm can be difficult. As a result, the mechanical behaviour of NC materials is characterized primarily by high strength and hardness [4-7], and limited ductility [7,8].

The increase in strength and hardness that accompanies grain refinement is appealing from the tribological point of view, particularly when designing new materials and surfaces with improved friction and wear properties. There is a clear need for experimental work to characterize micromechanisms of wear in NC materials, and to rationalize microscopic processes leading to generation of wear debris or surface damage. In examining the wear behaviour of NC materials attention should be given to the role of testing atmosphere as the NC materials have a larger density of grain boundaries that can accelerate the surface oxidation process. Therefore, the role of surface oxidation during sliding wear and its effects on wear damage is of interest. Besides, the high density of grain boundaries can cause strong strain-rate sensitivity in NC materials, resulting in an unusual sensitivity to slight changes in sliding speed. Thus, the effect of sliding speed on the friction and wear mechanisms of NC materials must be studied to achieve a

comprehensive analysis. In addition, the large fraction of grain boundaries in NC materials may make these materials unstable at elevated temperatures, and therefore, it is important to also investigate the wear mechanisms of these materials at elevated temperatures. More details on the effects of surface oxidation, strain-rate sensitivity and thermal instability on the tribological performance of NC materials are presented in Section 2 of this chapter.

On the other hand, it is known that biological organisms maintain their unique surface properties by employing mechanisms that cannot be explained using simple linear theories of friction and adhesion. The complex surfaces of these organisms are capable of controlling friction, adhesion and wettabilty through a combination of surface structure, surface chemistry, flexibility, and active interface control [9]. Hence, adapting these mechanisms for fabricating novel engineering surfaces with enhanced properties (such as superhydrophobicity and low friction) is a promising technological trend. The challenge, however, is how to combine the advantages of a hard, wear-resistant material with the exceptional hydrophobicity or frictional properties of a biological organism in a single surface designed to function in an engineering system.

The current study proposes a method for producing a new group of wear-resistant materials with superhydrophobic surfaces and controlled frictional properties, by combining the high strength and hardness of NC materials with the surface texture of certain biological systems. The proposed method consists of two steps:

i) replication of the biological surface texture on a cellulose acetate film to obtain a negative impression of the texture; and

ii) electrodeposition of the NC material on the acetate film to obtain a hard replica of the biological surface texture.

The result is a self-sustaining NC film with a surface texture that simulates that of the selected biological system.

Along these lines, this dissertation is organized in eight chapters. Chapter 1 is an introduction to the entire dissertation that starts with a general overview and an outline of the objectives and methodologies used in the following chapters. It then reviews the main methods for the production of NC materials and the microstructure's role in mechanical and tribological behaviour of these materials. This chapter also presents examples of biological systems in which friction, adhesion and wettability are controlled through adaptation of specific surface textures.

Chapter 2 characterizes friction and wear mechanisms of an NC Ni in comparison with an MC Ni, to understand the micromechanisms responsible for the NC Ni's tribological behaviour. Coefficients of Friction (COF) and wear rates are measured in ambient air and argon environments using a pin-on-disc tribometer. The role of the oxide-rich tribolayers in the friction and wear mechanism of this NC metal is delineated, and microscopic processes leading to generation of wear debris and surface damage in different testing environments are characterized in detail.

The sliding-speed dependence of the COFs and the wear rates of the NC Ni and the MC Ni studied in Chapter 2 are characterized in Chapter 3. The sliding wear tests are performed in an argon environment under a constant normal load but at different sliding speeds. Additionally, the deformation behaviour of the NC Ni and the MC Ni surfaces are studied using a nanoindentation system.

Chapter 4 reports on the production of NC Ni composite coatings reinforced with micro and nanoparticles of SiC. The objective of this chapter is to investigate whether SiC particles as reinforcements could improve the high-temperature friction and wear properties of NC Ni. The COFs and wear rates of the NC Ni coatings reinforced with the SiC particles are measured at 298 and 493 K, using a high-temperature pin-on-disc tribometer. The cross-sectional microstructures of the worn surfaces are studied using focused ion beam (FIB) and transmission electron microscopy (TEM) techniques.

Chapter 5 presents a study of the tribological behaviour of NC Co as a metal with a lattice structure that differs from that of the NC Ni. The friction and wear properties of an NC Co are studied in comparison with an MC Co using pin-on-disc tests in ambient air.

Chapter 6 details the method developed in this research to produce NC Ni films with the surface textures similar to those of biological systems. The objective of this chapter is to produce hard replicas of certain biological surfaces to reduce or control the friction. For this purpose, two types of biological surface textures (i.e., a lotus leaf and a boa's skin) are replicated on a cellulose acetate film, on which an NC Ni coating is electrodeposited to obtain self-sustaining replicas of the biotextures. The frictional properties of the NC Ni lotus leaf replicas are measured using a pin-on-disc tribometer. The COFs of the NC Ni snake skin replicas are measured using an instrumented microscratch tester with a Rockwell-type diamond indenter tip.

Chapter 7 explains the fabrication of biotextured NC Ni films with superhydrophobic and low friction surfaces. NC Ni replicas of lotus leaf are produced using replication and electrodeposition methods described in Chapter 6. A short-duration, secondary electrodeposition process is used to modify the morphology of the protuberances,

followed by a perfluoropolyether (PFPE) solution treatment. Water contact angles and COFs of the textured films are measured and compared to those of smooth NC Ni surfaces.

The final chapter of this dissertation, Chapter 8, is a summary of the preceding chapters and the main conclusions arising from this dissertation.

2. NANOCRYSTALLINE MATERIALS

2.1. Production of Nanocrystalline Materials

NC materials can be produced using a large number of methods that include electrodeposition, severe plastic deformation (SPD), crystallization of amorphous solids, consolidation of nanopowders, physical vapour deposition (PVD) and chemical vapour deposition (CVD). Among these methods, electrodeposition and SPD techniques are widely used in the production of dense NC metals.

<u>**Electrodeposition**</u>

Electrodeposition can be used to produce NC metals with a controlled grain size [10]. The processing parameters for this method include the electrolyte's basic chemical composition, the addition of grain nucleators, stress relievers and grain-growth inhibitors, the PH value, the deposition temperature, the current density, and the type of current cycles [10,11].

Electrodeposition can be used with conventional or modified electroplating baths to produce large parts with sufficient thickness in hours. The specimens produced by this method are fully dense, and their textures can be controlled through the process parameters. It is a relatively inexpensive, room-temperature technology that can easily be developed for mass production [12].

The main disadvantage of this method, however, is the limited thickness of the products that results from deposit peeling prompted by accumulated stress [12].

Severe Plastic Deformation

Very large deformations can be obtained by using SPD methods at relatively low temperatures [13], which create complex stress states, straining patterns and dislocation configurations, in addition to high densities of the geometrically necessary dislocations that lead to grain refinement [8].

High pressure torsion (HPT), equal channel angular pressing (ECAP), and accumulative roll-bonding (ARB) are the best-known methods for providing large plastic deformations and nanostructure formations. Schematics of these techniques are presented in Figures 1a-c. For many metals, these methods can lead to grains as fine as 20 nm and dislocation densities as high as $5 \times 10^{14} \text{ m}^{-2}$ [14].

An NC surface layer can be produced without affecting bulk properties, by limiting the extent to which plastic deformation is applied to a material's surface. The techniques employed to achieve this goal are generally referred to as surface nanocrystallization, and include ultrasonic shot peening (USSP) [15], surface mechanical attrition treatment (SMAT) [16,17], and friction thermomechanical processes (FTMP) [18].

Lu et al. [17] placed spherical steel balls with smooth surfaces and a diameter of 8 mm into a reflecting chamber that was oscillated by a vibration generator. The system's high frequency (20 kHz) means that the surface is impacted by a large number of flying balls over a short period of time (Figure 2a). The repeated, multidirectional impacts impose complex stress states at high strain rates onto the sample's surface, and cause severe plastic deformations that induce grain refinement in the entire surface. According to their observations, the SMAT treatment provides an effective approach for forming a nanostructured layer on metallic surfaces.

Shinoda et al. [18] modified the surfaces of some Al alloy castings using an FTMP technique, in which a non-consumable rod is forced against the specimen's surface while rotating (Figure 2b). The frictional force introduces stress into the surface, and the frictional heat makes it plasticise. As a result, the microstructure is refined due to dynamic recrystallization. According to their observations, the porosity in the modified layer was completely removed, the segregation of Cu and Si was considerably reduced, and the hardness of the surface layer increased due to grain refinement during the FTMP.

2.2. Microstructure of Nanocrystalline Materials

Microstructure of Nanocrystalline Metals Produced by Electrodeposition

Finer microstructures and higher dislocation densities can be obtained through electrodeposition, compared to SPD techniques [19]. Depending on the application of the NC material, it is possible to modify the processing parameters to enhance the microstructural characteristics. For example, instead of adding grain refiners like saccharin, which usually results in a high concentration of sulphur in the deposits [20], it is possible to prevent grain growth by rotating the substrate at a high speed [21].

Electrodeposited NC metals and alloys are usually textured, and contain microstrain in their crystalline lattice [21]. The texture mainly depends on the composition of the material and the processing parameters, such as the type of current cycle [21]. In contrast, the microstrain is proportional to the deposit thickness [12]. These microstructural features can be measured using X-ray diffraction (XRD) technique [22].

The relationship between the crystalline structures of the electrodeposited NC material and the substrate is another factor that influences the microstructure and the

grain morphology [23]. For example, the slight mismatch between the lattice constants of Cu (substrate) and Ni (deposit) produces a characteristic lamellar structure that consists of micro-twins within the grains [23]. No micro-twins have been observed in electrodeposited Ni or Cu on a Ti substrate, because the lattice constants and crystal structure of the deposits and substrate are so different [23]. Figure 3 shows the microstructure of an electrodeposited NC Ni sample [19].

Microstructural Evolution in Severe Plastic Deformation Methods

Lloyd et al. [24] investigated the structure of some heavily cold-worked Al alloys, and observed the evolution of a subgrain structure as they increased the strain in the studied alloys. According to their report, the subgrain size decreased sharply up to a strain of 1.0, and then more slowly over the subsequent strain range. Figure 4 shows the variation in the subgrain diameter with strain in different Al alloys. They also reported a misorientation in the range of 2-20 degrees across subgrains at the largest strains (2.5), but did not present a detailed analysis of the misorientation distribution with strain.

Heilmann et al. [25] employed a block-on-ring test configuration to determine the orientation of subsurface cells generated by sliding in Cu. They observed large plastic strains and large rotation angles in subsurface cells after very short sliding distances. According to their report, after a sliding distance of 12 m (100 cycles) under a normal load of 66.6 N and at a sliding speed of 1 cm/s, a substructure of elongated cells containing crystallites as small as 3-30 nm formed in the region immediately under the surface, but the authors did not present a theory that explains the formation of these ultra-fine crystalline particles. As the depth increased, cell sizes became larger, cell walls

9

became wider, misorientation between the adjacent cells decreased, and dislocation networks appeared within the cells. They also observed and measured the rotation of the cells (as a result of surface deformation) around an axis normal to the sliding direction and parallel to the interface. The cell rotation was maximum at the interface, and increased as the number of sliding cycles increased. Figure 5 shows the cell rotation as a function of the subsurface depth after 1 cycle, and then after 100 cycles of sliding [25].

It has been suggested that high strains introduce a lamellar or subgrain structure with boundaries of different misorientation angles [26]. Experiments have shown that deformation-induced, high-angle boundaries are common to a diverse set of materials and conditions [27]. A detailed description of the microstructural evolution during SPD of metals has been presented by Hughes et al. [27]. They employed convergent beam Kikuchi patterns to assess the orientations of individual crystallites, and found that the ratio of the deformation-induced, high-angle boundaries to the original grain boundaries was significantly large.

Figure 6 provides a schematic drawing of grain subdivision in small and large strains [27]. According to this figure, increasing the strain prompts dislocation boundaries to evolve from a typical cell block structure into a lamellar structure that is oriented in the direction of material flow. Continued deformation leads different slip system combinations to operate within each original grain, resulting in dislocation accumulation processes. As a result, complex dislocation boundaries form, and grains subdivide into regions with different texture components [27]. Increasing the strain leads to the rotation of these small individual crystallites towards the preferred end textures [28]. Since the preferred end textures differ by very large misorientations, this process can lead to the

formation of high-angle boundaries. Therefore, grain subdivision followed by texture evolution can result in a large fraction of high-angle boundaries in a severely deformed metal, which produces a deformation-induced grain refinement [27].

Figure 7a shows a TEM micrograph of the dislocation microstructure developed during cold rolling in pure Ni. A well-developed structure of lamellar boundaries and cell blocks has formed after a 90% cold reduction [29]. Figure 7b shows a schematic drawing of a large-strain dislocation structure that features sheets of extended lamellar boundaries (LB) with incidental dislocation boundaries (IDB) bridging between them [29].

2.3. Properties of Nanocrystalline Materials Influencing Tribological Behaviour

Strength, Ductility and Strain-Rate Sensitivity

Since the early works of Hall [30] and Petch [31], experiments have shown that reducing the grain size of metals and ceramics increases their yield strength, according to the well-known Hall-Petch equation:

$$\sigma_y = \sigma_0 + kd^{-0.5} \tag{1}$$

where σ_0 is the lattice frictional stress, d is the grain size, and k is a constant for the grain boundaries' contribution to the strength.

Since the hardness (H) is related to the yield strength (σ_y) of the material, by [32]:

$$H = 3\sigma_y \tag{2}$$

a similar relationship can be expected between the hardness and grain size of polycrystalline materials.

Farhat et al. [6] produced NC Al coatings with grain sizes in the range of 15-100 nm, using an RF magnetron sputtering technique. They observed that the relationship between

the hardness and the grain size of the NC Al obeyed the Hall-Petch equation, much like other polycrystalline materials. More specifically, the grain boundaries continued to contribute to the material's strength, even down to grain sizes as small as 15 nm. Other studies [33-36] on the hardness of NC materials have shown an increase in hardness by a factor of 5-7 when the grain size decreased from the micrometer range to the nanometer range. However, the Hall-Petch relationship is only valid down to a critical grain size of about 14 nm [33,37]. Below this critical grain size, each grain cannot contain more than one dislocation, and therefore the dislocation pile up mechanism is not applicable [37]. Therefore, the mechanical properties of NC materials are mainly controlled by the grain-boundary-induced deformation mechanisms rather than by the plasticity of the crystals due to dislocation movement [38,39]. It is also important to note that the strength of nanostructured materials is determined not only by crystallite size, but also by misorientation across the crystallite boundaries [40].

Since microstructural refinement leads to a great improvement in a material's hardness, one can expect an improvement in the wear resistance as well, according to Archard's law of wear [41]:

$$W = K \frac{P}{H}$$
(3)

where W is the volume of material worn per unit sliding distance (wear rate), P is the applied load, H is the hardness, and K is the wear coefficient. The literature has thoroughly documented that both the coefficient of friction (COF) and the wear rate are lower in specimens with higher surface hardness values [16,37,42], because as the surface hardness increases, the plastic deformation and microplowing are considerably

reduced so that the contacting solids can slide with a reduced amount of energy expenditure [16,42]. As a result, both the COF and the surface damage decrease.

While, the COF peak and the severe wear rate at the initial stage of sliding are usually higher in softer materials, the steady-state COF and wear rate are less sensitive to the hardness of the original surface, because the formation of hard tribolayers increases the surface hardness at the later stages of sliding [43,44].

NC materials often exhibit low tensile ductility at room temperature, which limits their applications, but experiments have shown that NC materials with high tensile ductility can be produced using the SPD techniques [8,39]. For example, a 30% uniform elongation and 65% elongation to failure were observed when samples of pure Cu were subjected to a special thermo-mechanical treatment (Figure 8) [8]. This treatment resulted in a bimodal grain size distribution with microcrystalline (MC) grains embedded inside a matrix of NC grains. According to the Hall-Petch relationship, the NC matrix provides the high strength of the material [42,45]. Meanwhile, the MC grains induce strain hardening mechanisms [46,47] that lead to a high tensile ductility.

Zhang et al. [39] measured the tensile ductility of NC Zn, and reported a relatively high tensile ductility compared to an MC Zn. According to their report, the high tensile ductility probably originated from the strain accumulating potential of the larger grains, and the grain boundary sliding mechanism of the smaller grains. They suggested several possibilities for enhancing tensile ductility, including increasing strain hardening and strain-rate sensitivity, activating other deformation mechanisms like twinning or stacking faults, and inducing grain boundary sliding to prevent the formation of pores along the grain boundaries and triple junctions.

Surface ductility is an important factor in determining the wear resistance of a material [48]. It is widely accepted that delamination wear is usually associated with subsurface crack propagation [49]. Alpas and Embury [50] reported that crack initiation and propagation along the shear bands was the main mechanism of delamination wear in ductile materials. This mechanism can play an important role in the wear behaviour of NC materials produced by the SPD methods, because shear bands form during the microstructural evolution in these materials [27].

Plastic deformation mechanisms in NC materials, include grain boundary sliding and dislocation emission at grain boundaries [22,51-53]. Since these mechanisms are time-dependent, the deformation of NC materials becomes increasingly difficult at higher strain rates, leading to notable enhancements in yield strength [54-58]. An increase in the sliding speed is expected to cause an increase in the rate of the application of the shear strain to the contact surface. This suggests that a slight change in sliding speed may have a great influence on the tribological properties of NC materials. The role of sliding speed on the friction and wear behaviour of NC Ni is explored in Chapter 3.

Surface Oxidation and Thermal Instability

NC materials have a larger density of grain boundaries that act as preferential nucleation sites for oxides and provide preferential diffusion paths for oxygen [59]. As a result, NC materials are expected to possess higher rates of surface oxidation. Therefore, surface oxidation during sliding wear may play a substantial role in tribological behaviour of NC metals. The role of the testing environment and surface oxidation in the

friction and wear mechanisms of electrodeposited NC Ni and NC Co is discussed in Chapters 2 and 5.

In spite of their higher oxidation rates, NC materials usually display a lower average corrosion rate, as they are less susceptible to localized intergranular corrosion and pitting, compared to their MC counterparts [59-63]. It has been suggested that [60] the large density of grain boundaries in NC materials reduces the distance between the anodic (grain boundary) and the cathodic (grain interior) sites, resulting in lower localized corrosion potentials, and hence, a more uniform corrosion and passivation of the surface.

NC materials generally possess a low thermal stability [64,65]. This property originates from the large amount of energy stored in the microstructure of these materials, which becomes a driving force for recovery and recrystallization at elevated temperatures. This restricts the tribological applications of NC materials to low-temperature environments, as well as low-to-medium sliding speed range where the surface temperature is below the temperature at which the material becomes thermally instable. The thermal stability of NC materials can be improved by annealing the material below its recrystallization temperature, solid solution strengthening, and precipitation strengthening [64,66]. Effect of thermal instability on the friction and wear behaviour of electrodeposited NC Ni is discussed in Chapter 4, where it is shown that the high-temperature wear resistance of NC Ni could be improved through dispersion strengthening mechanism, using SiC nanoparticles as reinforcements.

3. TRIBOLOGICAL PROPERTIES OF BIOLOGICAL SYSTEMS RESULTING FROM SURFACE TEXTURE

The properties mentioned in Section 2.3 have significant effects on the tribological behaviour of a smooth NC surface. In this section, the tribological properties of biological systems with much softer surfaces and the effects that various surface textures have on them are explored. These surface textures display similar effects if applied to hard NC systems, as discussed in Chapters 6 and 7.

3.1. Low-Friction Surfaces

Shark skin is a good example of biological surfaces that maintain a low friction with the surrounding environment. The surface texture of shark skin reduces the turbulence of water in the solid/fluid boundary, resulting in a reduction in the friction between the water and the shark's body. Figure 9 shows the surface texture of a shark skin [67]. The skin consists of hard, tooth-like scales with spines that point backward. The surface of these small scales is covered with microscale grooves that lie parallel to the longitudinal body axis. This special structure allows water to flow along the shark's body with minimum friction, and it reduces the adhesion of marine species to the skin [68].

Based on the structure of shark skin, industrial applications have been developed to decrease drag resistance in airplanes and boats. For example, applying a vinyl tape with tiny v-shaped grooves to the surface of airplane and boat hulls can alter the character of the air and water flow inside the boundary layer, resulting in a reduction in the friction [67].

3.2. High-Friction Surfaces

Increasing Friction by Utilizing van der Waals Forces

The gripping foot of a gecko is probably the best biological example for utilizing van der Waals forces. Capable of climbing smooth vertical surfaces, the gecko has about 5×10^5 keratinous hairs (setae) on each foot. Each seta has a length of 30-130 μm and features hundreds of pads at its end (Figure 10a) [69,70].

Autumn et al. [70] studied the adhesive force of a single gecko foot-hair, and concluded that hundreds of pads at the end of each seta interact on a molecular level with any surface. This creates a strong adhesion as a result of van der Waals forces. The gecko releases its foot by peeling off the hairs at a critical angle.

Based on the gecko's mechanism for increasing friction, Geim et al. [71] developed a microfabricated polyimide dry adhesive (Figure 10b). The surface of this material is covered by submicron, aligned posts that simulate the keratinous hairs on a gecko's foot.

Increasing Friction by Utilizing Mechanical Interlocking

Many biological systems employ mechanical interlocking mechanism to increase adhesion and friction. This mechanism is found in various types of barbs and hooks [67].

The wing-locking devices in tenebrionid beetles are good examples of surfaces that use this mechanism to increase the friction (Figure 11a) [72]. Examples of possible interlocking mechanisms used by beetles are shown in Figure 11b [72].

3.3. Surfaces with Anisotropic Frictional Properties

In the evolutionary process, some moving organisms have been optimized to minimize friction at one end of the system while maximizing it at the other end [67]. Anisotropic interlocking is an important mechanism employed by some biological systems to control frictional forces in different directions. The pad of a cricket's foot that attaches this insect to a variety of surfaces is a good example of natural surfaces that utilize the anisotropic interlocking mechanism. Scherge et al. [9] carried out a comprehensive study on the attachment pads of cricket. Figure 12a shows SEM micrographs of the surface and the cross-section of the pad [9]. The micrographs reveal that the angle between the pad surface and the direction of its hairs is less than 90º, making the friction between the pad and various surfaces anisotropic. This is better understood by considering Figure 12b, which shows the shape of the pad in static conditions, and during motion in proximal and distal directions [67]. It should be noted that the anisotropy in this system increases when normal load increases [9]. In addition, the flexibility of the pads enables them to adapt quickly to any surface profile [9]. Figure 12c shows how a combination of flexibility and orientation forms a self-mating mechanical contact that creates an anisotropic interlocking mechanism.

The nanoscale design of snake skin is another biological example that uses an anisotropic interlocking mechanism to adjust the friction in different directions [73]. In this example, ordered directional texture causes a frictional anisotropy that enhances forward motion while simultaneously serving as an effective halt to backward motion. As Figure 13 [73] shows, this frictional anisotropy in forward/backward motions is a result of the asymmetric shape of the fibre ends on snake skin. On the other hand, sharp micro-

obstacles cannot prevent forward motion because of the high flexibility of the microfibrils [73].

The fabrication of an NC Ni replica of a snake skin is described in Chapter 6. This type of structure may have potential applications in engineering systems, where a range of different COF values in various directions in needed.

3.4. Superhydrophobic Surfaces

Superhydrophobicity is critical to the survival of many insects. Some insects, like butterfly [74] and cicada [75], use superhydrophobicity to keep their wings dry and clean. Other insects, like the water strider [76], have superhydrophobic legs that enable them to support themselves on the surface of the water. The hierarchical structure of a water strider's leg, with its numerous oriented microsetae, is shown in Figure 14a. Each seta has a nanoscale grooved surface texture, as seen in Figure 14b. This multilevel surface texture allows the water strider to entrap a very high fraction of air at the leg/water interface. This interfacial air cushion prevents the legs from becoming wet, and helps the insect to overcome the gravity.

Plant leaves provide the best-known examples of water-repellent surfaces in nature. The ability to remove water from its surface cleans the leaf, and minimizes the risk of infection to the plant [68]. One of the most-studied examples of this phenomenon is the lotus leaf. Similar to a water strider's leg, the lotus leaf has a multilevel surface roughness. The surface of this leaf is composed of microscale protuberances as shown in Figure 15a. Each protuberance, in turn, is covered with a nanoscale, needle-like structure that is shown in Figure 15b. This structure entraps a high fraction of air beneath the water

droplets, creating a surface with a water contact angle greater than 150° [77]. A more detailed account of the wettability principles is presented in Chapter 7, where the fabrication of an NC Ni lotus leaf replica with a superhydrophobic surface and low COF is also described.

REFERENCES

[1]   H. Gleiter, Progr. Mater. Sci. 33 (1989) 223.

[2]   C. Suryanarayana, Int. Mater. Rev. 40 (1995) 41.

[3]   K. Lu, Mater. Sci. Eng. R16 (1996) 161.

[4]   C.C. Koch, D.G. Morris, K. Lu, A. Inoue, Mater. Res. Soc. Bull. 24 (1999) 54.

[5]   J.R. Weertman, D. Farkas, K. Hemker, H. Kung, M. Mayo, R. Mitra, H. Van Swygenhoven, Mater. Res. Soc. Bull. 24 (1999) 44.

[6]   Z.N. Farhat, Y. Ding, D.O. Northwood, A.T. Alpas., Mater. Sci. Eng. A206 (1996) 302.

[7]   H. Van Swygenhoven, J.R. Weertman, Scripta Mater. 49 (2003) 625.

[8]   Y. Wang, M. Chen, F. Zhou, E. Ma, Nature 419 (2002) 912.

[9]   M. Scherge, S.N. Gorb, Trib. Lett. 8 (2000) 1.

[10] U. Erb, A.M. El-Sherik, U.S. Patent 5,352,266 (1994).

[11] N. Wang, Z. Wang, K.T. Aust, U. Erb, Mater. Sci. Eng. A237 (1997) 150.

[12] L.L. Shaw, JOM 52 (2000) 41.

[13] R.Z. Valiev, R.R. Mulyukov, A.V. Korznikov, Mater. Sci. Eng. A168 (1993) 141.

[14] R.Z. Valiev, Mater. Sci. Eng. A234-236 (1997) 59.

[15] N.R. Tao, M.L. Sui, J. Lu, K. Lua, Nanostruct. Mater. 11 (1999) 433.

[16] Z.B. Wang, N.R. Tao, S. Li, W. Wang, G. Liu, J. Lu, K. Lu, Mater. Sci. Eng. A352 (2003) 144.

[17] K. Lu, J. Lu, Mater. Sci. Eng. A375-377 (2004) 38.

[18] T. Shinoda, M. Kawai, Surf. Coat. Tech. 169-170 (2003) 456.

[19] A.P. Zhilyaev, J. Gubicza, G. Nurislamova, A. Revesz, S. Surinach, M.D. Baro, T. Ungar, Phys. Stat. Sol. A198 (2003) 263.

[20] M. Thuvander, M. Abraham, A. Cerezo, G.D.W. Smith, Mat. Sci. Tech. 17 (2001) 961.

[21] H.Q. Li, F. Ebrahimi, Acta Mater. 51 (2003) 3905.

[22] F. Ebrahimi, G.R. Bourne, M.S. Kelly, T.E. Matthews, Nanostruct. Mater. 11 (1999) 343.

[23] A. Cziraki, I. Gerocs, E. Toth-Kadar, I. Bakonyi, Nanostruct. Mater. 6 (1995) 547.

[24] D.J. Lloyd, D. Kenny, Acta Metall. 28 (1980) 639.

[25] P. Heilmann, W.A.T. Clark, D.A. Rigney, Acta Metall. 31 (1983) 1293.

[26] G. Langford, M. Cohen, Metall. Trans. 6A (1978) 901.

[27] D.A. Hughes, N. Hansen, Acta Mater. 45 (1997) 3871.

[28] N. Hansen, in Aluminium Alloys for Packaging II, ed. J.G. Morris, Metals Society, Warrendale, PA, 1996.

[29] D.A. Hughes, N. Hansen, Acta Mater. 48 (2000) 2985.

[30] E.O. Hall, Proc. Phys. Soc. London B64 (1951) 747.

[31] N.J. Petch, J. Iron Steel Inst. 174 (1953) 25.

[32] D.M. Marsh, Proc. R. Soc. London A279 (1964) 420.

[33] C.A. Schuh, T.G. Nieh, T. Yamasaki, Scripta Mater. 46 (2002) 735.

[34] A.M. El-Sherik, U. Erb, G. Palumbo, K. Aust, Scripta Metall. Mater. 27 (1992) 1185.

[35] G.D. Hughes, S.D. Smith, C.S. Pande, H.R. Johnson, R.W. Armstrong, Scripta Metall. 20 (1986) 93.

[36] G.W. Nieman, J.R. Weertman, R.W. Siegel, Scripta Metall. 23 (1989) 2013.

[37] R. Mishra, B. Basu, R. Balasubramaniam, Mater. Sci. Eng. A373 (2004) 370.

[38] S.J. Fecht, Nanostruct. Mater. 6 (1995) 33.

[39] X. Zhang, H. Wang, C.C. Koch, Rev. Adv. Mater. Sci. 6 (2004) 53.

[40] C.Y. Barlow, P. Nielsen, N. Hansen, Acta Mater. 52 (2004) 3967.

[41] J.F. Archard, J. Appl. Phys. 24 (1953) 981.

[42] D.H. Jeong, F. Gonzalez, G. Palumbo, K.T. Aust, U. Erb, Scripta Mater. 44 (2001) 493.

[43] D.A. Rigney, L.H. Chen, M.G.S. Naylor, A.R. Rosenfield, Wear 100 (1984) 195.

[44] S.K. Ganapathi, D.A. Rigney, Scripta Metall. Mater. 24 (1990) 1675.

[45] D.O. Northwood, A.T. Alpas, Nanostruct. Mater. 10 (1998) 777.

[46] U. Andrade, M.A. Meyers, K.S. Vecchio, A.H. Chokshi, Acta Metall. Mater. 42 (1994) 3183.

[47] C.J. Youngdahl, J.R. Weertman, R.C. Hugo, H.H. Kung, Scripta Mater. 44 (2001) 1475.

[48] A.P. Malshe, W. Jiang, A.R. Dhamdhere, JOM 54 (2002) 28.

[49] J. Zhang, A.T. Alpas, Mater. Sci. Eng. A160 (1993) 25.

[50] A.T Alpas, J.D. Embury, Wear 146 (1991) 285.

[51] H. Van Swygenhoven, P.M. Derlet, Phys. Rev. B64 (2001) 1.

[52] A.G. Froseth, P.M. Derlet, H. Van Swygenhoven, Acta Mater. 52 (2004) 5863.

[53] H. Van Swygenhoven, A. Caro, D. Farkas, Mater. Sci. Eng. A309-310 (2001) 440.

[54] K.S. Kumar, S. Suresh, M.F. Chisholm, J.A. Horton, P. Wang, Acta Mater. 51 (2003) 387.

[55] K.S. Kumar, H. Van Swygenhoven, S. Suresh, Acta Mater. 51 (2003) 5743.

[56] F. Dalla Torre, H. Van Swygenhoven, M. Victoria, Acta Mater. 50 (2002) 3957.

[57] R. Schwaiger, B. Moser, M. Dao, N. Chollacoop, S. Suresh, Acta Mater. 51 (2003) 5159.

[58] F. Dalla Torre, H. Van Swygenhoven, R. Schaublin, P. Spatig, M. Victoria, Scripta Mater. 53 (2005) 23.

[59] S.H. Kim, U. Erb, K.T. Aust, F. Gonzalez, G. Palumbo, Plat. Surf. Finish. May (2004), 68.

[60] D. Cheng, V.L. Tellkamp, C.J. Lavernia, E.J. Lavernia, Ann. Biomed. Eng. 29 (2001) 803.

[61] R. Rofagha, R. Langer, A.M. El-Sherik, U. Erb, G. Palumbo, K.T. Aust, Scr. Metall. Mater. 25 (1991) 2867.

[62] R. Rofagha, U. Erb, D. Ostander, G. Palumbo, K.T. Aust, Nanostruct. Mater. 2 (1993) 1.

[63] O. Elkedim, H.S. Cao, C. Meunier, E. Gaffet, Mater. Sci. Forum 843 (1998) 269.

[64] A. Vinogradov, V. Patlan, Y. Suzuki, K. Kitagawa, V.I. Kopylov, Acta Mater. 50 (2002) 1639.

[65] T.L. Tsai, P.L. Sun, P.W. Kao, C.P. Chang, Mater. Sci. Eng. A342 (2003) 144.

[66] A. Vinogradov, S. Hashimoto, Mater. Trans. JIM 42 (2001) 74.

[67] M. Scherge and S. Gorb, Biological Micro- and Nanotribology, Springer, Berlin, 2001, 80-85.

[68] J. Genzer, A. Marmur, Mater. Res. Soc. Bull. 33 (2008) 742.

[69] A.P. Russell, J. Zool. Lond. 176 (1975) 437.

[70] K. Autumn, Y.A. Liang, S.T. Hsieh, W. Zesch, W.P. Chan, T.W. Kenny, R. Fearing, R.J. Full, Nature 405 (2000) 681.

[71] A.K. Geim, S.V. Dubonos, I.V. Grigorieva, K.S. Novoselov, A.A. Zhukov, S.Y. Shapoval, Nature Mater. 2 (2003) 461.

[72] S.N. Gorb, Int. J. Insect Morphol. Embryol. 27 (1998) 205.

[73] J. Hazel, M. Stone, M.S. Grace, V.V. Tsukruk, J. Biomech. 32 (1999) 477.

[74] J. Genzer, K. Efimenko, Biofouling 22 (2006) 339.

[75] T. Sun, L. Feng, X. Gao, L. Jiang, Acc. Chem. Res. 38 (2005) 644.

[76] X. Gao, L. Jiang, Nature 432 (2004) 36.

[77] J.P. Youngblood, N.R. Sottos, Mater. Res. Soc. Bull. 33 (2008) 732.

FIGURES

(a)

(b)

(c)
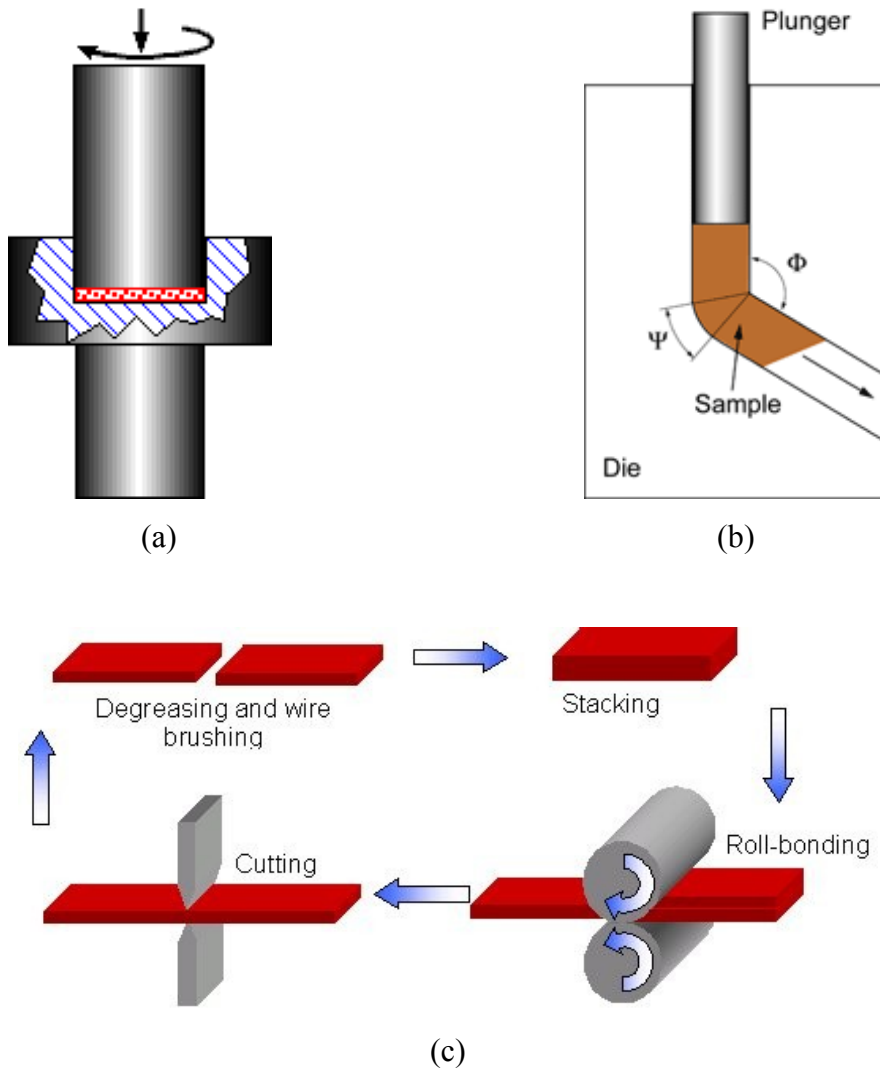
Figure 1. (a) Schematic illustration showing the principle of HPT process. (b) Schematic illustration showing the principle of ECAP process. (c) Schematic illustration showing the principle of ARB process.

(a)

(b)
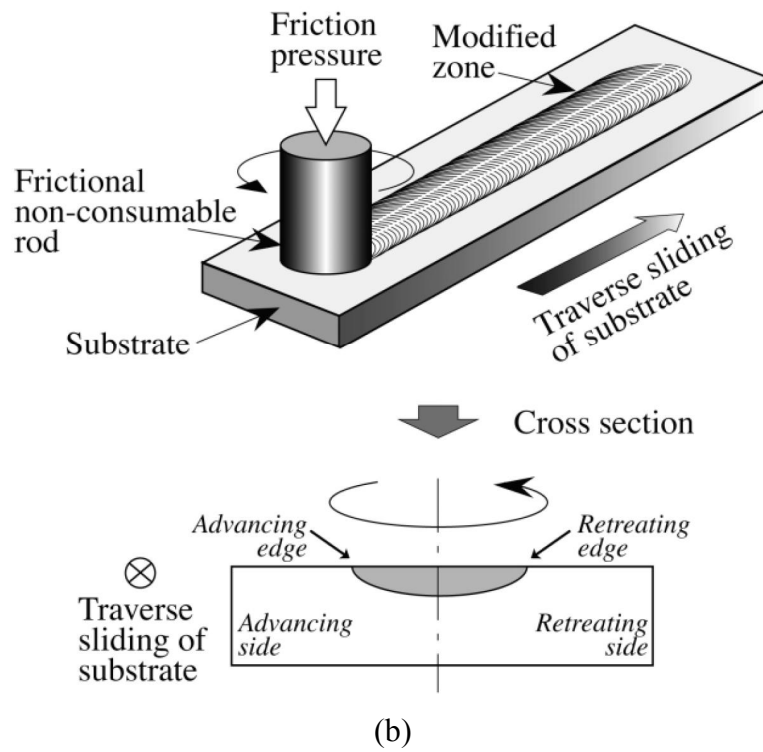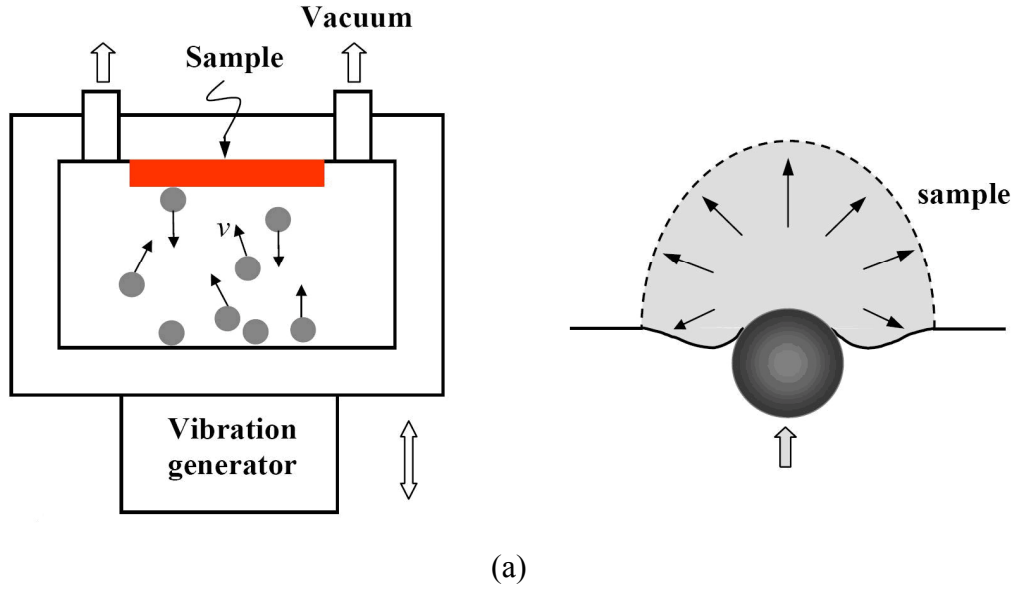
Figure 2. (a) Schematic illustration of the SMAT process set-up and the repeated multidirectional plastic deformation in the sample's surface layer [17]. (b) Schematic illustration of FTMP for surface modification [18].
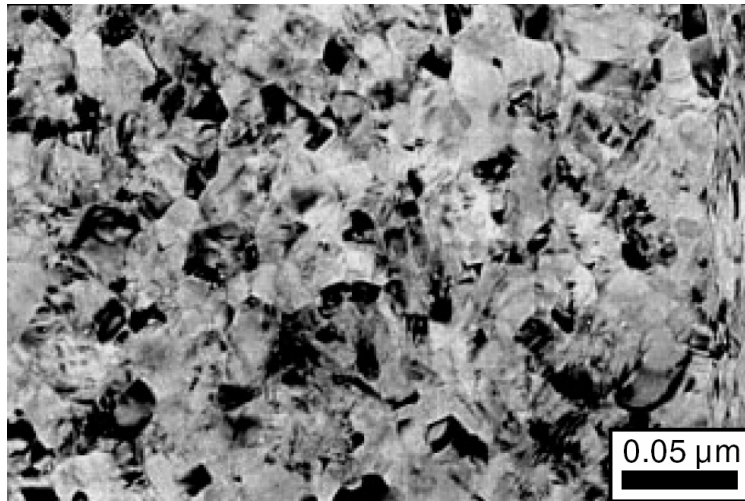
Figure 3. Microstructure of electrodeposited NC Ni sample [19].
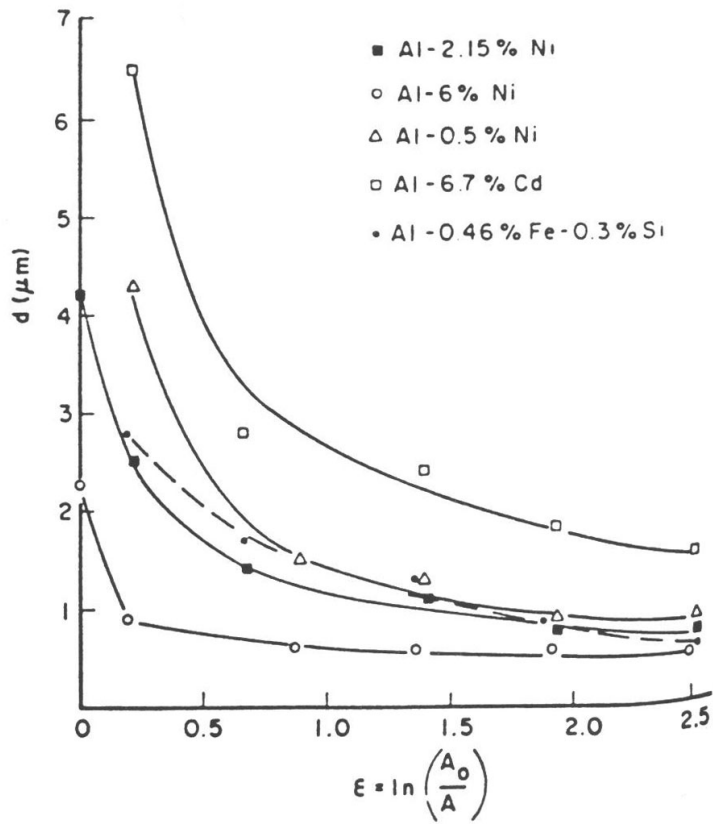
Figure 4. Variation in the subgrain diameter with strain in some Al alloys [24].
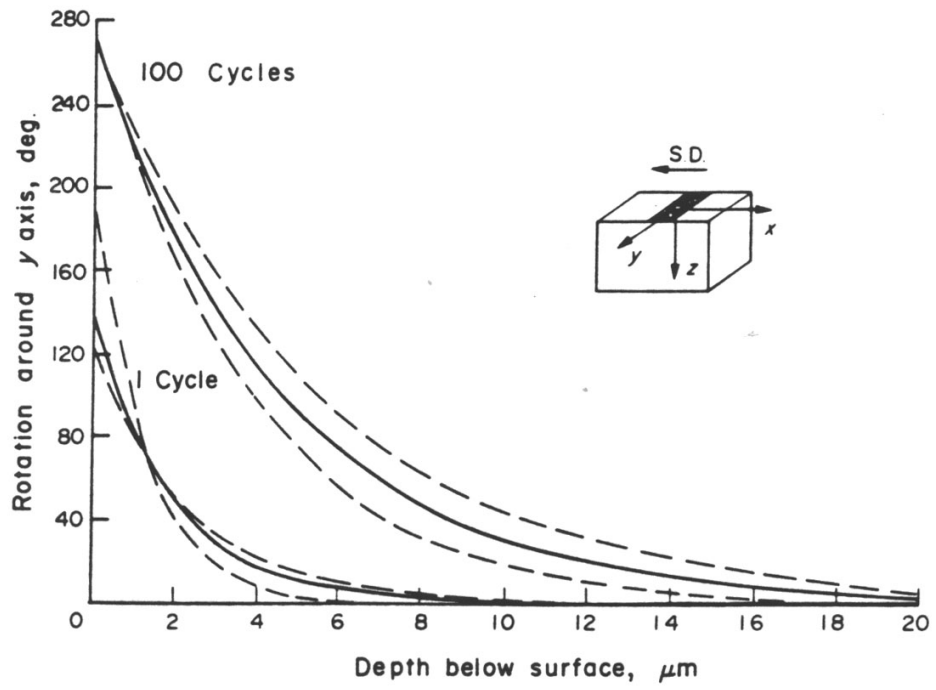
Figure 5. Rotation of cells in Cu as a function of depth bellow the wear surface after 1 cycle and 100 cycles of sliding [25].
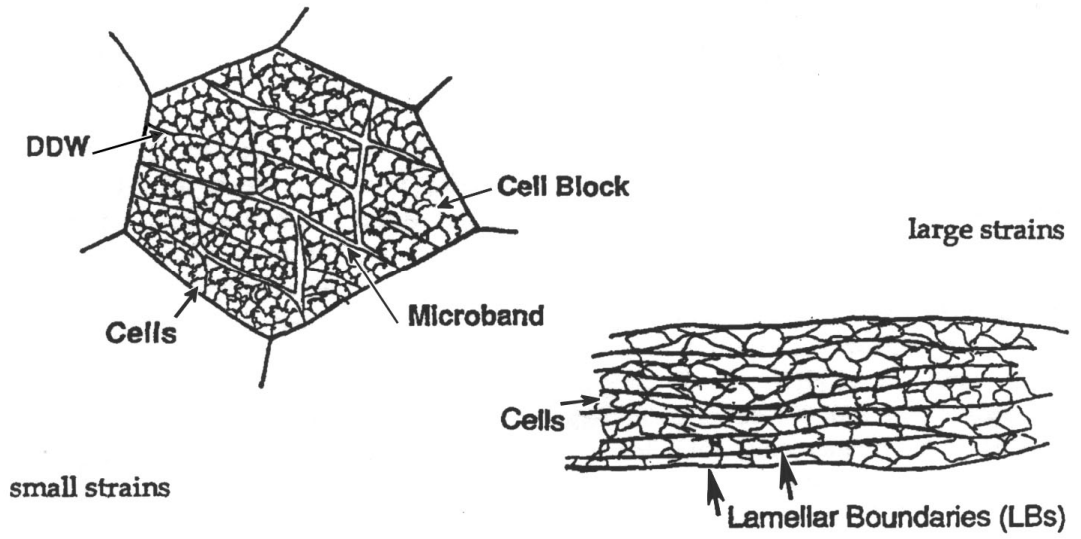
Figure 6. Schematic drawing of grain subdivision in small and large strains. DDW represents dense dislocation walls [27].
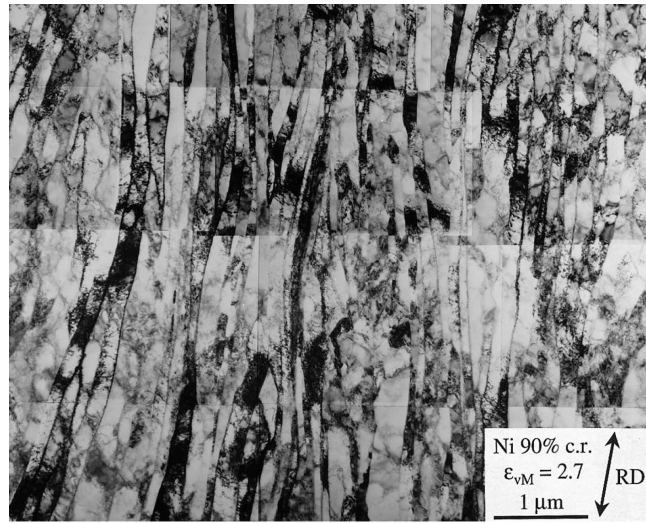
(a)
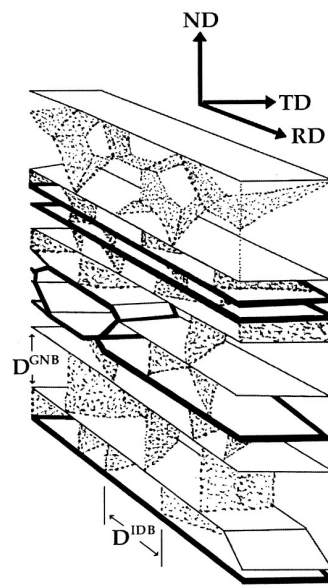
(b)

Figure 7. (a) TEM micrograph of the dislocation microstructure developed during cold rolling in pure Ni. Viewing plane is ND/RD section. The rolling direction is marked RD [29]. (b) Schematic drawing of a large strain dislocation structure showing sheets of extended LBs with IDBs bridging between them. High-angle LBs are represented by thick lines. Intercept spacings of LBs (D^{GNB}) and of cell boundaries (D^{IDB}) are shown [29].
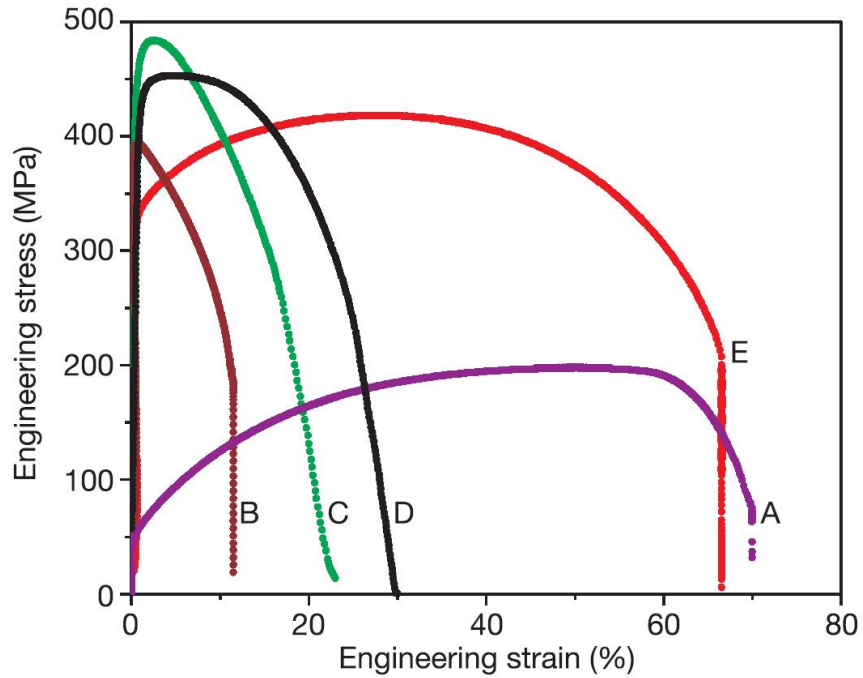
Figure 8. Stress-strain curves for pure Cu. A: annealed; B: 95% room-temperature rolled; C: 93% liquid-nitrogen-temperature rolled; D: the same as C but heat treated in 180 ℃ for 3 min; E: the same as C but heat treated in 200 ℃ for 3 min [8].
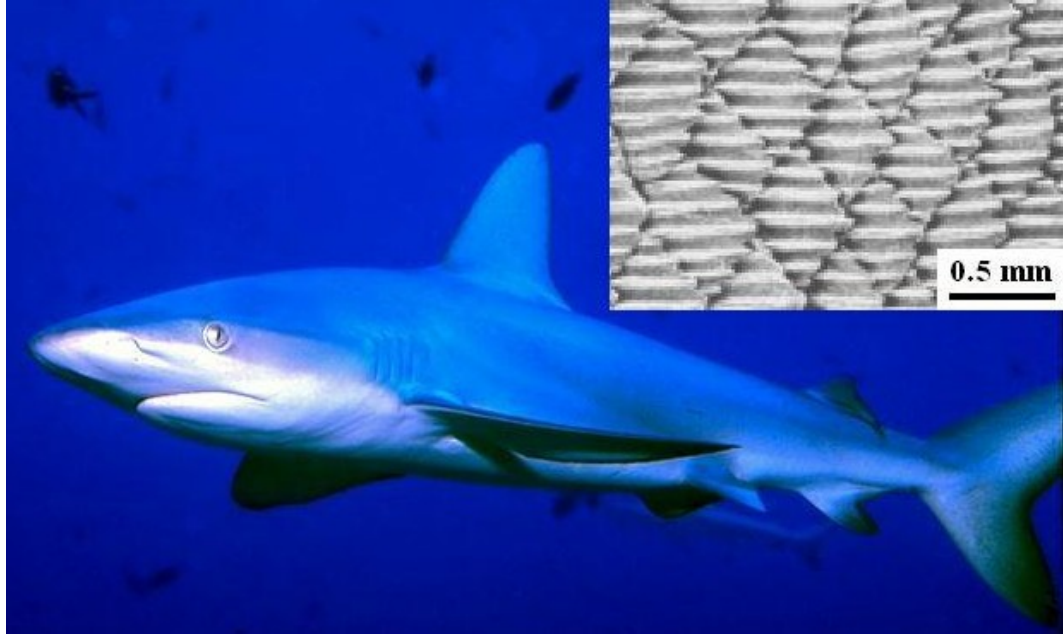
Figure 9. Grooved pattern of the shark skin surface [67].
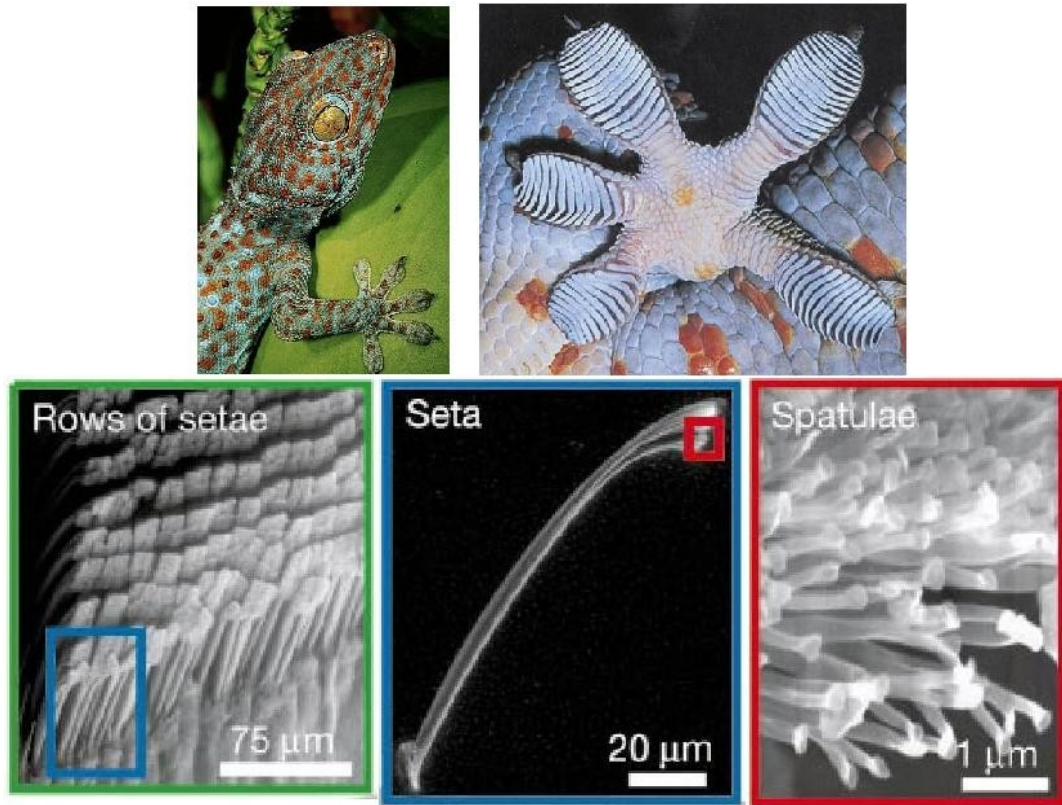
(a)
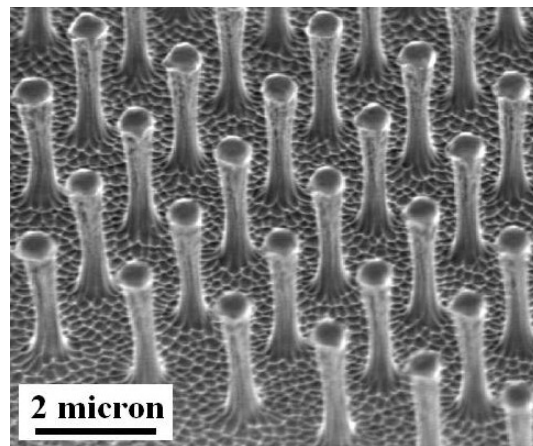
(b)

Figure 10. (a) Microstructure of the hairs in gecko's foot [70]. (b) SEM micrograph of microfabricated polyimide dry adhesive by Geim et al. [71].
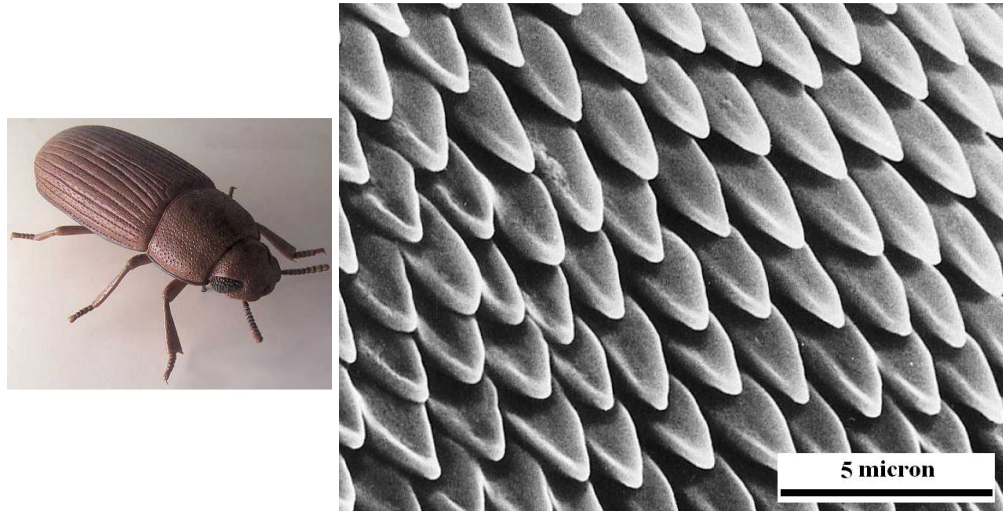
(a)
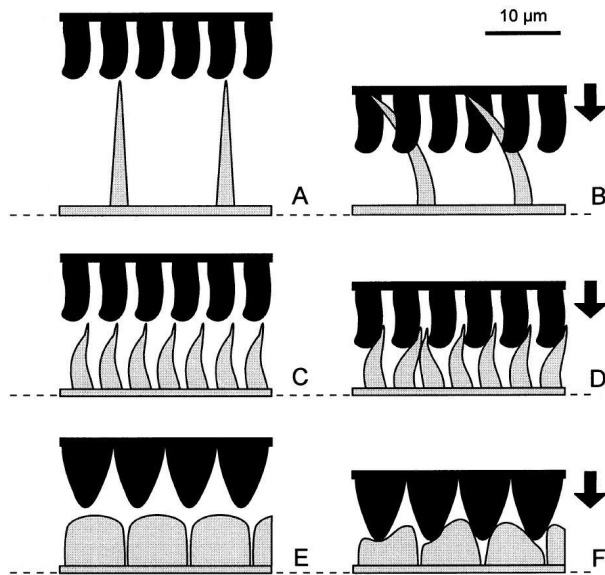
(b)

Figure 11. (a) SEM microstructure of the surfaces of the wing-locking devices in tenebrionid beetles [72]. (b) Examples of possible interlocking mechanisms between surfaces covered by microtrichia in beetles [72].
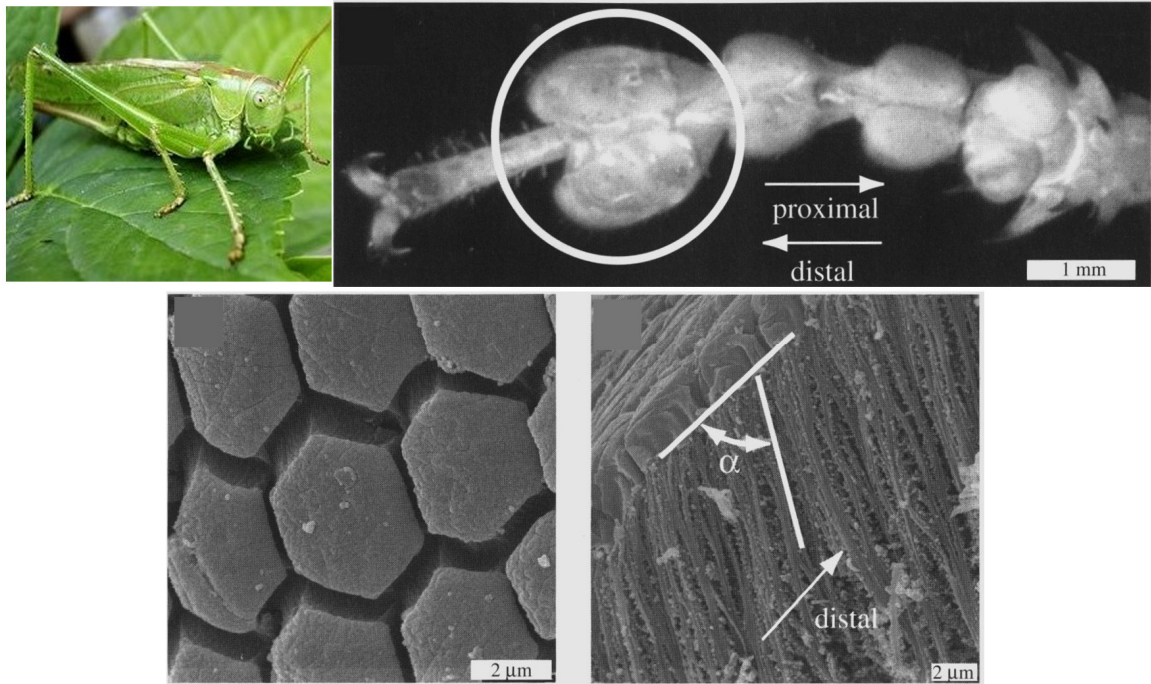
(a)
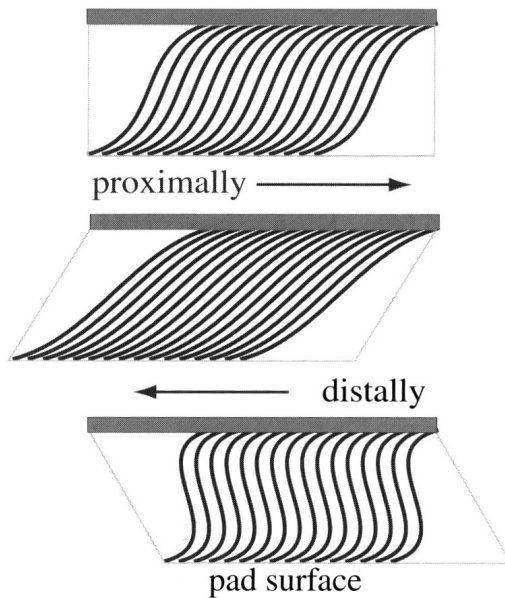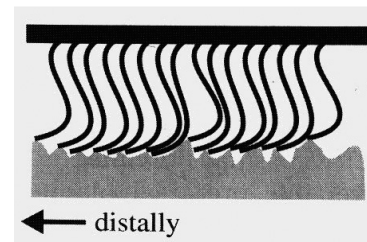
(b)   (c)

Figure 12. (a) SEM micrographs of the surface and the cross section of the pads of cricket [9]. (b) Shape of the pad in static conditions (top) and during the motion in proximal and distal directions [67]. (c) Formation of anisotropic mechanical interlocking as a result of flexibility and orientation [67].
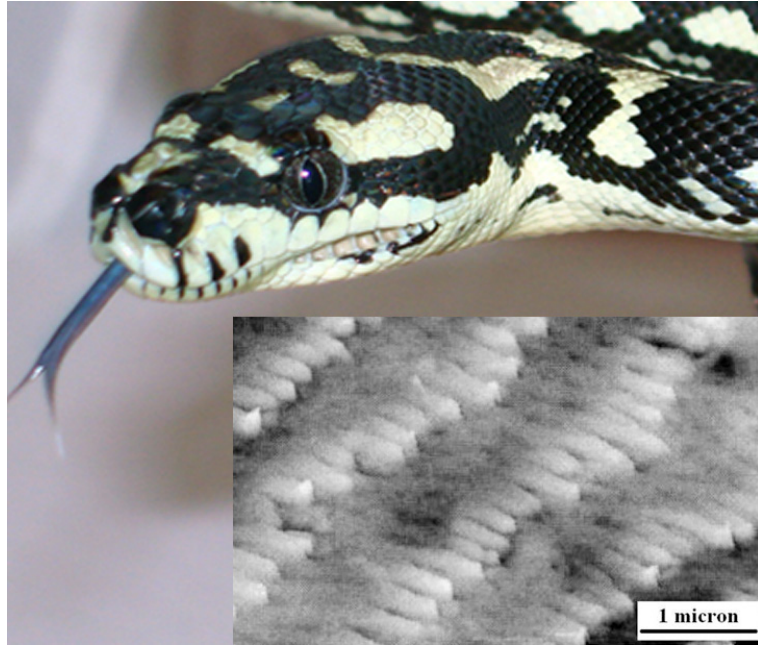
Figure 13. 3D topography of the skin of carpet python [73].

(a)
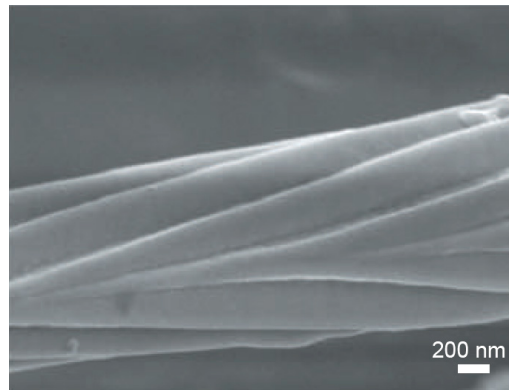
(b)

Figure 14. (a) The hierarchical structure of a water strider's leg with numerous oriented microsetae. (b) Each seta has a nanoscale grooved surface texture [76].
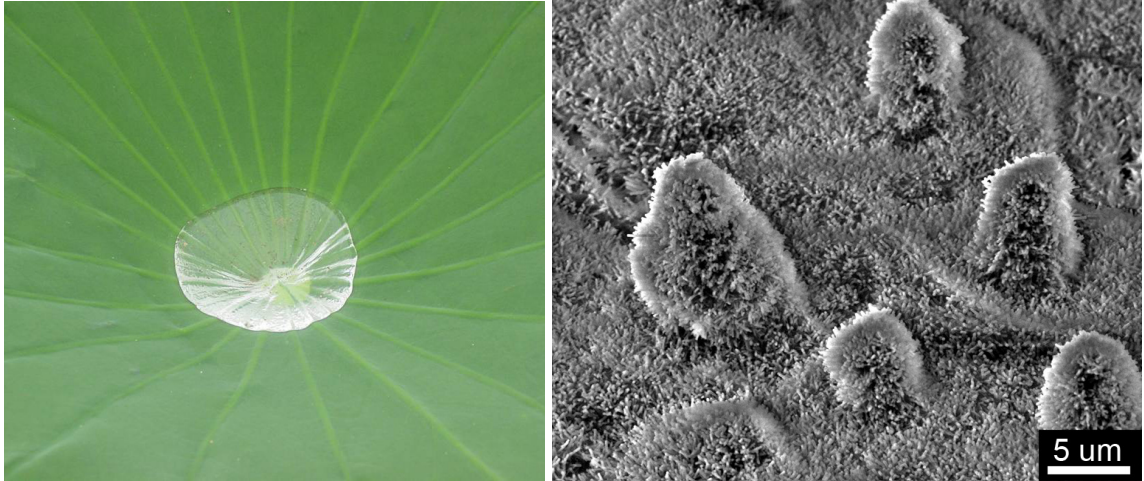
(a)
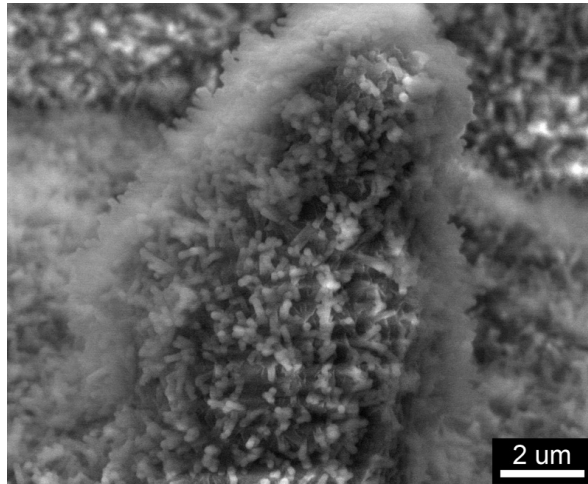
(b)

Figure 15. (a) Microscale protuberances on the surface of a lotus leaf. (b) Each protuberance is covered with a nanoscale needle-like structure.

CHAPTER 2

FRICTION AND WEAR MECHANISMS OF NANOCRYSTALLINE

NICKEL IN AMBIENT AND INERT ATMOSPHERES

1. INTRODUCTION

Nanocrystalline (NC) metallic materials are normally characterized by high strength and hardness but limited ductility [1-4]. These properties are generally attributed to the large volume fraction of grain boundaries inhibiting the mobility of dislocations [5-7]. For example, when the grain size of Ni was reduced from 15 μm to 12 nm its hardness was reported to increase from 0.9 GPa to 6.9 GPa [8, 9]. The increase in strength and hardness that accompanies grain refinement is of interest from the tribological point of view, in particular for the design of new materials and surfaces with improved wear resistance. Farhat et al. [10] tested magnetron sputtered NC Al using a pin-on-disc tribometer. In ambient air, an 80% reduction in the wear rate and a 60% reduction in the peak coefficient of friction (COF) of the 15 nm grain size Al were measured compared to an Al with a grain size of 1 mm. In the grain size (d) range of 15-100 nm where Hall-Petch type strengthening [11, 12] was observed, the wear rate (W) of the NC Al was found to be proportional to the applied load (P) consistent with the Archard's law [13], and obeyed the following equation [10]:

$$W = W_0 + K \left[\frac{P}{H_0 + kd^{-0.5}} \right] \qquad (1)$$

On the other hand, for electrodeposited NC Ni subjected to abrasion tests it was reported that the breakdown in Hall-Petch hardening at d = 12 nm was accompanied by a

change in the wear mechanism [9]. Schuh et al. [9] also compared scratch resistance of Ni samples with grain sizes of 12 nm and 15 μm. No change in the COF was observed during the nanoscratch tests performed using a Berkovich type indenter, and a COF of 0.25 was measured for both samples. Jeong et al. [14] investigated the abrasive wear resistance of electrodeposited NC Ni coatings in ambient air and found that a 44% increase in the wear resistance occurred for Ni with d = 13 nm compared to Ni with d = 90 μm. On the contrary, Mishra et al. [15] reported COF values of 0.16 and 0.29 for electrodeposited NC Ni coatings with d = 8 nm and 10 nm, respectively, and a COF of 0.62 for a microcrystalline (MC) Ni with d = 61 μm.

There is clearly a need for further experimental work to characterize micromechanisms of wear in NC metallic materials, and to rationalize microscopic processes leading to generation of wear debris or surface damage. In examining the wear behaviour of NC materials attention should be given to the role of testing atmosphere as the wear rates depend on the environmental conditions to which a material is subjected. The NC materials have a larger density of grain boundaries that act as preferential nucleation sites for oxides [16]. Grain boundaries also provide high diffusion paths for oxygen, and thus, the role of surface oxidation during sliding wear and its effects on wear damage is of interest. In this work, the role of the testing environment in the initial and steady-state wear behaviour of an NC Ni was studied by performing sliding wear tests. Tests were performed in ambient air and argon atmospheres. The wear rates and COF values measured for the NC Ni were compared with those of an MC Ni sample tested under the same environmental conditions. Metallographic and profilometric studies were

41

performed to delineate the differences between the wear mechanisms in NC and MC Ni under different testing environments.

2. EXPERIMENTAL PROCEDURES

NC Ni (99.8% purity) in the form of 0.20 mm sheets produced by electrolytic deposition were obtained from Goodfellow Cambridge Ltd. (Huntingdon, England), England. Mechanical properties of NC Ni have been well studied [4, 17, 18]. Electrolytic deposition allows production of NC Ni samples with narrowly controlled grain size distribution [19], and with low defect density compared to other NC materials production techniques [20]. For comparison, Ni foils with 99.98% purity and a thickness of 0.25 mm were obtained from the same supplier and subjected to the wear tests. The grain size of this material, referred as MC Ni, was 20±5 μm.

In order to determine their grain size, the Ni samples were examined by X-ray diffraction (XRD) using Cu K_α radiation. XRD patterns of the MC Ni and NC Ni are shown in Figures 1a-b. The MC Ni had a (200) preferential orientation, because this sample was produced by rolling and annealing. The (200) texture is more difficult to deform compared to a (111) texture, so this sample is expected to display a slightly better wear resistance compared to an MC Ni sample without a crystallographic texture.

The XRD pattern of the MC Ni exhibits narrow diffraction peaks (Figure 1a), whereas the NC Ni shows pronounced line broadening effect (Figure 1b). The grain size of the NC Ni was determined by measuring the half-peak broadening of the (111) peaks, and using [21]:

$$d = \frac{0.9\,\lambda}{\left(B_M^2 - B_S^2\right)^{0.5} \cos\theta} \tag{2}$$

where λ is the wavelength of the X-ray, θ is the peak angle, B_M is the half-peak breadth of the (111) peak for a given material, and B_S is the instrumental broadening. According to Equation 2 the grain size of the NC Ni was d = 13.6 nm. Figure 2 shows a bright field transmission electron microscopy (TEM) image of the NC Ni sample, from which the grain size was determined as 15±3 nm, in agreement with the XRD measurement.

Vickers microhardness of the MC Ni was measured as 122±5 HV and that of the NC Ni as 519±11 HV using an indentation load of 100 gf. When the microhardness measurements were done at a lower load of 10 gf, these values were lower i.e., 117±4 HV and 382±12 HV, respectively. The smaller indentation load of 10 gf was used to determine the microhardnesses of the wear tracks formed on the contact surfaces of the samples during sliding wear.

A pin-on-disc type tribometer was used for the wear tests under unlubricated sliding conditions in ambient air (with 35% relative humidity), and in a dry argon atmosphere (less than 0.2% relative humidity). For the tests in argon, the argon flow rate was about 10^{-3} m^3/s. The pin-on-disc tests were conducted under a constant normal load of 2 N and at a constant sliding speed of 0.1 m/s. An alumina, Al_2O_3, ball (H = 1,900±40 HV) of 3.18 mm diameter fixed to the end of the pin was used as the counterface. Prior to friction and wear tests, contact surfaces of the Ni samples were polished using 6, 3 and finally 1 μm diamond suspensions.

After the wear tests, the morphologies and composition of the wear tracks were investigated by an optical microscope, an optical surface profilometer and a scanning electron microscope (SEM) equipped with an energy dispersive spectroscope (EDS). The

volumetric wear losses (V) were measured according to the procedure given in ASTM standard G99 [22] using the following equation:

$$V = 2\pi R \left[r^2 \sin^{-1}\left(\frac{w}{2r}\right) - \left(\frac{w}{4}\right)\sqrt{4r^2 - w^2} \right] \tag{3}$$

where R and w are the radius and the width of the wear track, and r is the radius of the counterface ball (see Appendix A for the procedure used to measure the width of the wear track). The wear rates were computed from the slopes of volume loss vs. sliding cycle curves.

3. RESULTS AND DISCUSSION

3.1. Friction and Wear Rates under Ambient Atmospheric Conditions

Variations in the COF with the sliding cycles for the MC Ni and NC Ni tested in ambient atmosphere are shown in Figures 3a,b, respectively. The general trend of both curves was similar: COF increased rapidly at the beginning of the tests reaching a peak (COF_p), and then decreased to a lower steady-state value (COF_{ss}). The COF_p was 0.71±0.03 for the MC Ni and 0.58±0.06 for the NC Ni (18% lower than the COF_p of the MC Ni). In the MC Ni, the COF_p appeared after 20-25 cycles. In the NC Ni, however, it took 50-55 cycles to observe the peak.

During the initial contact on the surface high contact stresses are expected to occur. The Hertzian stresses for the testing geometry can be estimated using [23]:

$$\sigma_H = 0.918 \sqrt[3]{\frac{P}{D^2 C^2}} \tag{4a}$$

where P = 2 N is the applied normal load, D = 3.18 mm is the counterface ball diameter and C is the effective elastic modulus defined as:

$$C = \left(\frac{1-v_1^2}{E_1}\right) + \left(\frac{1-v_2^2}{E_2}\right) \qquad (4b)$$

Although a slight decrease in elastic modulus of Ni was reported at grain sizes smaller than 18 nm [24], the elastic moduli of MC Ni and NC Ni do not differ much [4]. Also, Poisson's ratio is insensitive to changes in microstructure [4]. The effective elastic modulus (C) is calculated using Equation 4b and using $E_1 = 200$ GPa and $v_1 = 0.31$ for both MC Ni and NC Ni, and $E_2 = 350$ GPa and $v_2 = 0.24$ for Al_2O_3. Accordingly, the initial (elastic) contact pressure was $\sigma_H = 1.56$ GPa. This is about four times higher than the yield strength of the MC Ni estimated at $\sigma_y = 0.40$ GPa from the bulk hardness (H) as $\sigma_y = H/3$ [10]. Therefore, indentation by the counterface ball is expected to cause plastic deformation during the initial contact of the counterface to the surface of the MC Ni. The indentation-induced plastic deformation is the possible cause of the occurrence of the large COF peak in the MC Ni. For the NC Ni with an estimated $\sigma_y = 1.70$ GPa, the initial contact is not likely to induce plastic deformation at the same load (2 N). As will be shown by the metallographic evidence presented in Section 3.2 ploughing and scratching of the contact surface by the counterface was responsible for the initial wear of the NC Ni. Compared to the indentation plastic deformation induced on the surface of the MC Ni the damage caused by ploughing was less extensive. As a result, COF_p was lower in the NC Ni compared to the MC Ni.

About 100 sliding cycles were needed for the samples to reach steady-state COF values. The steady-state COF values of the MC Ni and NC Ni were similar, i.e., $COF_{ss} = 0.43 \pm 0.06$ for the MC Ni, and $COF_{ss} = 0.41 \pm 0.05$ for the NC Ni.

Volumetric wear loss vs. sliding cycles curves for both samples tested under the ambient atmosphere are shown in Figure 4a. For the MC Ni, initially, the volume loss increased rapidly, but then the slope of the curve decreased and a steady-state condition was reached at longer cycles. In the NC Ni the initial high wear rate period was much less noticeable.

It is important to note the low wear rates in the NC Ni both during the initial and steady-state stages of the sliding wear. While the MC Ni initially showed characteristics of severe wear, the wear rates of the NC Ni were low during the initial and the steady-state stages of wear. A better comparison of wear rates can be made using the data shown in Figure 4b where the instantaneous wear rates of the MC Ni and NC Ni are plotted. The instantaneous wear rates (W) were defined as:

$$W = \frac{1}{2\pi R}\left(\frac{\Delta V}{\Delta N}\right) \tag{5}$$

where ΔV is volume loss within an interval of ΔN sliding cycles. The initial wear rates (at 4 sliding cycles) were W_i (MC) $= 7.88\times10^{-3}$ mm^3/m and W_i (NC) $= 0.16\times10^{-3}$ mm^3/m, and the steady-state wear rates were W_{ss} (MC) $= 0.13\times10^{-3}$ mm^3/m and W_{ss} (NC) $= 0.03\times10^{-3}$ mm^3/m. Consequently, after 4 sliding cycles, the volume loss from the NC Ni surface was as low as 2 % of that of the MC Ni. In the steady-state stage the wear rate of the NC Ni was 20% of that of the MC Ni.

3.2. Wear Tracks Developed during Initial and Steady-State Stages of Wear under Ambient Atmospheric Conditions

According to the surface profilometry image in Figure 4c, after 8 sliding cycles, a relatively wide wear track with a width of w = 106 μm was formed on the MC Ni sample

as a result of indentation plastic deformation. Some plastically deformed material within the wear track were displaced sideways and formed the pile-ups on both sides of the wear tracks as shown in Figure 4c. Optical micrograph showing the wear track during the initial wear is given in Figure 5a. After 10^3 sliding cycles, the wear track became wider (w = 160 μm), and darker in appearance due to surface oxidation (Figure 5b). The wear track also appears rougher in the steady-state condition (Figure 4d). At the edge of the wear track fragmented material pieces (microchips) were formed, creating a morphology that was different than the track edge morphology characterized by material pile-up during the initial sliding process. The change in morphology to microchip formation indicates transition to more brittle type of wear during the steady-state wear, which may be attributed to the reduction of the ductility of the material as a result of work hardening during sliding. The SEM micrograph illustrating the morphology of the microchip-type wear debris at a higher magnification is shown in Figure 5c, and the EDS spectra in Figure 5d indicates that the worn surface of the MC Ni became oxidized during steady-state wear.

Morphologies of the wear tracks formed on the NC Ni samples after testing them in air to 8 and 10^3 sliding cycles are shown in the optical surface profilometry images of Figures 4e,f. The width and depth of the wear tracks generated on the worn surfaces of the NC Ni were smaller than those of the wear tracks on the MC Ni (also see the optical micrographs in Figures 6a,b). After 8 sliding cycles, the width of the wear track, consisting of longitudinal surface scratches extending parallel to each other, was 28 μm. After 10^3 sliding cycles, the width of the wear track reached 91 μm, and its roughness was increased as well. The SEM micrograph and EDS spectra of the wear track on the

47

NC Ni after 10^3 sliding cycles (Figures 6c-e) indicate that a tribolayer containing Ni and O was formed on the worn surface of the sample. The tribolayer[*] covered the entire surface of the wear track except for a few small areas, where the tribolayer was spalled off (labelled as 2 in Figure 6c). These observations confirm that the initial plastic damage on the contact surface of the NC Ni was much smaller than that of the MC Ni consistent with lower volumetric wear and COF_p values. Also, the steady-state surface oxidation in the NC Ni was more excessive, with the oxidized tribolayers covering the contact surface almost entirely.

The microhardness of the worn surfaces of the MC Ni and NC Ni were measured using a Vickers hardness indenter at 10 gf. The results are shown in Figure 7. During the first 8 sliding cycles a 28% increase occurred in the surface hardness of the MC Ni (from 117 HV to 150 HV), while during the last 800 sliding cycles the increase in the surface hardness was only 3% (from 170 HV to 175 HV). This indicates that initial plastic deformation was accompanied by the strain hardening of the deformed layers. In the NC Ni the worn surface hardness increased from 382 HV to 387 HV during the first 8 cycles reflecting the lower capacity of the NC Ni for strain hardening. A significant increase of 29% in the surface layer hardness of the NC Ni occurred however after 10^3 sliding cycles (Figure 7). But this was due to the formation of an oxidized tribolayer on the worn surface.

---

[*] This is mainly an oxide layer rather than a mechanically mixed layer. A mechanically mixed tribolayer formed on the contact surfaces of the NC Ni reinforced with SiC microparticles as shown in Figures 7b,e in Chapter 4.

3.3. Friction and Wear Rates under an Argon Atmosphere

Both the COF values and wear rates of the MC Ni and NC Ni measured under the argon atmosphere were higher compared to those measured in air. Similar to the tests in air, during the initial stage of sliding in argon, the NC Ni showed lower COF_p^{Ar} and wear rates than the MC Ni. In the steady-state stage the wear behaviour showed a more complex trend as will be described later in this section.

The variations in the COFs of the MC Ni and NC Ni tested in argon are shown in Figures 8a,b. The peak COF values of the MC Ni and NC Ni were observed at 20 cycles; COF_p^{Ar} (MC) = 1.14 and COF_p^{Ar} (NC) = 0.77, so that the COF_p for the NC Ni was 32% lower. About 400 sliding cycles elapsed for the surfaces of the samples to reach the steady-state condition, which was 300 cycles longer compared to the ambient atmosphere. The steady-state COF of the MC Ni was COF_{ss}^{Ar} (MC) = 0.50±0.05, but a higher COF was observed in the NC Ni, i.e., COF_{ss}^{Ar} (NC) = 0.58±0.06. The higher COF values generated during the argon tests infer that the 'protective' tribolayers generated under the ambient testing conditions did not form during the tests in argon.

Figure 9a compares the variations in volume loss with sliding cycles for the MC Ni and NC Ni tested in argon. The shapes of the volume loss curves were similar to those obtained in air (Figure 4a), but the volume losses were higher in argon for both samples. The initial wear rates of the MC Ni and NC Ni under this testing environment were W_i^{Ar} (MC) = 9.97×10^{-3} mm^3/m and W_i^{Ar} (NC) = 0.22×10^{-3} mm^3/m (Figure 9b). The steady-state wear rates were W_{ss}^{Ar} (MC) = 0.18×10^{-3} mm^3/m and W_{ss}^{Ar} (NC) = 0.07×10^{-3} mm^3/m.

3.4. Wear Tracks Developed during Initial and Steady-State Stages of Wear under Argon Atmosphere

In examining the three dimensional optical surface profile of the MC Ni's wear track (Figure 9c), a peculiar feature is noted: initial contact between alumina ball and the MC Ni surface has led to the formation of a "peak-and-valley" shape deformation pattern in the argon atmosphere, suggesting a stick-and-slip type sliding behaviour. The stick-and-slip type sliding behaviour resulted in not only a large COF_p value but also the initial part of the COF curve in Figure 8a was characterized by a large number of oscillations and exhibited a serrated friction pattern. The optical micrograph of the wear track of the MC Ni tested in argon for 8 sliding cycles is shown in Figure 10a, which is characterized by contractions between bulged out sections, where the contractions correspond to the peaks in Figure 9c. After sliding to 10^3 cycles, the width of the wear track became wider and the wear track geometry became more uniform and the wear track had straight edges parallel to each other (Figure 9d). At this stage of sliding, namely during the steady-state condition, the wear track had generally a shiny metallic appearance and was characterized by long scratch marks parallel to each other extending in the sliding direction (Figure 10b). The SEM micrograph of the wear track obtained after testing to 10^3 cycles (Figure 10c) shows the longitudinal scratch marks and damage features that were consistent with the surface deformation, but no tribolayer could be observed. As the EDS spectra in Figure 10d depicted only elemental Ni, it is concluded that the oxygen content of the wear track was below the detection limit of EDS.

After 8 sliding cycles the width of the wear track on the NC Ni was 32 μm (Figures 9e and11a) and thus much smaller than that on the MC Ni. The wear track formed on the

NC Ni did not exhibit evidence for formation of a peak-and-valley morphology, i.e., no stick-and-slip type sliding occurred. After 10^3 sliding cycles, the width of the wear track was increased to 119 μm (Figures 9f and11b). A patchy tribolayer can be seen on the optical and SEM micrographs of the worn surface (Figures 11b,c). Although the tests have been maintained in argon atmosphere, the test chamber was not completely oxygen free. The tribolayer contained a small amount of oxygen (Figure 11d) but the oxygen peak is much smaller than that found in tribolayers formed in the ambient atmosphere (Figure 6d). The tribolayer was not continuous and exposed sections of the NC Ni can be seen in Figure 11c, whose elemental composition are given in Figure 11e.

After the first 8 sliding cycles in argon, a 21% increase in the surface hardness of the MC Ni was measured (Figure 7). On the contrary, no noticeable increase occurred in the surface hardness of the NC Ni in the argon atmosphere even after 10^3 sliding cycles: the hardness of the tribolayer formed on the contact surfaces of the NC Ni was significantly lower than the hardness of the oxide-rich tribolayer generated in air.

Surface oxidation has a pronounced effect in controlling the steady-state wear rates and COFs. The higher tendency of the NC Ni for oxidation during sliding wear [16] along with the continuous coverage of the wear tracks by oxide-rich tribolayers in air helped to maintain lower wear rates and COFs during ambient air wear tests. In the ambient atmosphere, oxidized debris particles became agglomerated and compacted on the top of the wear track, forming a wear protective tribolayer attached to the contact surfaces of the NC Ni. It has been proposed that a decrease in partial pressure of oxygen in the test environment may lead to an increase in the size of the wear debris particles but a decrease in their generation rate [25]. Consequently, under the low oxygen partial

pressure condition during the argon tests a discontinuous but thicker tribolayer can be expected to form compared to that formed in air. This is consistent with the rougher wear tracks generated on the worn surfaces of the NC Ni in argon (R_a = 105 nm) compared to those formed in air (R_a = 48 nm).

4. SUMMARY AND CONCLUSIONS

Friction and wear behaviour of an electrodeposited nanocrystalline (NC) Ni with a grain size of 15±3 nm and a hardness of 519±11 HV was studied by paying particular attention to role of the testing environment. An MC Ni with a grain size of 20±5 μm and a hardness of 122±5 HV was also subjected to the same sliding wear tests. It is instructive to summarize the COF values and the wear rates of the MC Ni and NC Ni tested in air and in argon in the form of a table for comparison (Table 1), and relate them to the surface profiles obtained during initial and steady-state stages of sliding wear. Accordingly, the main conclusions of this work are as follows:

1. In an ambient atmosphere, during the initial stage of wear, the COF of both MC Ni and NC Ni reached a peak value (COF_p) and then gradually decreased to a constant steady-state value (COF_{ss}). For the NC Ni COF_p (0.58) was 18% lower than that of the MC Ni (0.71). The COF_{ss} values were comparable to each other, i.e., COF_{ss} (MC) = 0.43 and COF_{ss} (NC) = 0.41. The initial wear rate of the NC Ni (W_i (NC) = 0.16×10^{-3} mm^3/m) was almost two orders of magnitude smaller than that of the MC Ni (W_i (MC) = 7.88 ×10^{-3} mm^3/m). The steady-state wear rate of the NC Ni (W_{ss} (NC) = 0.03×10^{-3} mm^3/m) was 77% lower than that of the MC Ni (W_{ss} (MC) = 0.13×10^{-3} mm^3/m).

2. In an argon atmosphere, the peak COF of the NC Ni was 32% lower than that of the MC Ni, i.e., COF_p^{Ar} (MC) = 1.14 and COF_p^{Ar} (NC) = 0.77. The steady-state COF values for the MC Ni and NC Ni samples were comparable, i.e., COF_{ss}^{Ar} (MC) = 0.50 and COF_{ss}^{Ar} (NC) = 0.58. Both MC Ni and NC Ni showed higher wear rates in argon than in air, but again the initial wear rate of the NC Ni was much lower than that of the MC Ni, i.e., W_i^{Ar} (MC) = 9.97×10^{-3} mm^3/m and W_i^{Ar} (NC) = 0.22×10^{-3} mm^3/m. Also, the steady-state wear rate of the NC Ni was 61% lower than that of the MC Ni.

3. High initial contact stresses caused plastic deformation of softer surfaces of the MC Ni as a result of the penetration of the spherical alumina counterface. This was not the case for the NC Ni, for which ploughing of the surface by the counterface was responsible for the initial damage. Consequently, the wear tracks of the NC Ni consisted of only a small number of shallow surface scratches. The ploughing appeared to have occurred as a result of plastic deformation but compared to the plastic deformation induced on the surface of the MC Ni, the damage was much less extensive.

4. The initial mechanical damage mechanisms were the same for both testing environments, but testing in an argon atmosphere caused more extensive damage on both materials. A stick-and-slip type damage to the MC Ni surface tested in argon was the most significant damage observed.

5. The strain hardening of the MC Ni surfaces and surface oxidation (in ambient atmosphere) were among the factors that led to lower steady-state wear rates and COFs compared to the initial wear rates and COFs. Oxidation was more prominent in the NC Ni. This material did not show noticeable strain hardening during sliding wear. During

the steady-state wear in air oxide-rich tribolayers (different morphologies) formed on both MC Ni and NC Ni surfaces.

6. No tribolayer was observed on the contact surfaces of the MC Ni in argon resulting in higher steady-state wear rates for the MC Ni. In argon atmosphere, a tribolayer was formed on the contact surfaces of the NC Ni, but it was patchy and softer, and had lesser oxide content compared to the tribolayer formed in air. The steady-state wear rate of the NC Ni in the argon atmosphere was consequently lower than that of the MC Ni tested under the same conditions but higher than that of the NC Ni tested in air.
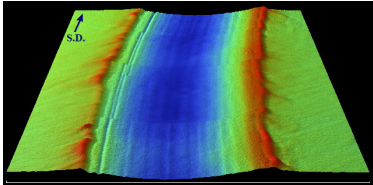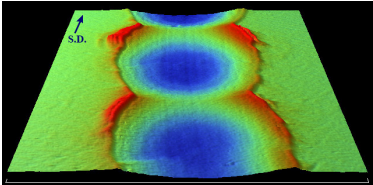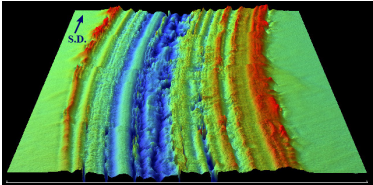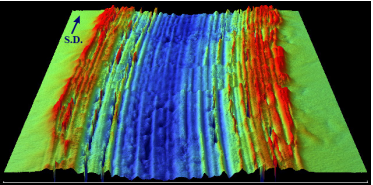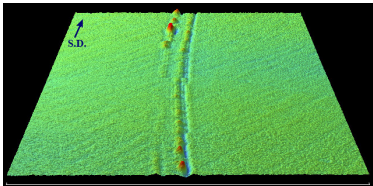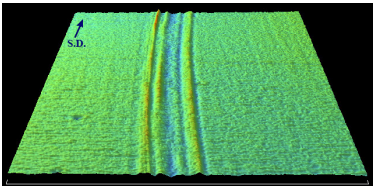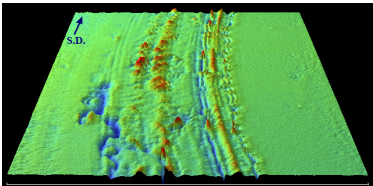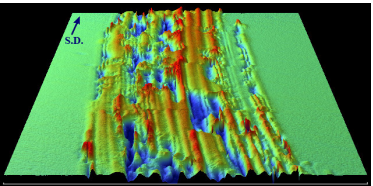
REFERENCES

[1] C.C. Koch, D.G. Morris, K. Lu, A. Inoue, Mater. Res. Soc. Bull. 24 (1999) 54.

[2] J.R. Weertman, D. Farkas, K. Hemker, H. Kung, M. Mayo, R. Mitra, H. Van Swygenhoven, Mater. Res. Soc. Bull. 24 (1999) 44.

[3] H. Van Swygenhoven, J.R. Weertman, Scripta Mater. 49 (2003) 625.

[4] K.S. Siow, A.A.O. Tay, P. Oruganti, Mater. Sci. Tech. 20 (2004) 285.

[5] H. Gleiter, Progr. Mater. Sci. 33 (1989) 223.

[6] C. Suryanarayana, Int. Mater. Rev. 40 (1995) 41.

[7] K. Lu, Mater. Sci. Eng. R16 (1996) 161.

[8] G.D. Hughes, S.D. Smith, C.S. Pande, H.R. Johnson, R.W. Armstrong, Scripta Metall. 20 (1986) 93.

[9] C.A. Schuh, T.G. Nieh, T. Yamasaki, Scripta Mater. 46 (2002) 735.

[10] Z.N. Farhat, Y. Ding, D.O. Northwood, A.T. Alpas, Mater. Sci. Eng. A206 (1996) 302.

[11] E.O. Hall, Proc. Phys. Soc. 64 (1951) 747.

[12] N.J. Petch, J. Iron Steel Inst. 174 (1953) 25.

[13] J.F. Archard, J. Appl. Phys. 24 (1953) 981.

[14] D.H. Jeong, F. Gonzalez, G. Palumbo, K.T. Aust, U. Erb, Scripta Mater. 44 (2001) 493.

[15] R. Mishra, B. Basu, R. Balasubramaniam, Mater. Sci. Eng. A373 (2004) 370.

[16] S.H. Kim, U. Erb, K.T. Aust, F. Gonzalez, G. Palumbo, Plat. Surf. Finish. May (2004), 68.

[17] F. Ebrahimi, G.R. Bourne, M.S. Kelly, T.E. Matthews, Nanostruct. Mater. 11 (1999) 343.

[18] K.S. Kumar, S. Suresh, M.F. Chisholm, J.A. Horton, P. Wang, Acta Mater. 51 (2003) 387.

[19] A.P. Zhilyaev, J. Gubicza, G. Nurislamova, A. Revesz, S. Surinach, M.D. Baro, T. Ungar, Phys. Stat. Sol. A198 (2003) 263.

[20] L.L. Shaw, JOM 52 (2000) 41.

[21] B.E. Warren, J. Biscoe, J. Amer. Ceram. Soc. 21 (1938) 49.

[22] Friction and Wear Testing, ASM, Materials Park, OH, 1997, pp. 124-128.

[23] Metals Handbook, 1st ed., ASM, Materials Park, OH, 1992, vol. 18, pp. 480-488.

[24] Y. Zhou, U. Erb, K.T. Aust, G. Palumbo, Z. Metallkd. 94 (2003) 1157.

[25] J. Jiang, F.H. Stott, M.M. Stack, Wear 203-204 (1997) 615.

TABLE

Table 1. Wear mechanisms of the MC Ni and NC Ni in the ambient and inert atmospheres.

Sample	Initial Wear		Steady-State Wear	
	Air	Argon	Air	Argon
MC Ni 122 HV				
	COF= 0.71 W= 7.88×10^{-3} mm^3/m	COF= 1.14 W= 9.97×10^{-3} mm^3/m	COF= 0.43 W= 0.13×10^{-3} mm^3/m	COF= 0.50 W= 0.18×10^{-3} mm^3/m
	Large plastic deformation by indentation of counterface.		Formation of oxidized surfaces. Ploughing of previously deformed wear track.	No tribolayer formation. Ploughing of previously deformed wear track.
NC Ni 519 HV				
	COF= 0.58 W= 0.16×10^{-3} mm^3/m	COF= 0.77 W= 0.22×10^{-3} mm^3/m	COF= 0.41 W= 0.03×10^{-3} mm^3/m	COF= 0.58 W= 0.07×10^{-3} mm^3/m
	Small plastic deformation by ploughing. Formation of continuous surface scratches.		Formation of oxidized tribolayers on most of the wear track prevents ploughing of the surface.	Formation of discontinuous tribolayers with less oxygen reduces ploughing of the surface.

FIGURES
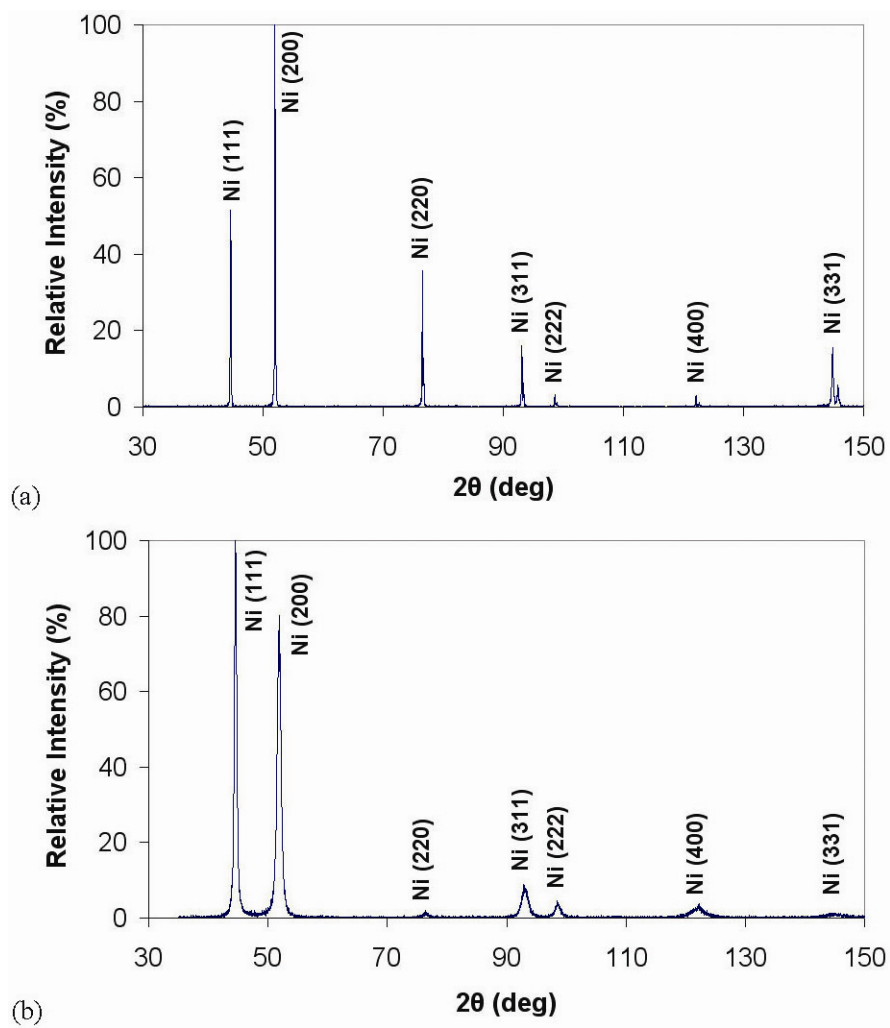
Figure 1. The XRD patterns of: (a) the MC Ni, and (b) the NC Ni.

Figure 2. A bright field TEM image of the NC Ni.

(a)

(b)
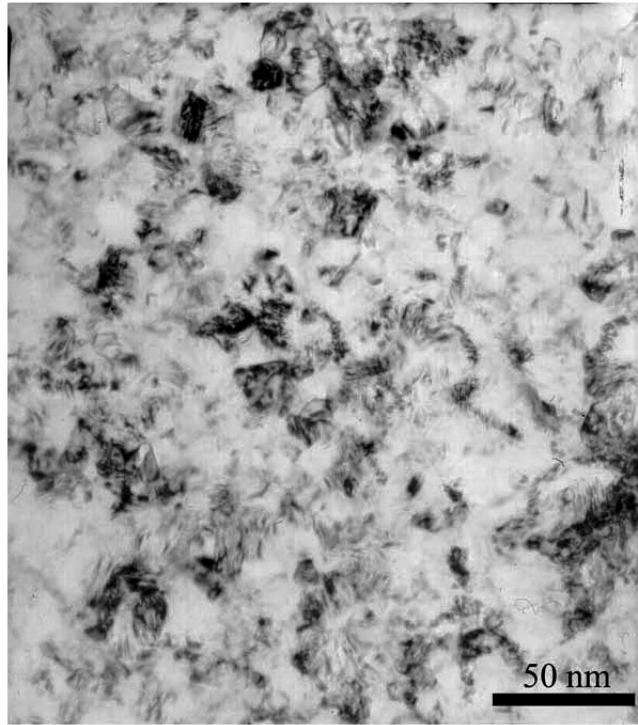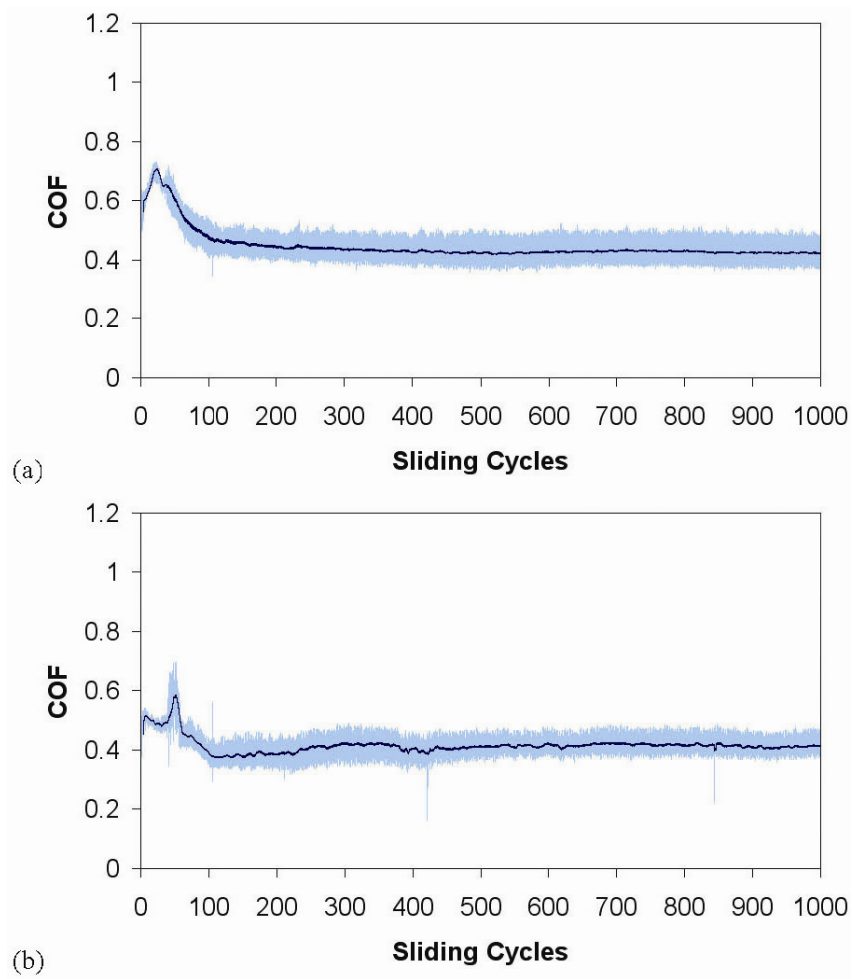
Figure 3. Variations in the COFs of: (a) the MC Ni, and (b) the NC Ni, in air (35% RH).
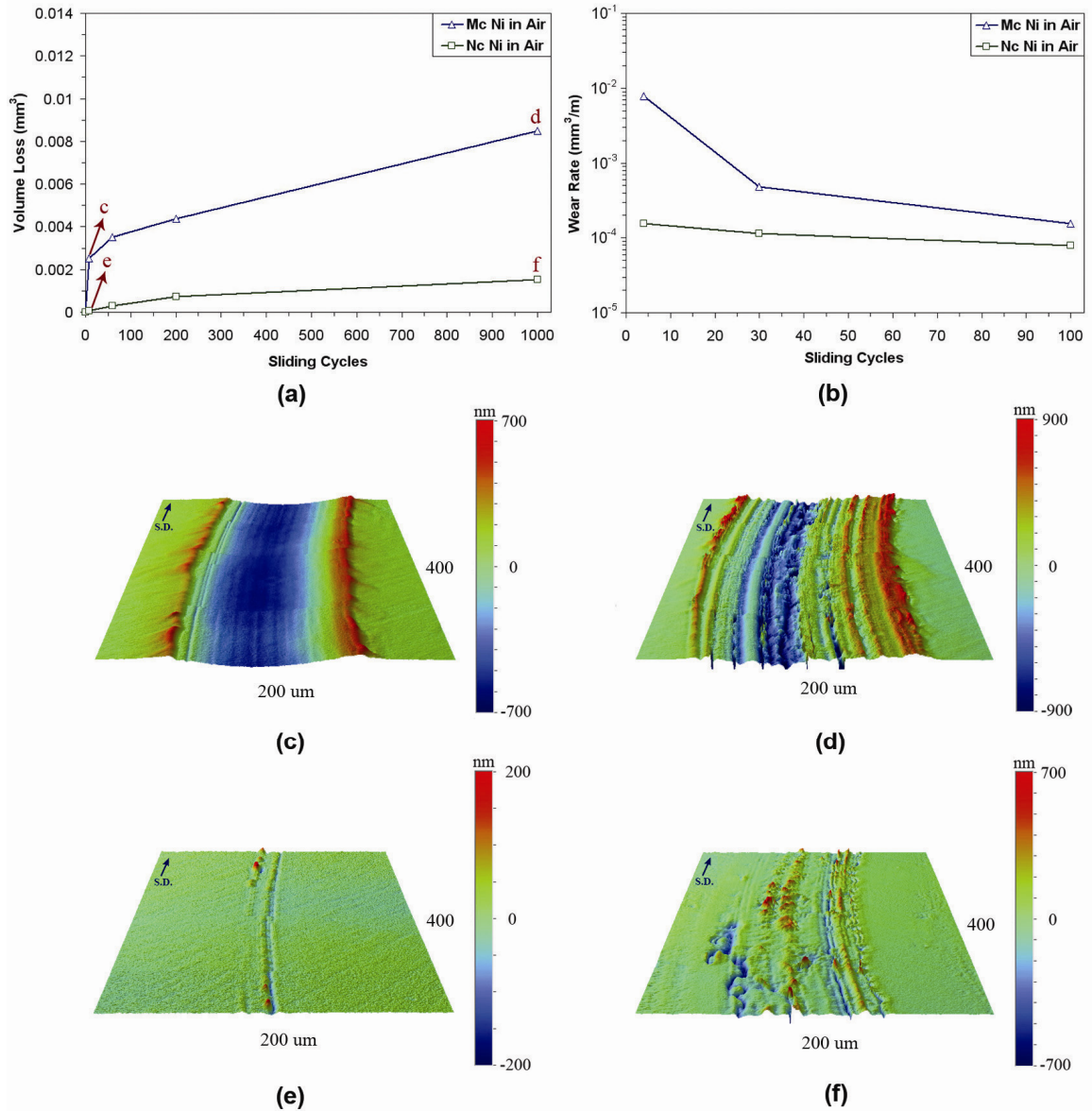
Figure 4. (a) Variations in volume loss with sliding cycles for the MC Ni and the NC Ni in air (35% RH). (b) Variations in initial wear rate with sliding cycles under the same conditions. (c-f) Corresponding initial and steady-state surface damage profiles as marked in (a).
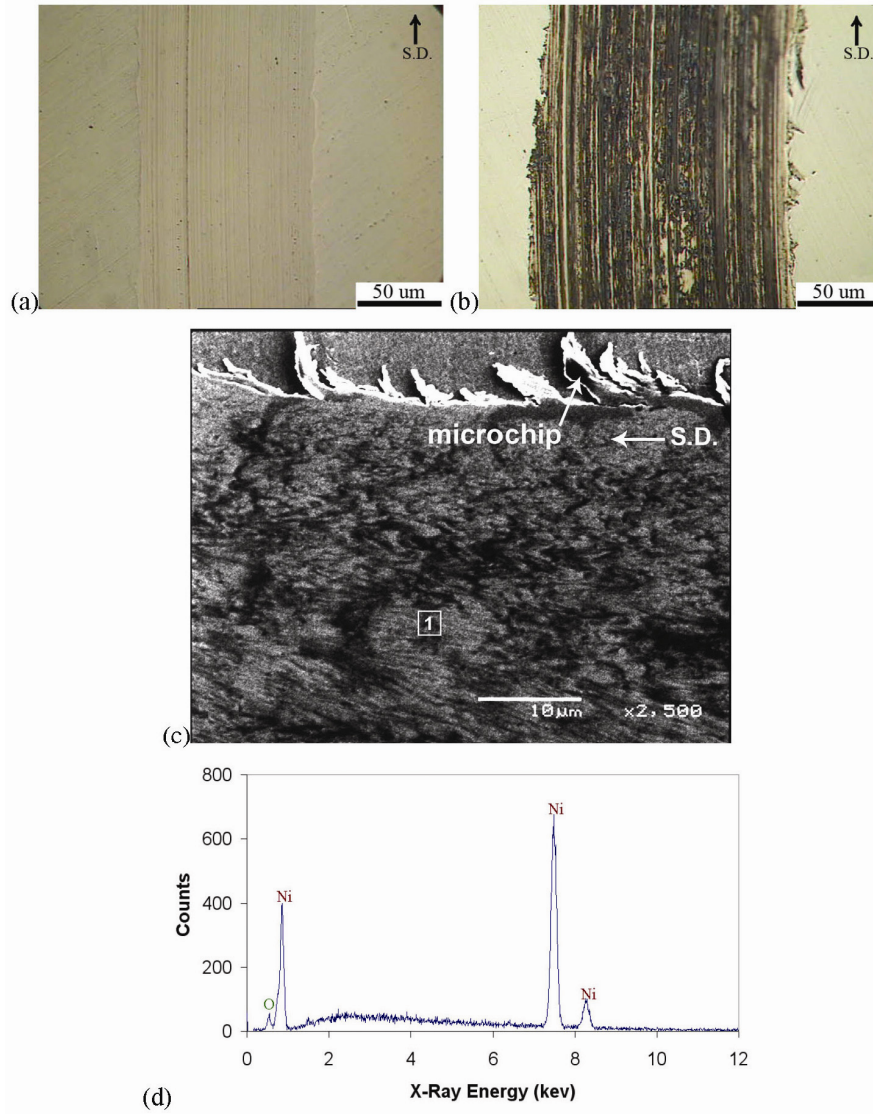
Figure 5. (a,b) Optical micrographs of the MC Ni wear tracks formed after 8 and 10^3 sliding cycles in air (35% RH). (c) SEM micrograph of the track shown in (b). (d) EDS spectra of the area labelled 1 in (c).
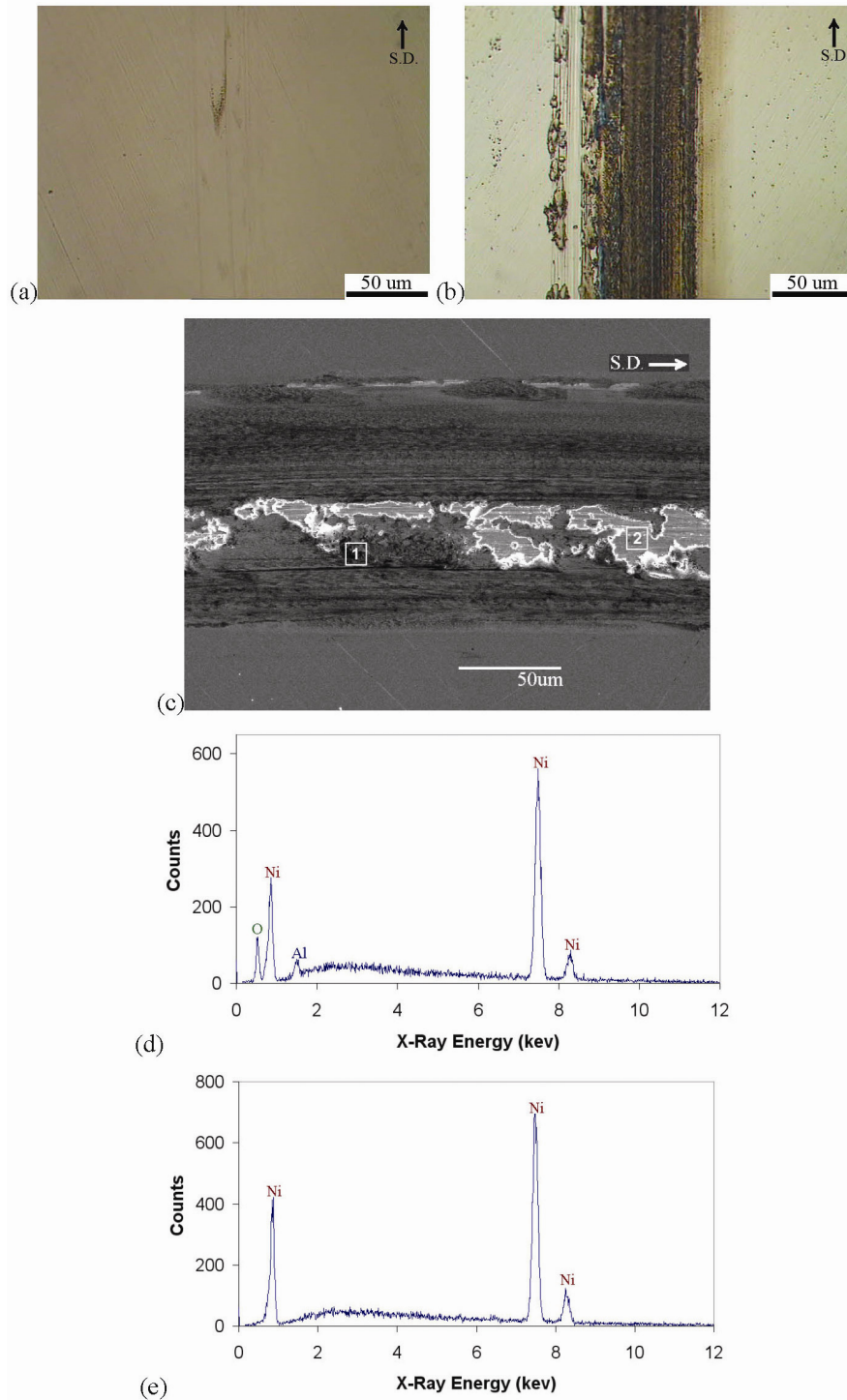
Figure 6. (a,b) Optical micrographs of the NC Ni wear tracks formed after 8 and 10^3 sliding cycles in air (35% RH). (c) SEM micrograph of the track shown in (b). (d) EDS spectra of the area labelled $\underline{1}$ in (c). (e) EDS spectra of the area labelled $\underline{2}$ in (c).
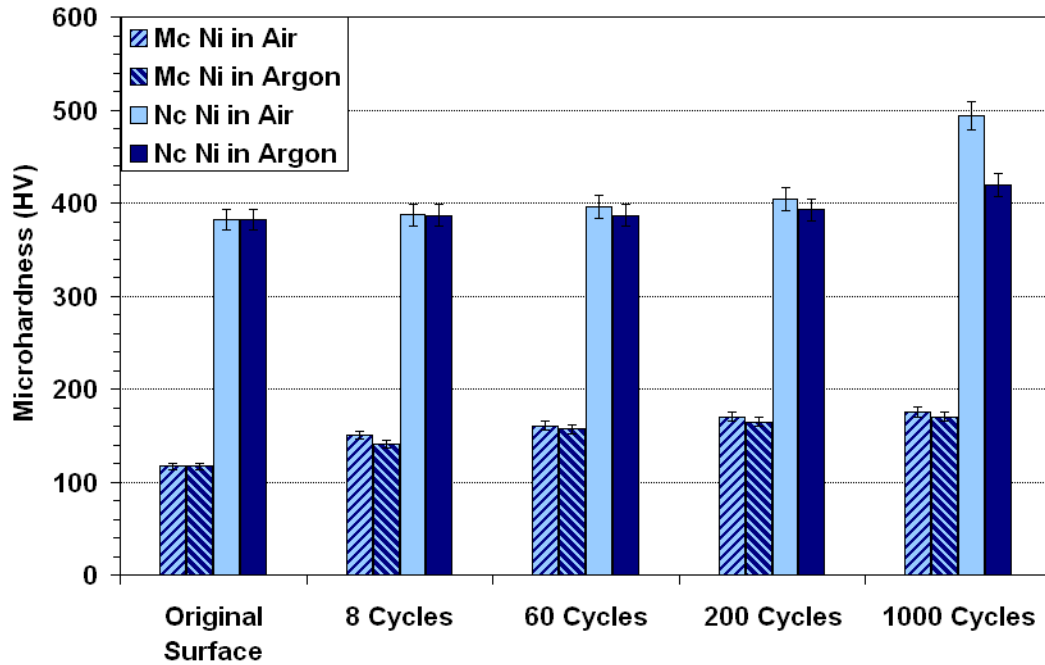
Figure 7. Microhardness values of the original and worn surfaces of the MC Ni and NC Ni after 8, 60, 200, and 10^3 sliding cycles in the air and argon atmospheres. All measurements were made under 10 gf normal load. In the case of the worn surfaces with discontinuous tribolayers, the indentation tests were performed on the tribolayers.

(a)

(b)
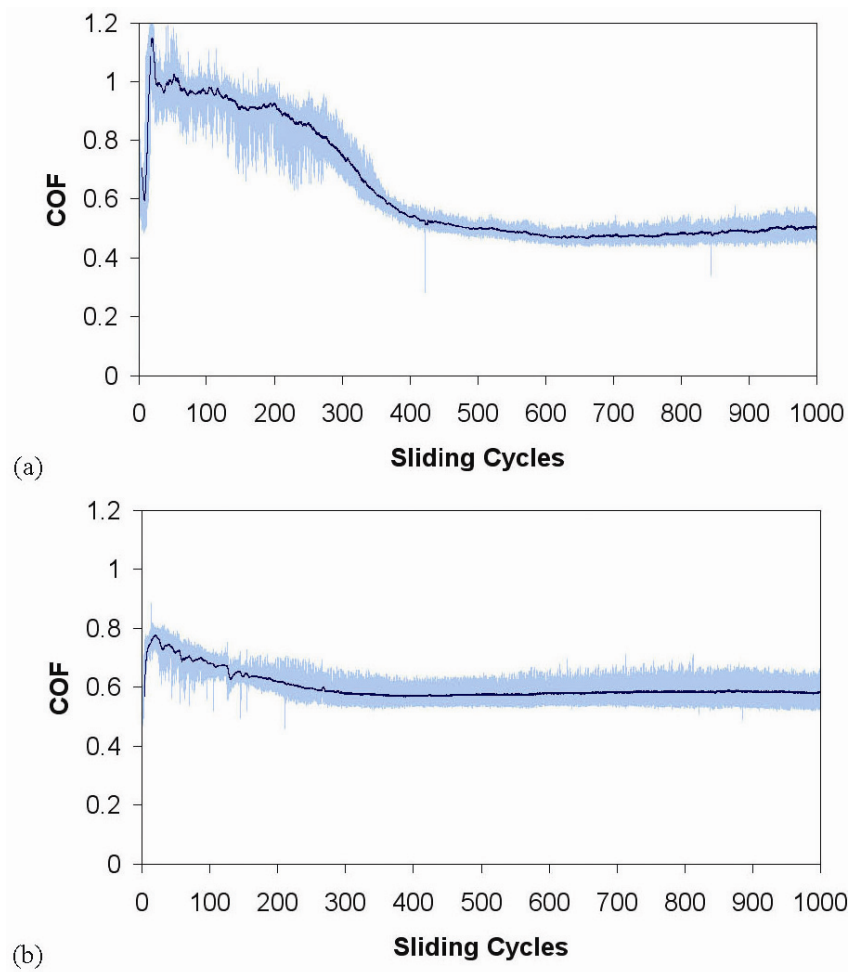
Figure 8. Variations in the COFs of: (a) the MC Ni, and (b) the NC Ni, in dry argon.
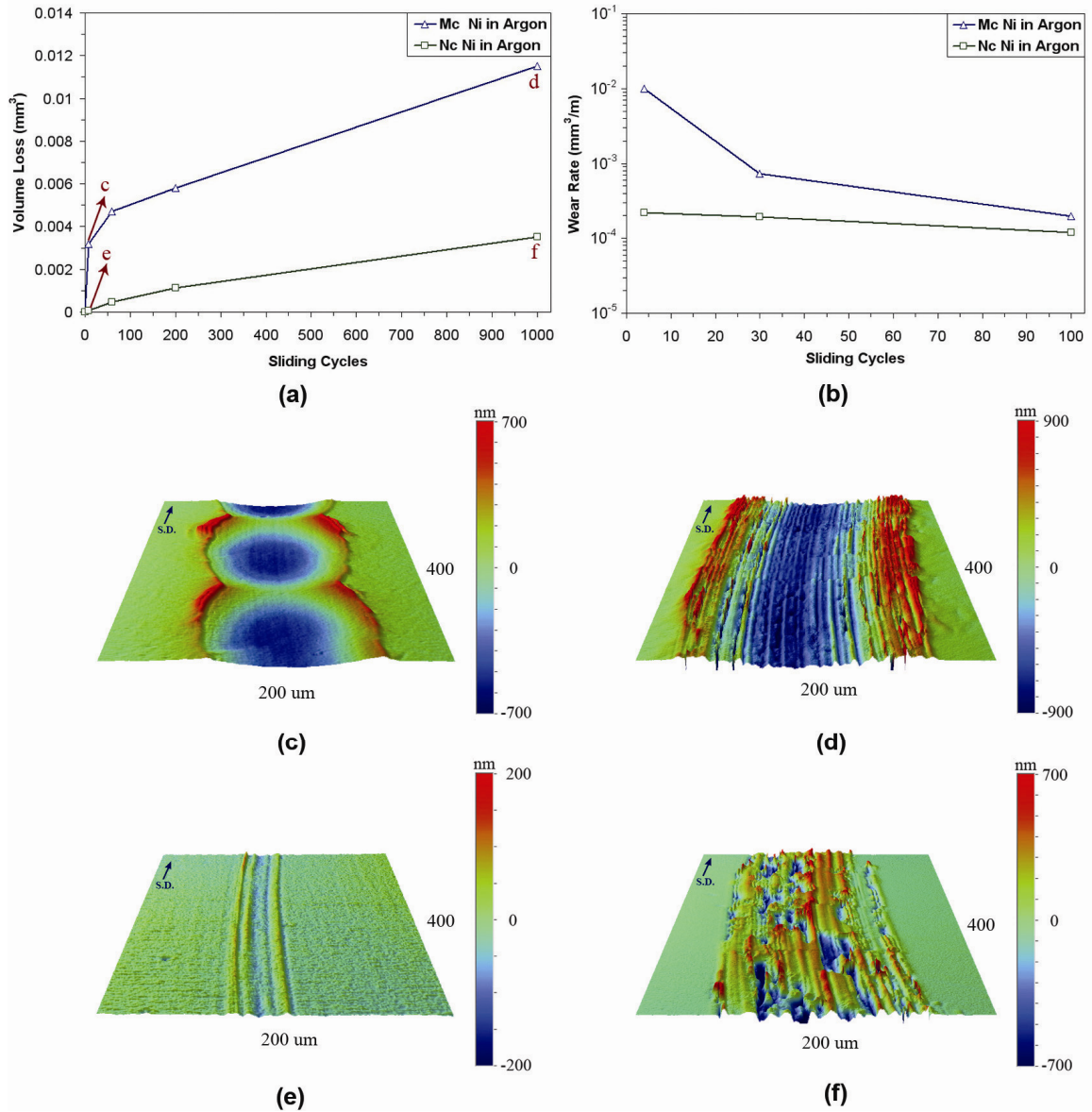
Figure 9. (a) Variations in volume loss with sliding cycles for the MC Ni and NC Ni in dry argon. (b) Variations in initial wear rate with sliding cycles under the same conditions. (c-f) Corresponding initial and steady-state surface damage profiles as marked in (a).
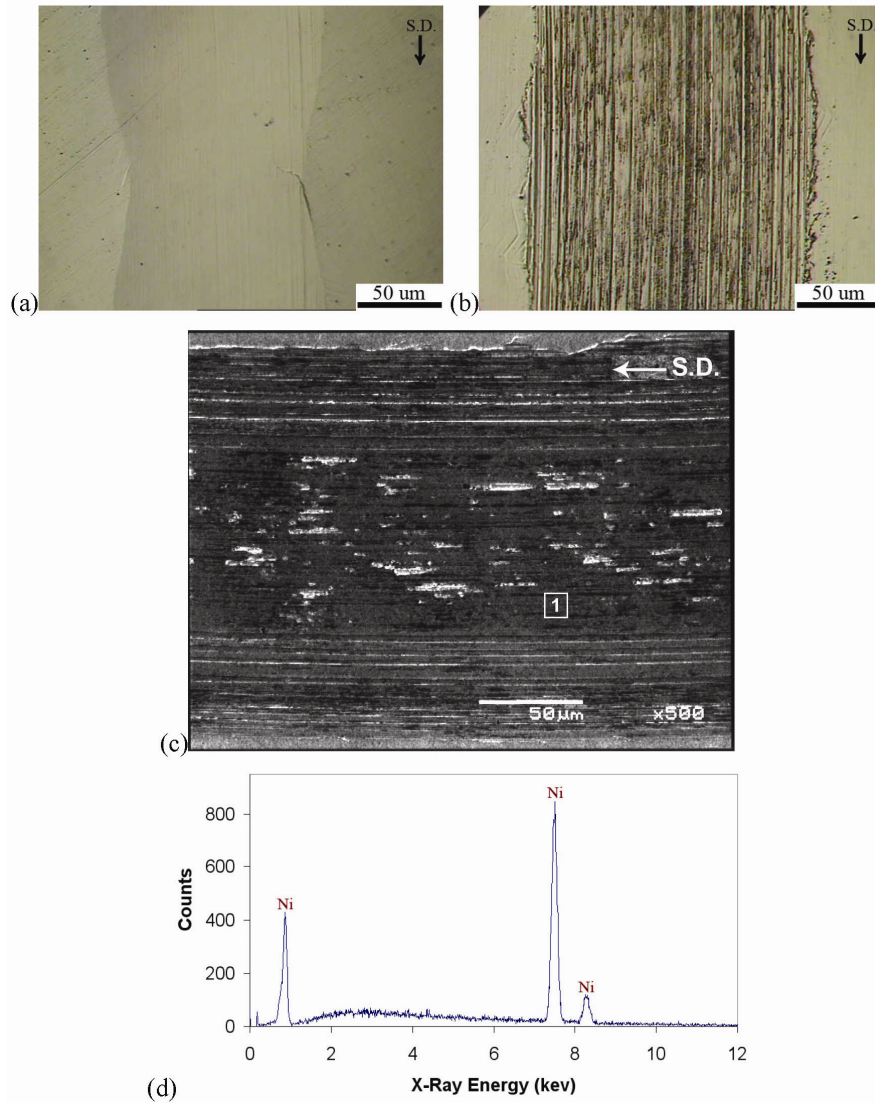
Figure 10. (a,b) Optical micrographs of the MC Ni wear tracks formed after 8 and 10^3 sliding cycles in dry argon. (c) SEM micrograph of the track shown in (b). (d) EDS spectra of the area labelled 1 in (c).
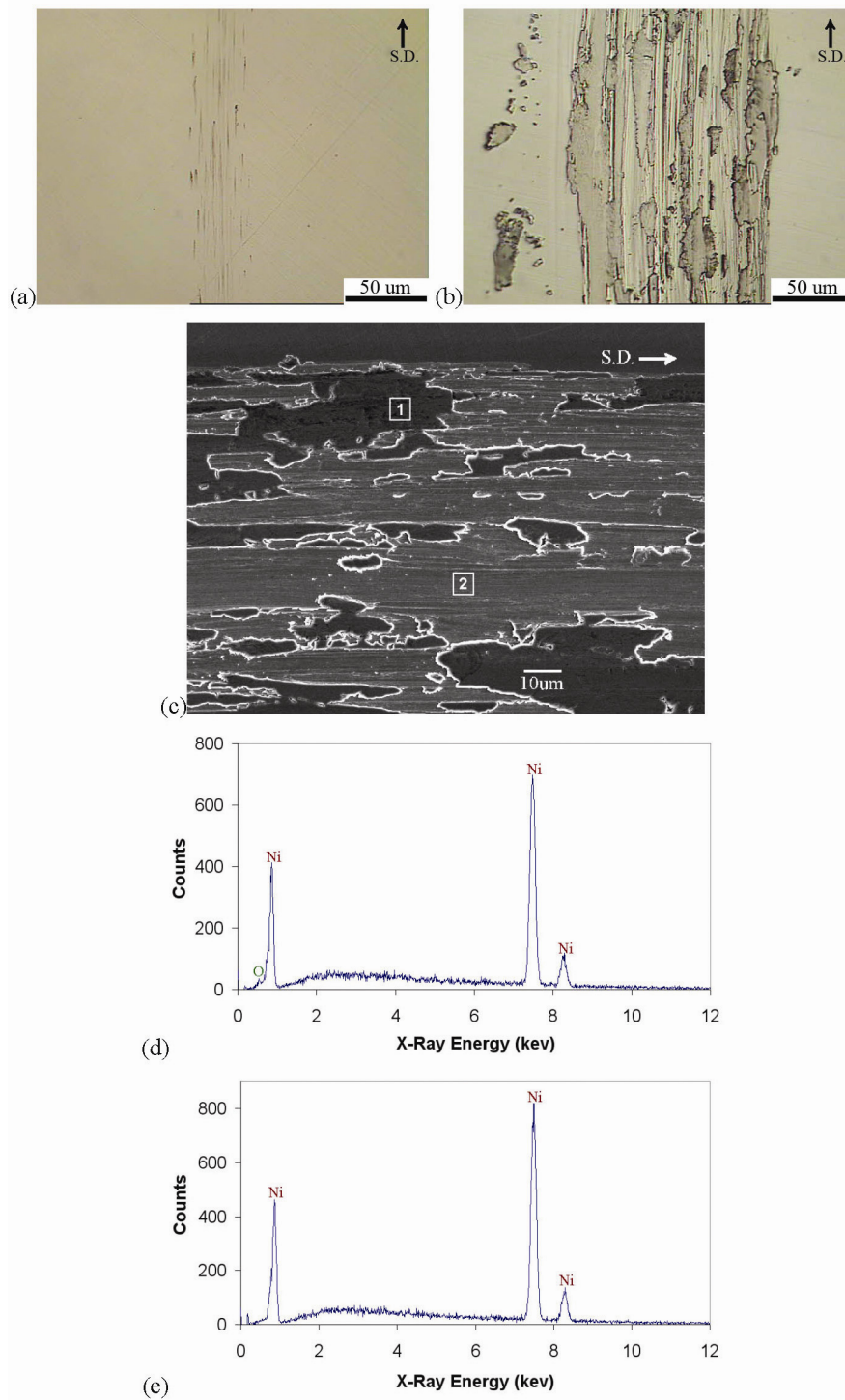
Figure 11. (a,b) Optical micrographs of the NC Ni wear tracks formed after 8 and 10^3 sliding cycles in dry argon. (c) SEM micrograph of the track shown in (b). (d) EDS spectra of the area labelled 1 in (c). (e) EDS spectra of the area labelled 2 in (c).

CHAPTER 3

EFFECT OF SLIDING SPEED ON FRICTION AND WEAR BEHAVIOUR OF NANOCRYSTALLINE NICKEL TESTED IN AN ARGON ATMOSPHERE

1. INTRODUCTION

The increase in strength and hardness in nanocrystalline (NC) metals [1-4] due to the Hall-Petch strengthening [5, 6] may provide an opportunity for designing new materials and surfaces with improved wear resistance. Farhat et al. [7] tested magnetron sputtered NC Al using a pin-on-disc tribometer, and revealed that in the grain size (d) range of 15-100 nm the wear rate (W) of the NC Al was proportional to the applied load (P), a finding that is consistent with the Archard law [8], and obeyed the following equation at a constant velocity [7]:

$$W = W_0 + K\left[\frac{P}{H_0 + kd^{-0.5}}\right] \qquad (1)$$

where K is the wear coefficient, H_0 is the single crystal hardness and k is a constant representing "grain boundary strength".

The tribological behaviour of NC Ni films has also been studied. Among various techniques, electrolytic deposition produces NC Ni films with narrowly controlled grain size [9] and low defect density [10]. However, there are discrepancies in the data presented in the literature regarding the COF and wear rate of NC Ni, due to the differences in testing conditions used. Jeong et al. [11] measured the abrasive wear resistance of electrodeposited NC Ni coatings in ambient air using Taber wear testing,

and found a 44% increase in wear resistance for an NC Ni with d = 13 nm, compared to a microcrystalline (MC) Ni with d = 90 μm. Schuh et al. [12] employed a Berkovich-type indenter in ambient air to compare the scratch resistance of NC and MC Ni samples with grain sizes of 12 nm and 15 μm in ambient air, but no change was observed in the COF during the nanoscratch tests, with the same COF of 0.25 measured for both samples. In contrast, Mishra et al. [13] reported distinctly different COF values of 0.16 at d = 8 nm and 0.29 at d = 10 nm for electrodeposited NC Ni coatings using a fretting wear tester in ambient air. A COF of 0.62 was measured for an MC Ni with d = 61 μm. Wang et al. [14] reported that reducing grain size from 3 μm to 16 nm in electrodeposited Ni coatings led to a 75% reduction in wear rate and a 19% reduction in COF. A reciprocating pin-on-disc tribometer operating in ambient air was used in their experiments.

NC metals have a large density of grain boundaries that act as preferential nucleation sites for oxides [15], as well as providing high diffusion paths for oxygen. Thus, in studying tribological properties of NC metals, attention must be given to role of testing environment. Shafiei and Alpas [16] studied the role of the testing environment on the initial and steady-state wear behaviour of an NC Ni with d = 15 nm using pin-on-disc wear tests. In ambient atmosphere, the NC Ni showed a 25% lower peak COF, a 27% lower initial wear rate, a 29% lower steady-state COF and a 57% lower steady-state wear rate when compared to data obtained in an argon atmosphere. They observed that in ambient atmosphere, the formation of oxidized tribolayers on top of the steady-state wear track prevented the ploughing of the NC Ni's surface by the counterface. The tribolayers formed in the argon atmosphere were discontinuous and had a much lower oxygen content, making them less protective than the ones formed in air.

The strain-rate sensitivity of NC Ni's strength and ductility has been observed in both computational simulations and experimental investigations [17-21]. The strong strain-rate sensitivity of flow stress observed in NC Ni (and also in NC Cu [22-24]), suggests the possibility that NC metals are highly sensitive to slight changes in sliding speed, so, although hardness is considered to be the main factor in examining the tribological performance of NC metals compared to their MC counterparts [11-14, 25], the effect of sliding speed on their wear resistance must be studied to achieve a comprehensive analysis. This work explores effect of sliding speed on the friction and wear properties of electrodeposited NC Ni.

In studying the effects that the mechanical properties of NC metals have on their tribological behaviour, oxidational wear mechanisms should be avoided as shown in our previous work [16]. Accordingly, in this work the sliding tests were performed in an argon environment in an effort to reduce the atmospheric effects, specifically to restrict surface oxidation. The micromechanisms of wear in NC Ni were characterized, and microscopic processes leading to the generation of wear debris and surface damage at different sliding speeds were studied.

2. EXPERIMENTAL PROCEDURES

2.1. Microstructure

Samples were 0.20 mm thick sheets of electrodeposited NC Ni (99.8% purity) supplied by Goodfellow Cambridge Ltd. (Huntingdon, England). For comparison, Ni foils with 99.98% purity and a thickness of 0.25 mm were also obtained from the same supplier and subjected to the indentation and sliding tests. Prior to the tests, the surfaces

of both MC Ni and NC Ni samples were polished to a similar roughness using a 1 μm diamond suspension. During polishing, a pressure much lower than the Hertzian pressure applied during the sliding tests (i.e. σ_H = 1.56 GPa, as is shown in Section 4.1) was exerted to the samples' surfaces to avoid polishing-induced effects on the mechanical and tribological properties of the samples.

Figure 1 shows the X-ray diffraction (XRD) spectra of the MC Ni and NC Ni. The MC Ni had a (200) preferential orientation, while the NC Ni had a slightly stronger (111) texture. The XRD pattern of the MC Ni exhibited narrow diffraction peaks (Figure 1a), whereas the NC Ni displayed a pronounced line broadening effect (Figure 1b). The grain size of the NC Ni was determined by measuring the half-peak breadth of the (111) peaks. The instrumental broadening (B_S) was estimated by measuring the half-peak breadth of the (111) peak of the MC Ni. Broadening due to microstructural refinement in the NC Ni (B) was calculated using [26]:

$$B^2 = B_M^2 - B_S^2 \tag{2a}$$

where B_M is the half-peak breadth measured in the (111) peak of the NC Ni. Then, the grain size of the NC Ni was determined using [27]:

$$d = \frac{0.9\,\lambda}{B\,\cos\theta} \tag{2b}$$

where λ is the wavelength of the X-ray used (Cu K_α radiation) and θ is the Bragg angle of the (111) peak. Using Equations 2a,b, the grain size of the NC Ni was calculated as 13.6 nm.

Figure 2 shows a bright field transmission electron microscopy (TEM) image of the NC Ni. Using the conventional linear intercept method on several TEM micrographs (at least 100 grains were used), the average grain size was measured as 15±3 nm, in

agreement with the grain size determined by the XRD line broadening technique. The grain size of the MC Ni was measured as 20±5 μm, also using the linear intercept method.

2.2. Mechanical Property Measurements

Using an indentation load of 1 N, the Vickers microhardness of the NC Ni was measured as 5.09±0.11 GPa (519±11 HV), while that of the MC Ni measured was 1.20±0.05 GPa (122±5 HV) under the same load.

A Hysitron nanoindentation system was employed to obtain indentation load-depth curves using a spherical indenter with a radius of 5 μm at a loading and unloading rate of 0.1 mN/s. Each indentation test consisted of nine partial unloading steps to 40% of the highest applied load for each loading step in increments from 0 to 9 mN. At the end of this stepwise loading and partial unloading sequence, i.e. at the maximum load of 10 mN, the indenter was completely unloaded.

In order to determine nanohardness values from the load-depth curves, the actual radius of the projected contact area, a_c', was calculated according to the procedure presented in Appendix B. Then, the nanohardness values were determined using:

$$H = \frac{P}{\pi a_c'^2}$$
(3)

2.3. Friction and Wear Tests

A pin-on-disc type tribometer with an environmental enclosure was used to conduct the wear tests under the unlubricated sliding conditions in a dry argon atmosphere (< 0.2% relative humidity). During the tests, argon gas was injected into the test chamber at

a flow rate of 10^{-3} m^3/s. The sliding wear tests were conducted for 8 cycles under a constant normal load of 2 N at three sliding speeds of 0.2×10^{-2}, 0.8×10^{-2} and 3.0×10^{-2} m/s. An alumina (Al$_2$O$_3$) ball with a hardness of 18.64±0.39 GPa and a diameter of 3.18 mm was fixed at the end of the pin and used as the counterface material.

The wear track morphologies were investigated by an optical interferometric surface profilometer and a scanning electron microscope (SEM) equipped with an energy dispersive spectroscopy (EDS) system. The volumetric wear loss, V, was measured according to the procedure given in the ASTM Standard G99 [28] using:

$$V = 2\pi R \left[r^2 \sin^{-1} \left(\frac{w}{2r} \right) - \left(\frac{w}{4} \right) \sqrt{4r^2 - w^2} \right] \qquad (4)$$

where R and w are the radius and the average width of the wear track, and r is the radius of the counterface ball. The wear rate, W, was computed from the slope of the volume loss vs. sliding cycles curve:

$$W = \frac{1}{2\pi R} \left(\frac{\Delta V}{\Delta N} \right) \qquad (5)$$

where ΔV is volume loss within an interval of ΔN sliding cycles.

An indentation load of 0.1 N was used to determine the Vickers microhardness of the contact surfaces of the samples after the sliding tests.

3. RESULTS

3.1. Mechanical Properties

The nanoindentation tests were done on the MC Ni and NC Ni to gain insight into the differences between their surface deformation behaviour. Variations in indentation depth with applied load (up to 10 mN) for typical nanoindentations made on the surfaces of the

MC Ni and NC Ni are plotted in Figure 3a. Figure 3b shows the nanohardness values of both samples at different indentation loads calculated according to Equation 3 and using the data extracted from Figure 3a. For both MC Ni and NC Ni, nanohardness values measured were independent of the indentation load for all loads except for loads < 3 mN in the NC Ni. At 9 mN, the largest load at which partial unloading was conducted, the nanohardness values of the MC Ni and NC Ni were 1.26±0.08 and 3.36±0.10 GPa, respectively (data point 9 in Figure 3b). At 10 mN, the nanohardness values calculated after complete unloading (data point 10 in Figure 3b) were 1.31±0.08 GPa for the MC Ni and 5.12±0.15 GPa for the NC Ni. These values were comparable to the Vickers microhardness values of 1.20±0.05 GPa for the MC Ni and 5.09±0.11 GPa for the NC Ni using an indentation load of 1 N. Clearly, the hardness measured upon complete removal of the indentation load (data point 10 in Figure 3b) was higher than those measured at the last partial unloading step (data point 9 in Figure 3b) particularly in the case of the NC Ni, because the projected area of the indentation impression obtained upon complete removal of the load was smaller.

According to Figure 3a, under the highest load of 10 mN, the maximum indentation depth of the NC Ni was h_{max}^{nc} = 96.5 nm, 56% smaller than that of the MC Ni (h_{max}^{mc} = 220.0 nm). The maximum indentation depth, h_{max}, and the residual depth after the complete unloading of the indenter, h_f, can be used in determining the elastic depth recovery ratio, δ, as:

$$\delta = \frac{h_{max} - h_f}{h_{max}}$$ (6)

According to Equation 6, the δ value measured for the NC Ni was 400% larger than that for the MC Ni, which was measured under the same loading conditions (i.e. δ^{mc} =

0.095 and δ^{nc} = 0.479). A large elastic depth recovery ratio infers that a large portion of the surface deformation that occurs during sliding wear can be recovered after complete unloading.

3.2. Friction and Wear Behaviour

Variations in Wear Rates and COFs with Sliding Speed

Variations in wear rates with speed were determined for both MC Ni and NC Ni using Equations 4 and 5 and are plotted in Figure 4. The wear rates of the MC Ni were almost constant, and showed only a slight increase with the increase of the test speed (i.e. 8.16×10^{-3}, 8.47×10^{-3} and 8.78×10^{-3} mm^3/m at the speeds of 0.2×10^{-2}, 0.8×10^{-2} and 3.0×10^{-2} m/s). In the case of the NC Ni, the wear rates were 3.44×10^{-3}, 2.16×10^{-3} and 0.47×10^{-3} mm^3/m at the same sliding speeds. Thus, it follows that an increase in sliding speed from 0.2×10^{-2} to 3.0×10^{-2} m/s caused an 86% reduction in the wear rate of the NC Ni.

COF was measured as a function of sliding cycles during the tests at the constant sliding speeds (Figure 5). Variations in the MC Ni's COF during 8 sliding cycles at different speeds are given in Figure 5a. The trend of all the COF curves was similar, despite the experimental scattering. In the case of the NC Ni tested over the same speed range, a clear difference between the trends of the COF curves was observed (Figure 5b). The average COFs of the MC Ni and NC Ni are plotted as a function of sliding speed in Figure 6. For the MC Ni, the average COF was found to remain almost constant within the speed range of 0.2×10^{-2} to 3.0×10^{-2} m/s. Within this range, the lowest average COF was 0.57±0.05 and the highest value was 0.61±0.04. However, increasing the sliding

speed from 0.2×10^{-2} to 3.0×10^{-2} m/s caused a 31% increase in the average COF of the NC Ni, i.e. from 0.49±0.05 to 0.64±0.06.

<u>Changes in Contact Surface Morphologies</u>

After 8 sliding cycles, the MC Ni's wear tracks displayed similar features, regardless of the testing speed used. The average width (109 μm) and the average maximum depth (0.45 μm) of the wear track were constant over the applied speed range. According to the 3-D surface profiles shown in Figures 7a-c, wear tracks were characterized by plastic deformation induced by the indentation of the counterface. Also, pile-ups of deformed material were seen at the edges of the wear tracks, which was a result of material displacement during plastic deformation. No change was observed in the wear mechanism of the MC Ni over the investigated sliding speed range. This was not the case for the NC Ni. At the lowest sliding speed of 0.2×10^{-2} m/s, the wear track of the NC Ni displayed continuous surface scratches as a result of counterface ploughing action (Figure 7d). The surface scratches on the NC Ni's contact surfaces decreased in both number and depth as the sliding speed was increased (Figures 7e,f). Consequently, the average width of the wear track decreased from 80.7 to 41.6 μm and its average maximum depth decreased from 0.40 to 0.20 μm when the sliding speed was increased from 0.2×10^{-2} to 3.0×10^{-2} m/s. Therefore, while the NC Ni's wear track became smaller (consistent with the reduction in its wear rate), its COF increased as the sliding speed increased.

Changes in Chemical State and Hardness of Contact Surfaces

The EDS analyses performed on the MC Ni's wear tracks did not reveal any detectable amounts of oxygen at either of the sliding speeds used, indicating that the MC Ni's surfaces remained practically unoxidized during the sliding tests. On the other hand, large quantities of debris particles were generated on the NC Ni's contact surfaces at lower sliding speeds, prompting the formation of tribolayers on the wear tracks. These layers were, however, discontinuous, and did not entirely cover the surfaces of the wear tracks. Figure 8 shows an SEM micrograph of the wear track formed on the NC Ni's surface at the lowest sliding speed of 0.2×10^{-2} m/s. No evidence of surface oxidation could be obtained from the EDS measurements made in the areas of this wear track that were not covered by the tribolayers. However, the tribolayers built up on the wear track contained small amounts of oxygen (maximum 3.3 at.% oxygen). It is known that NC Ni has a higher tendency for oxidation due to its higher density of grain boundaries compared to MC Ni [15]. Thus, the presence of small amounts of oxygen in the test chamber may have led to the formation of the partially-oxidized tribolayers on the NC Ni's contact surfaces. Higher sliding speeds produced lesser coverage of wear tracks by the same type of tribolayers, because smaller amounts of debris particles were generated as a result of the lower wear rate.

The results of the Vickers microhardness measurements made on the wear tracks using a load of 0.1 N are shown in Figure 9. These wear track hardness values represent the averages of ten measurements made on both the worn surfaces and the tribolayers formed on them. For the MC Ni, a 23% increase in hardness was measured after the sliding tests. This hardness increase was a result of the strain hardening of the MC Ni's

surfaces during the sliding wear and was independent of the sliding speed. In the case of the NC Ni, the increase in the contact surface hardness was a function of the sliding speed. The contact surfaces of the NC Ni tested at 0.2×10^{-2} and 0.8×10^{-2} m/s revealed 14% and 12% increases in hardness, respectively, compared to the hardness of the NC Ni's original surface. The NC Ni samples tested at the highest sliding speed of 3.0×10^{-2} m/s did not show any increase in hardness. As the yield strength of NC Ni is high, the contribution of surface strain hardening to the measured worn surface hardness of NC Ni should be smaller than that of the MC Ni. The increase in the hardness of the contact surfaces during the wear at the low speeds can be attributed to the tribolayer coverage of the worn surfaces.

4. DISCUSSION

The test results have shown that the wear rates of the NC Ni decrease as a result of increasing the test speed, while the MC Ni's wear rates remain relatively insensitive to changes in sliding speed. In this section, the wear mechanisms in the NC Ni and MC Ni are discussed, and then the speed sensitivity of the NC Ni is considered. An analysis is presented based on the Archard equation to predict wear rates of Ni as a function of grain size and sliding speed.

4.1. Wear Mechanisms of Nanocrystalline Nickel in Comparison with Microcrystalline Nickel

The damage mechanisms in the NC Ni subjected to sliding wear differed from the ones observed for the MC Ni. In the case of the MC Ni, wear was initiated by the large

plastic deformation induced by the contact stresses. The initial Hertzian stress applied to the contact surface can be estimated using [29]:

$$\sigma_H = 0.918 \ \sqrt[3]{\frac{P}{D^2 C^2}}$$

(7a)

where P = 2 N is the applied normal load, D = 3.18 mm is the counterface ball diameter and C is the effective elastic modulus defined as:

$$C = \left(\frac{1-v_1^2}{E_1}\right) + \left(\frac{1-v_2^2}{E_2}\right)$$

(7b)

The elastic moduli and the Poisson's ratios of micro- and nano-crystalline forms of Ni do not differ much [4]. The effective elastic modulus (C) is calculated using Equation 7b and using E_1 = 200 GPa and v_1 = 0.31 for both MC Ni and NC Ni, and E_2 = 350 GPa and v_2 = 0.24 for Al_2O_3. Accordingly, the initial contact pressure was σ_H = 1.56 GPa, approximately four times higher than the MC Ni's yield strength estimated at σ_y = 0.40 GPa from its hardness (H) as σ_y = H/3 [7]. On the other hand, in the NC Ni with an estimated σ_y = 1.70 GPa, the initial contact is less likely to induce indentation plastic deformation under the same test load of 2 N. This analysis is consistent with the experimentally observed wear track morphologies (Figure 7), which indicated that almost no plastic deformation damage occurred on the NC Ni's surface whereas in the MC Ni, substantial plastic deformation of the contact surface and piling-up of material around the wear track (to accommodate displacement due to the sinking-in of the indenter) was observed.

The results of the nanoindentation tests presented in Section 3.1 suggest that some of the total deformation induced by the sliding counterface might have been recovered upon the release of the stress applied by the counterface. The elastic recovery of the surface

deformation after the passage of the indenter would help to reduce the severity of the surface damage induced during the course of sliding. Hence, this could be an additional factor in reducing the wear damage in the case of the NC Ni due to its larger elastic recovery ratio.

In summary, the lesser amount of wear damage observed in the NC Ni at any given speed could be attributed to two factors: i) the high yield strength of the NC Ni, which limits the extent of plastic deformation at the applied contact stress level and ii) the large elastic recovery ratio that restores a portion of the total deformation upon the passage of the counterface.

4.2. A Phenomenological Analysis of Wear Rate - Sliding Speed Relationship

In Figure 10a the wear rates of the MC Ni and NC Ni measured at three different speeds are plotted against their original microhardness values. The Archard-type equations that best fit the experimental data obtained in the studied range are presented in the legend of this figure. The tests performed at the speed of 0.8×10^{-2} m/s followed the Archard equation, but a relatively small increase or decrease in sliding speed in the NC regime caused significant deviations from Archard's prediction. The Archard-type equations in Figure 10a have the following general form:

$$W = KP \left[\frac{1}{H} \right]^{\alpha} \tag{8}$$

where K (wear coefficient) and α (wear exponent) should depend on sliding speed. Variations in K and α with sliding speed are plotted in Figures 10b, c. Accordingly, Equation 8 yields:

$$W = K(v)P \left[\frac{1}{H_0 + kd^{-0.5}} \right]^{\alpha(v)} \tag{9}$$

where H_0 and k are Hall-Petch parameters as in Equation 1. For Ni, Equation 9 can be used to predict wear rates of NC Ni as a function of grain size and sliding speed using:

$$\begin{cases} K = 0.0603v + 0.0045 \\ \alpha = 50.3990v + 0.5156 \end{cases} \tag{10}$$

4.3. Micromechanisms Responsible for the Sliding-Speed Sensitivity in Nanocrystalline Nickel

Wear mechanisms in NC Ni would be sensitive to changes in the surface deformation rate at different sliding speeds. An increase in the sliding speed during the wear test is expected to cause an increase in the rate of the application of the shear strain to the contact surface. It was shown that increasing the strain rate during the tensile and indentation tests leads to enhancements in yield strength of electrodeposited NC Ni [17-21]. Plastic deformation mechanisms in nanocrystalline metals and alloys that consist of large volume fractions of grain boundaries include grain-boundary sliding and dislocation emission at grain boundaries [17-19, 30-33]. Since these mechanisms are time-dependent, the deformation of NC Ni becomes increasingly difficult at higher strain rates. Hence, during high speed sliding tests, plastic deformation would become more difficult, leading to less extensive surface damage compared to the tests carried out at lower speeds. This is consistent with the observation that the severity of NC Ni's surface damage reduced at higher speed tests (Figures 7d-f). As a result, NC Ni's wear rate decreased when this material was tested at higher speeds (Figure 4). The strong strain-rate sensitivity observed in NC Ni is absent in MC Ni [20], a fact that is consistent with the observation that the

MC Ni's wear rate (Figure 4) and wear mechanism (Figures 7a-c) were independent of sliding speed. On the other hand, the COF of the NC Ni increased with the sliding speed (Figure 5). At lower sliding speeds, the protective tribolayers that formed on the surfaces of the NC Ni were responsible for the lower COF values. Smaller tribolayer coverage at the higher speeds led to lower surface and higher COF values. The COF of MC Ni was practically independent of sliding speed over the same speed range as there was no change in the amount of tribolayers formed on the surface.

5. CONCLUSIONS

The friction and wear behaviour of a nanocrystalline (NC) Ni with a grain size of 15±3 nm was investigated as a function of sliding speed in comparison with a microcrystalline (MC) Ni with a grain size of 20±5 µm using a pin-on-disc tribometer operated in an argon environment. The main conclusions arising from this study are as follows:

1. Sliding wear of the MC Ni was characterized by indentation-induced plastic deformation inflicted by the counterface, and material pile-up at the edges of the wear tracks. In contrast, in the case of the NC Ni, the wear tracks were narrower and wear occurred by material removal as a result of surface scratching rather than indentation-induced deformation. The lesser wear damage observed in the NC Ni compared to the MC Ni is attributed to the NC Ni's higher hardness and greater deformation recovery ratio.

2. The NC Ni's wear rate was a strong function of the sliding speed. Increasing the test speed over the relatively small range of 0.2×10^{-2} to 3.0×10^{-2} m/s caused an 86%

reduction in the NC Ni's wear rate from 3.44×10^{-3} to 0.47×10^{-3} mm^3/m. A modified Archard equation was proposed to predict wear rates of Ni as a function of grain size and sliding speed.

3. As the sliding speed increased in the case of the NC Ni, damaging the surface became increasingly difficult. This is attributed to the fact that the grain-boundary-induced deformation mechanisms are more difficult to operate at higher strain rates. In contrast, the MC Ni's wear rate remained virtually constant over the same speed range.

4. The COF of the NC Ni showed an increase of 31% from 0.49 to 0.64 when the sliding speed increased from 0.2×10^{-2} to 3.0×10^{-2} m/s. At the lower sliding speeds, the protective tribolayers formed on the surfaces of the NC Ni were responsible for the lower COF values. The smallest amount of debris generated at the highest sliding speed was not sufficient to form protective tribolayers, leading to a high COF value. The COF of the MC Ni was practically independent of sliding speed over the same speed range.

REFERENCES

[1]   C.C. Koch, D.G. Morris, K. Lu, A. Inoue, Mater. Res. Soc. Bull. 24 (1999) 54.

[2]   J.R. Weertman, D. Farkas, K. Hemker, H. Kung, M. Mayo, R. Mitra, H. Van Swygenhoven, Mater. Res. Soc. Bull. 24 (1999) 44.

[3]   H. Van Swygenhoven, J.R. Weertman, Scripta Mater. 49 (2003) 625.

[4]   K.S. Siow, A.A.O. Tay, P. Oruganti, Mater. Sci. Tech. 20 (2004) 285.

[5]   E.O. Hall, Proc. Phys. Soc. 64 (1951) 747.

[6]   N.J. Petch, J. Iron Steel Inst. 174 (1953) 25.

[7]   Z.N. Farhat, Y. Ding, D.O. Northwood, A.T. Alpas, Mater. Sci. Eng. A206 (1996) 302.

[8]   J.F. Archard, J. Appl. Phys. 24 (1953) 981.

[9]   A.P. Zhilyaev, J. Gubicza, G. Nurislamova, A. Revesz, S. Surinach, M.D. Baro, T. Ungar, Phys. Stat. Sol. A198 (2003) 263.

[10] L.L. Shaw, JOM 52 (2000) 41.

[11] D.H. Jeong, F. Gonzalez, G. Palumbo, K.T. Aust, U. Erb, Scripta Mater. 44 (2001) 493.

[12] C.A. Schuh, T.G. Nieh, T. Yamasaki, Scripta Mater. 46 (2002) 735.

[13] R. Mishra, B. Basu, R. Balasubramaniam, Mater. Sci. Eng. A373 (2004) 370.

[14] L. Wang, Y. Gao, T. Xu, Q. Xue, Mater. Chem. Phys. 99 (2006) 96.

[15] S.H. Kim, U. Erb, K.T. Aust, F. Gonzalez, G. Palumbo, Plat. Surf. Finish. May (2004) 68.

[16] M. Shafiei, A.T. Alpas, Metall. Mater. Trans. A38 (2007) 1621.

[17] K.S. Kumar, S. Suresh, M.F. Chisholm, J.A. Horton, P. Wang, Acta Mater. 51 (2003) 387.

[18] K.S. Kumar, H. Van Swygenhoven, S. Suresh, Acta Mater. 51 (2003) 5743.

[19] F. Dalla Torre, H. Van Swygenhoven, M. Victoria, Acta Mater. 50 (2002) 3957.

[20] R. Schwaiger, B. Moser, M. Dao, N. Chollacoop, S. Suresh, Acta Mater. 51 (2003) 5159.

[21] F. Dalla Torre, H. Van Swygenhoven, R. Schaublin, P. Spatig, M. Victoria, Scripta Mater. 53 (2005) 23.

[22] D. Jia, K.T. Ramesh, E. Ma, L. Lu, K. Lu, Scripta Mater. 45 (2001) 613.

[23] L. Lu, S.X. Li, K. Lu, Scripta Mater. 45 (2001) 1163.

[24] E.M. Bringa, A. Caro, Y. Wang, M. Victoria, J.M. McNaney, B.A. Remington, R.F. Smith, B.R. Torralva, H. Van Swygenhoven, Science 309 (2005) 1838.

[25] T. Hanlon, A.H. Chokshi, M. Manoharan, S. Suresh, Int. J. Fatigue 27 (2005) 1159.

[26] B.E. Warren, J. Biscoe, J. Amer. Ceram. Soc. 21 (1938) 49.

[27] D. Lewis, E.J. Wheeler, D.O. Northwood, J. Edu. Modul. Mater. Sci. Eng. 4 (1982) 665.

[28] Friction and Wear Testing, ASM, Materials Park, OH, 1997, pp. 124-128.

[29] Metals Handbook, 1st ed., ASM, Materials Park, OH, 1992, vol. 18, pp. 480-488.

[30] F. Ebrahimi, G.R. Bourne, M.S. Kelly, T.E. Matthews, Nanostruct. Mater. 11 (1999) 343.

[31] H. Van Swygenhoven, P.M. Derlet, Phys. Rev. B64 (2001) 1.

[32] A.G. Froseth, P.M. Derlet, H. Van Swygenhoven, Acta Mater. 52 (2004) 5863.

[33] H. Van Swygenhoven, A. Caro, D. Farkas, Mater. Sci. Eng. A309-310 (2001) 440.

FIGURES
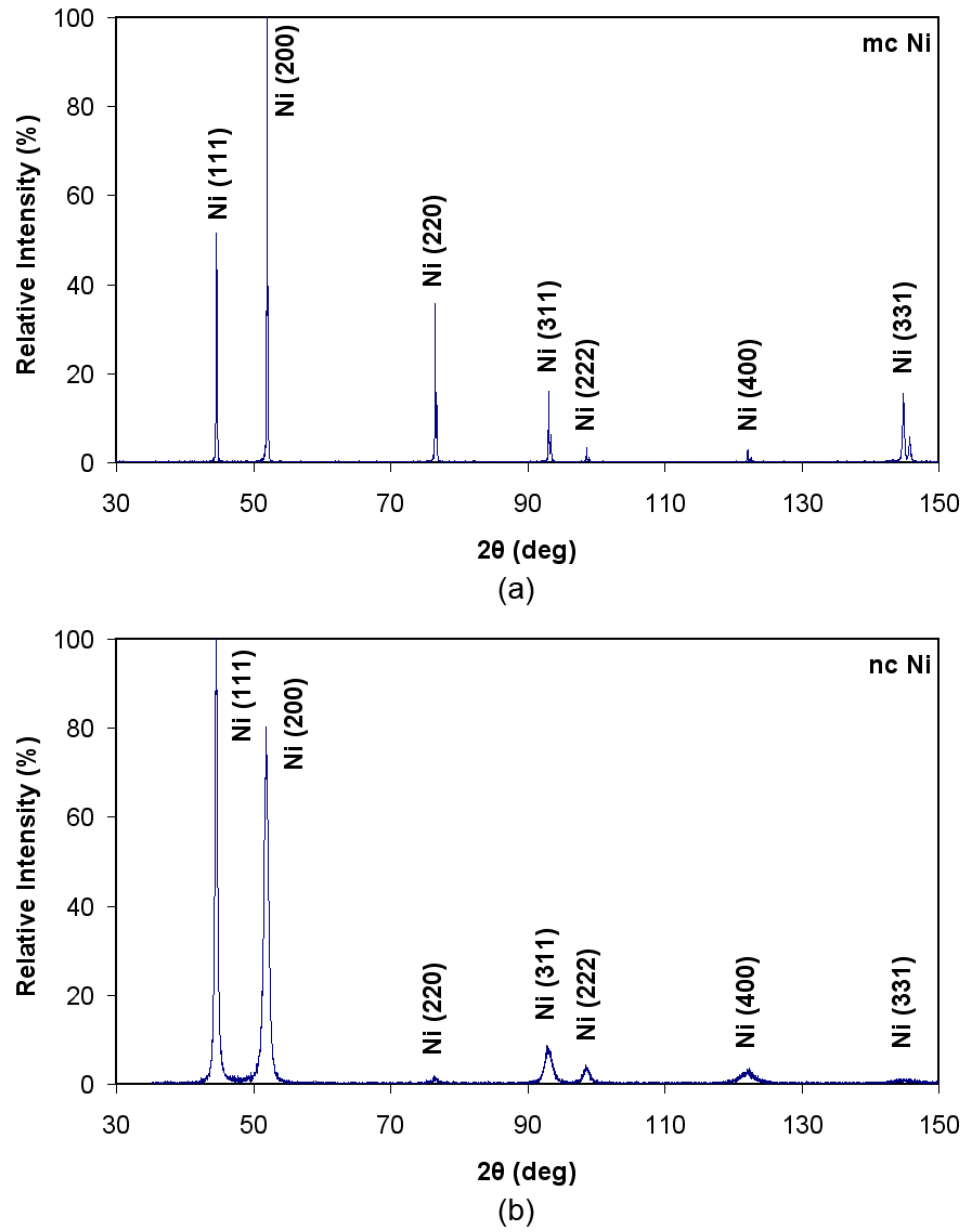
Figure 1. XRD patterns of: (a) the MC Ni, and (b) the NC Ni.
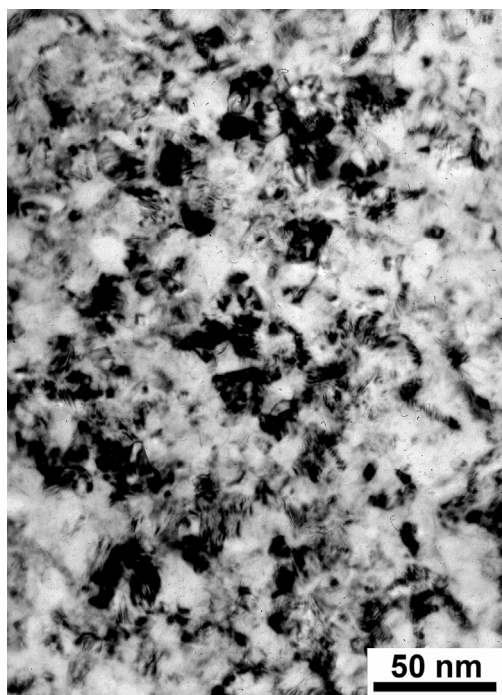
Figure 2. A bright field TEM image of the NC Ni.
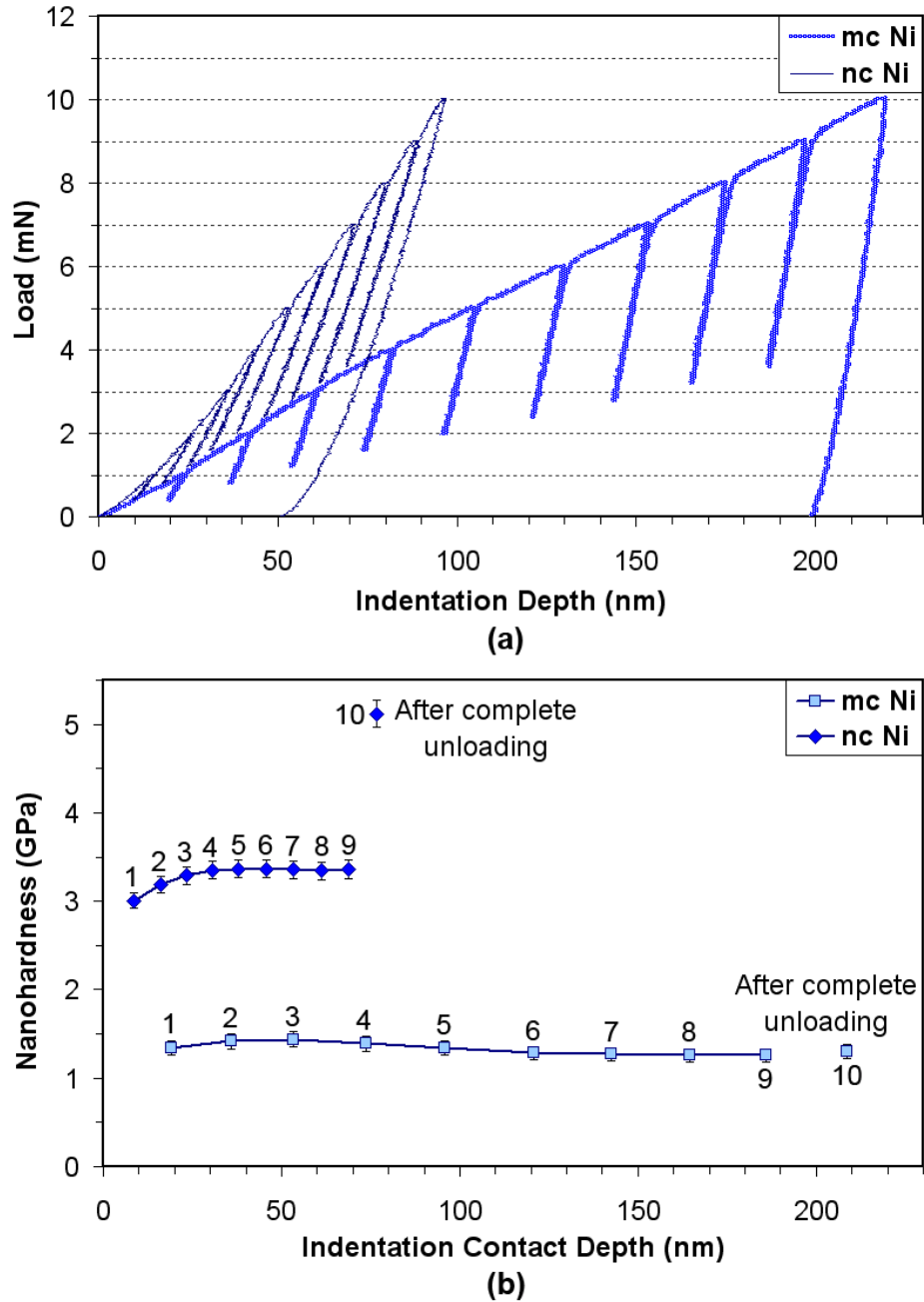
Figure 3. (a) Load-depth curves of typical nanoindentations on the MC Ni and NC Ni samples. (b) Variations in nanohardness value with indentation contact depth under load for the MC Ni and NC Ni. The last point in each series of data represents the nanohardness value calculated after complete unloading.
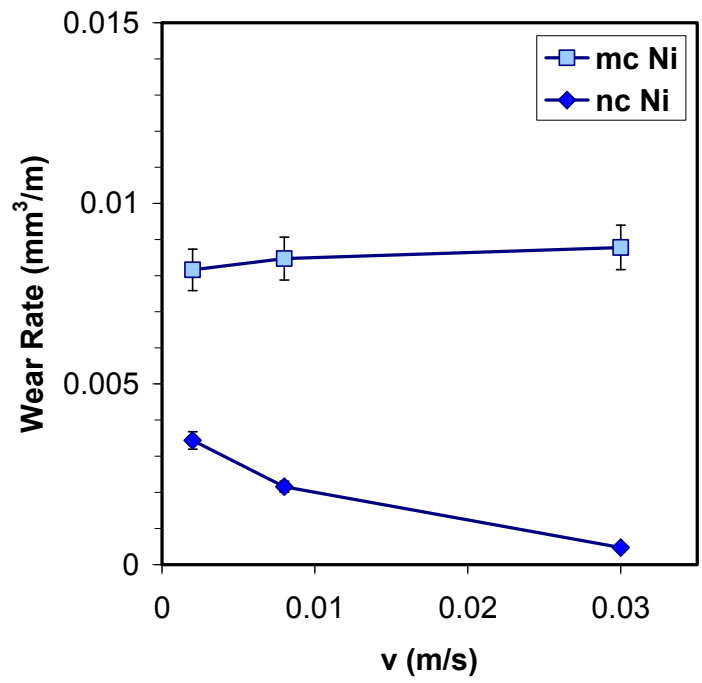
Figure 4. Wear rate vs. sliding speed for the MC Ni and NC Ni after 8 sliding cycles in the argon atmosphere.
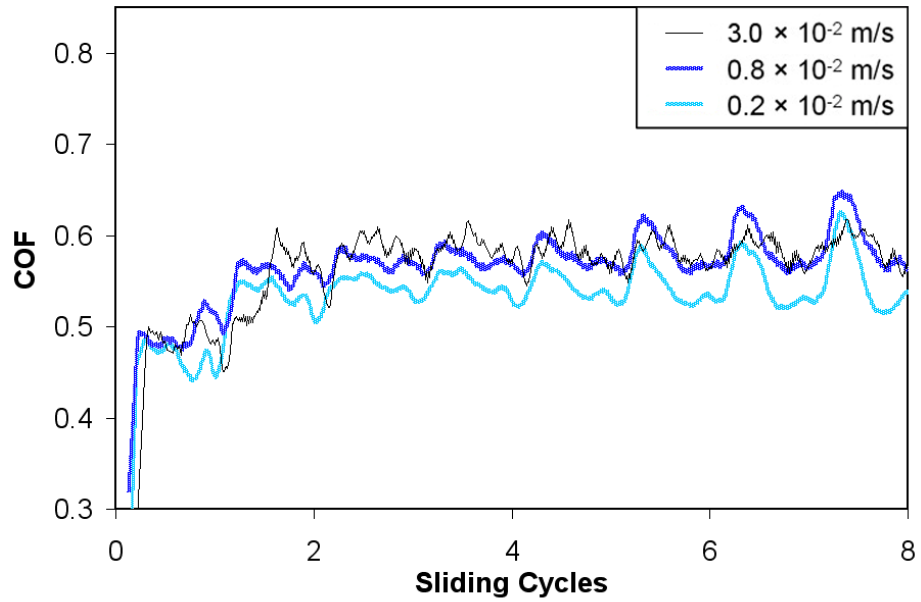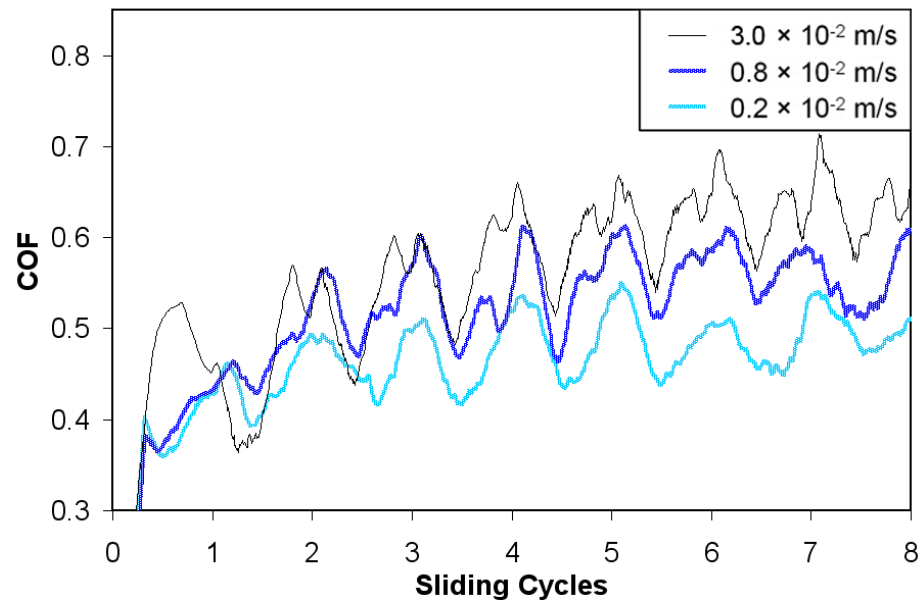
Figure 5. Variations in the COFs during 8 sliding cycles in the argon atmosphere at different speeds for: (a) the MC Ni, and (b) the NC Ni.
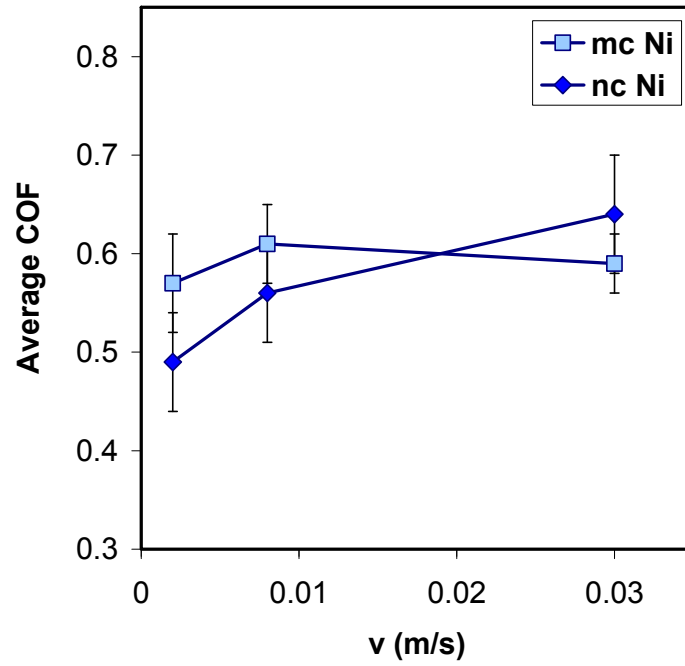
Figure 6. The average COFs of the MC Ni and NC Ni plotted as a function of sliding speed.
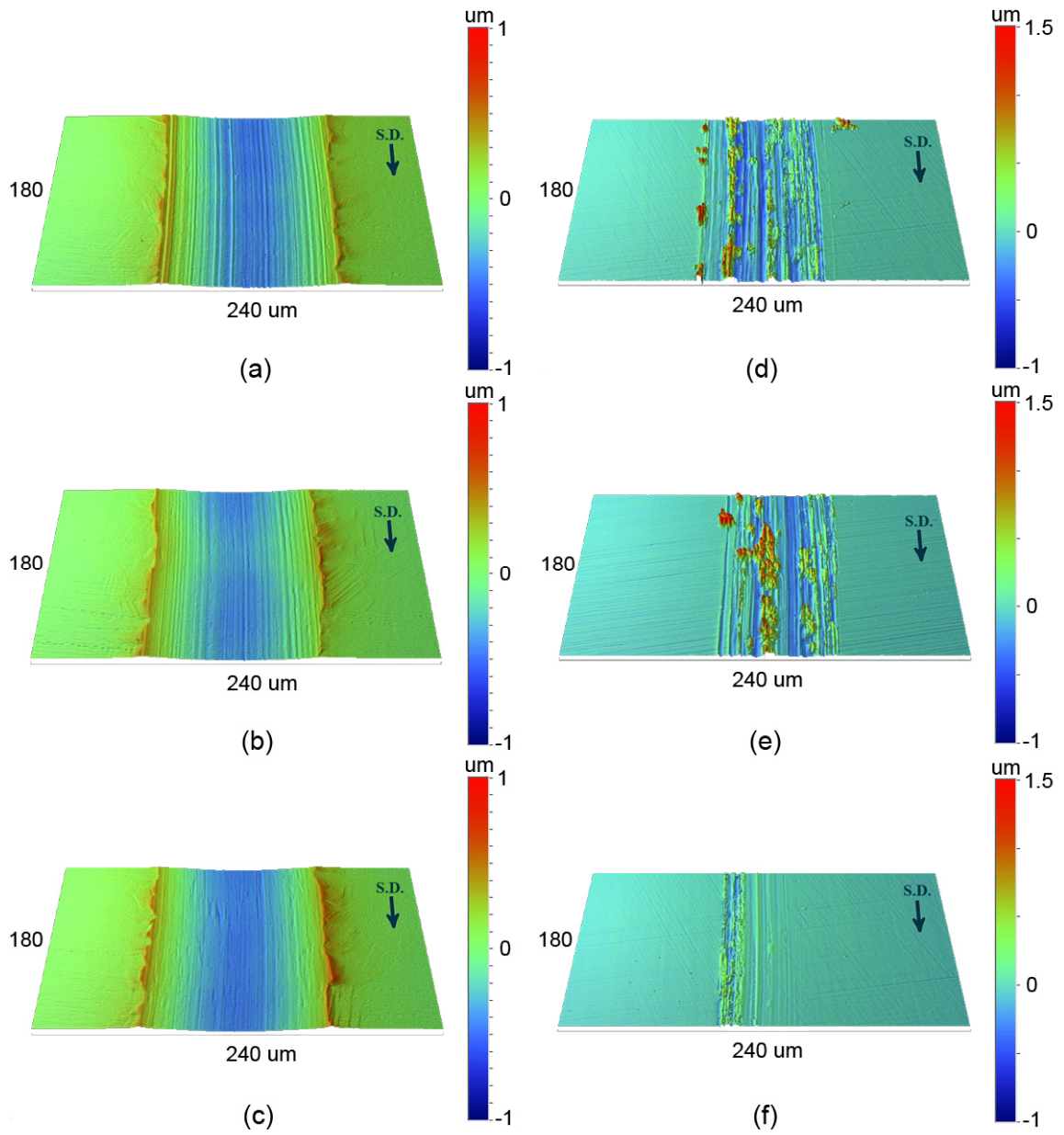
Figure 7. (a-c) 3-D surface profiles of the MC Ni's wear tracks after 8 sliding cycles in the argon atmosphere at speeds of (a) 0.2×10^{-2} m/s, (b) 0.8×10^{-2} m/s, and (c) 3.0×10^{-2} m/s. (d-f) 3-D surface profiles of the NC Ni's wear tracks after 8 sliding cycles in the argon atmosphere at speeds of (d) 0.2×10^{-2} m/s, (e) 0.8×10^{-2} m/s, and (f) 3.0×10^{-2} m/s.
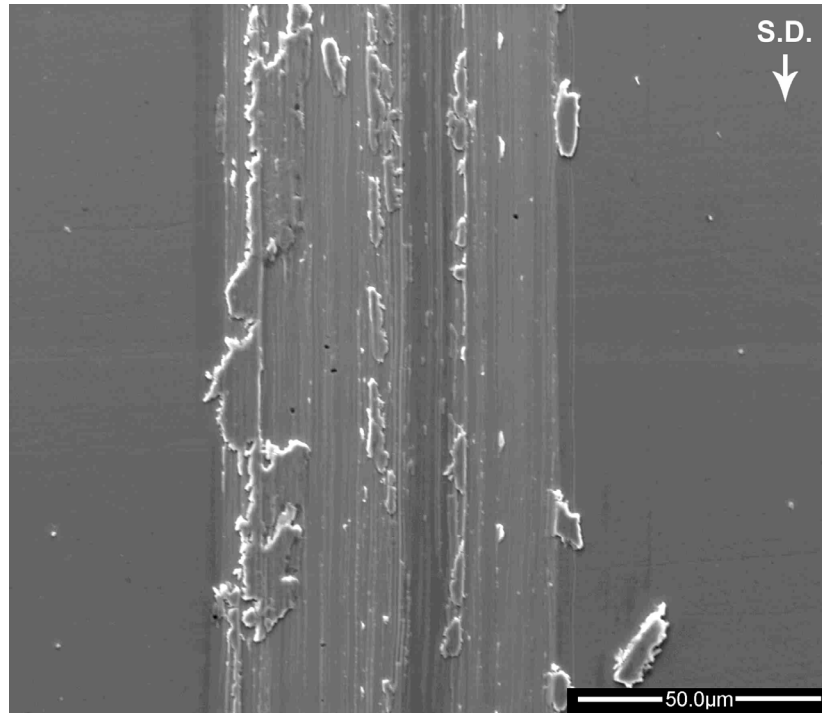
Figure 8. An SEM micrograph of the wear track formed on the NC Ni after 8 sliding cycles in the argon atmosphere at the lowest sliding speed (0.2×10^{-2} m/s).
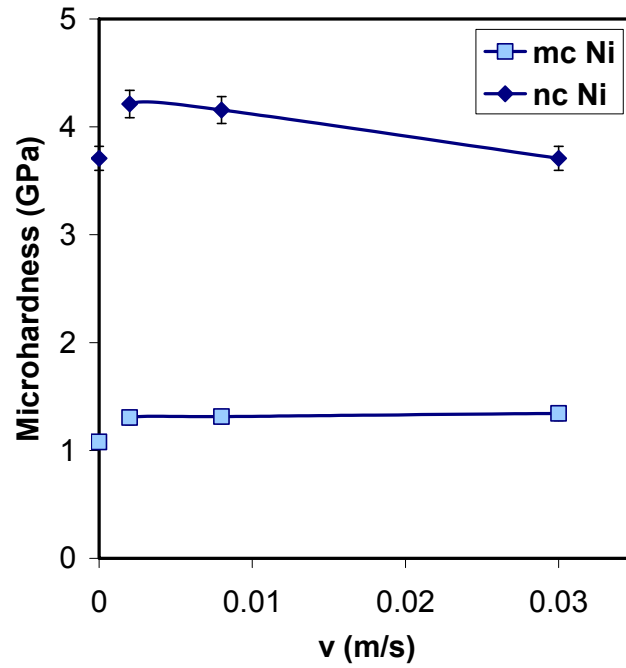
Figure 9. Microhardness values obtained from the wear tracks formed on the surfaces of the MC Ni and NC Ni at different sliding speeds. The data points at the velocity of 0 represent the microhardness values of the original surfaces prior to the wear tests. All measurements were made using a 0.1 N normal load.

(a)

(b)

$$\alpha = 50.399v + 0.5156$$
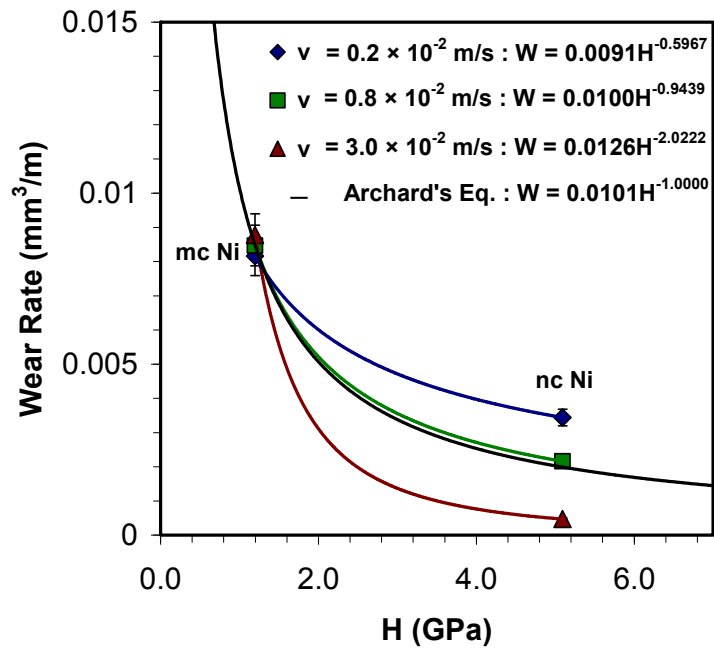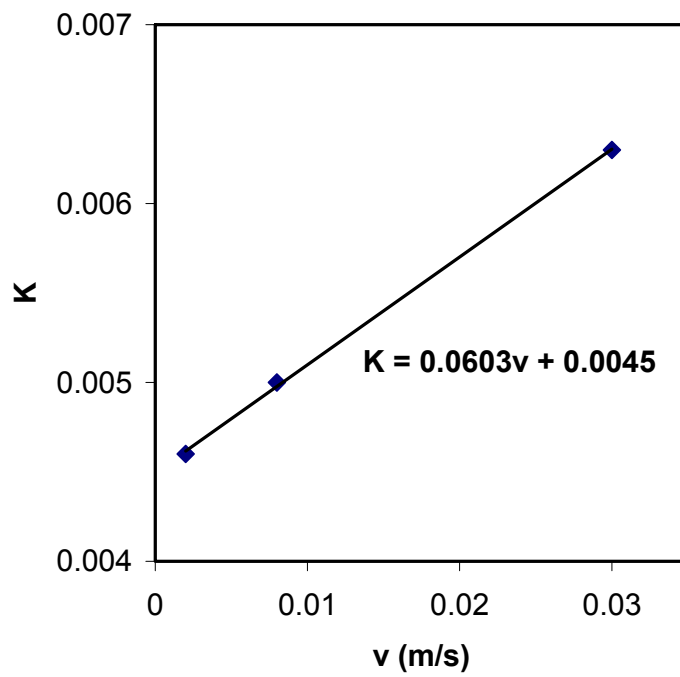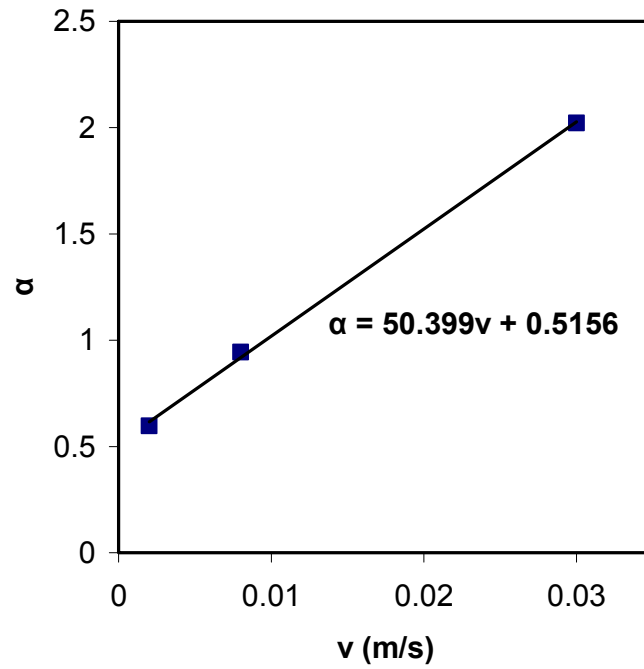
(c)

Figure 10. (a) Variations in wear rates of Ni samples with original microhardness at different sliding speeds. The legend shows the Archard-type equations that best fit the experimental data. (b) Variations in K (in Equation 9) with sliding speed. (c) Variations in α (in Equation 9) with sliding speed.

CHAPTER 4

HIGH-TEMPERATURE FRICTION AND WEAR MECHANISMS OF NANOCRYSTALLINE NICKEL COMPOSITE COATINGS

1. INTRODUCTION

Electrodeposition, among all the nanocrystalline (NC) metal fabrication techniques, provides fully dense NC structures with relatively narrow grain size distributions. Electrodeposited NC Ni displayed better mechanical [1-6] and tribological [7-10] properties at room temperature compared to microcrystalline (MC) Ni. However, NC Ni contains a large volume fraction of grain boundaries and triple junctions, which make it thermally unstable. Differential scanning calorimetry (DSC) studies [11,12] showed that three exothermic reactions would take place when annealing NC Ni deposits with a grain size of 10-20 nm: i) nucleation and abnormal grain growth in the 353-563 K range; ii) normal grain growth in the 563-643 K range; and iii) growth towards equilibrium in the 643-773 K range. The first reaction leads to a bimodal grain structure, while the second reaction results in a uniform structure of larger grains with impurity segregation to grain boundaries [13]. The third reaction transforms NC Ni to MC Ni.

The high-temperature tensile testing of as-deposited NC Ni samples [14,15] displayed a drastic drop in the films' strength, as well as a significant increase in their elongation at about 573 K. Testing the as-deposited NC Ni samples at about 473 K revealed that their strength was lower and their elongation was higher compared to the room temperature values, even though no significant change in their grain size was detected at this temperature. In another study, the creep behaviour of NC Ni deposits was investigated,

and the creep rate was found to be very sensitive to temperature [16]. While no grain growth was detected at 373 K, the creep rate measured at this temperature was two orders of magnitude larger than that measured at room temperature under a similar stress of 700 MPa. An increase in temperature from 273 K to 373 K could cause a transition in the creep mechanism from diffusion along grain boundaries and triple junctions to grain boundary sliding. High self-diffusivity and a large volume fraction of grain boundaries make NC Ni susceptible to creep at temperatures slightly higher than room temperature [1].

This study reports on the coefficients of friction (COF) and wear rates of electrodeposited NC Ni measured at room temperature and an elevated temperature (493 K). In order to enhance the high temperature tribological properties, micro and nanoparticles of SiC were added to the NC Ni films. The effects of SiC particles on the room temperature and high temperature friction and wear behaviour of NC Ni were explored by employing optical interferometry, as well as cross-sectional focussed ion beam (FIB) and transmission electron microscopy (TEM) techniques.

2. EXPERIMENTAL PROCEDURES

A Watt's bath was used to electrodeposit NC Ni films onto a Cu substrate (cathode) with a Pt anode, at a direct current density of 0.05 A/cm^2 and an electrolyte pH of 4.5, as well as an electrolyte temperature of 45 °C. The deposition duration for all the coatings was 45 minutes. The electrolyte was composed of 300 g/l $NiSO_4$, 45.0 g/l $NiCl_2$, 45.0 g/l HBO_3, 5.00 g/l saccharin and 0.25 g/l sodium lauryl sulfate. Under these conditions, NC Ni coatings with a grain size of 30±4 nm and a thickness of 63±6 μm were deposited. In

addition, two types of NC Ni matrix composite coatings were produced by adding 30 g/l SiC particles of either 5 μm (MP SiC) or 50 nm (NP SiC) in diameter to separate baths with the above-mentioned chemical composition. In order to reduce the agglomeration of nanoparticles, the electrolyte containing NP SiC was oscillated in an ultrasonic container for 10 minutes, prior to electrodeposition. Under these conditions, composite coatings containing 6.5±1.0 vol.% of SiC particles were obtained.

Scanning electron microscopy (SEM) images of the NC Ni-MP SiC and NC Ni-NP SiC coatings' surfaces appear in Figures 1a,b. Both coatings seem to have a uniform distribution of SiC particles in the NC Ni matrix. Nanoparticles tend to agglomerate inside the bath (due to their high surface energy), a characteristic that could potentially diminish the mechanical properties of the coating [17,18]. No agglomeration of the NP SiC could be detected in this work (see Figure 1b).

The Vickers microhardness of the coatings was measured using an indentation load of 100 gf. Incorporating SiC particles in NC Ni did not cause any significant increase in the hardness of this material (i.e., H(NC Ni) = 4.47±0.08 GPa, H(NC Ni-MP SiC) = 4.80±0.14 GPa and H(NC Ni-NP SiC) = 4.60±0.10 GPa). The microhardness values of the coatings after they were heated to 493 K and kept at that temperature for 10 minutes, then cooled down to room temperature (i.e., the heating cycle used in the high-temperature wear tests), were slightly higher than those of the as-deposited coatings (i.e., H^{ht}(NC Ni) = 4.59±0.09 GPa, H^{ht}(NC Ni-MP SiC) = 4.86±0.8 GPa and H^{ht}(NC Ni-NP SiC) = 4.64±0.09 GPa). This small increase was attributed to relaxations at the non-equilibrium grain boundaries during low-temperature annealing [13,19].

A CSM high-temperature, pin-on-disc tribometer was used to conduct dry wear tests in air at 298 and 493 K. For the high temperature tests, samples were heated from room temperature to 493 K in about 50 minutes. The wear tests were carried out for 500 sliding cycles at a normal load and sliding speed of 1.0 N and 0.03 m/s, respectively. An alumina, Al_2O_3, ball (1,900±40 HV) of 3.18 mm diameter was fixed to the end of the pin and used as the counterface. The COF was recorded at a frequency of 10 s^{-1} during the sliding tests. After the wear tests, the contact surface morphologies were studied using a Wyko NT-1100 optical interferometer, and the width of each wear track was measured at four locations around the track. The volumetric wear losses (V) were measured according to the procedure given in ASTM standard G99 [20] using the following equation:

$$V = 2\pi R \left[r^2 \sin^{-1}\left(\frac{w}{2r}\right) - \left(\frac{w}{4}\right)\sqrt{4r^2 - w^2} \right] \qquad (1)$$

where R and w are the radius and the width of the wear track, and r is the radius of the counterface ball. The wear rates (W) were computed from the slopes of volume loss vs. sliding cycle curves:

$$W = \frac{1}{2\pi R}\left(\frac{\Delta V}{\Delta N}\right) \qquad (2)$$

where ΔV is the volume loss within an interval of ΔN sliding cycles.

The cross-sectional microstructures of the contact surfaces were investigated using FIB and TEM. A Zeiss NVision 40 dual-beam SEM/FIB instrument was employed for the FIB analyses. First, a thin layer of carbon was deposited on the focal area of the contact surface, to protect surface features from beam damage. Next, a narrow trench was milled using a voltage of 30 kV and Ga-ion beam currents ranging from 13 nA to 700 pA to produce a smooth surface perpendicular to the contact surface. To minimize the beam

damage during observation, a lower ion beam current of 10 pA was used to observe the microstructural features of the milled surfaces. It should be noted that although FIB techniques provide new possibilities for studying the microstructures of different materials, the extent of the beam damage to the investigated microstructures must be considered when analyzing the FIB images.

Cross-sectional TEM samples were prepared using the "lift-out" FIB technique shown in Figures 2a-f. Two narrow trenches were ion-milled on both sides of the focal area, protected by a carbon layer, so that a 1 μm thick plate was obtained (Figure 2a). A tungsten needle was then positioned near the plate (Figure 2b), and they were attached by a thin layer of carbon (Figure 2c). The plate was then lifted out (Figures 2d,e) and subsequently milled to a final thickness of about 100 nm, using a low ion beam current of 10 pA (Figure 2f). The TEM investigations were performed using a JEOL 2010 F field emission electron microscope.

3. RESULTS AND DISCUSSION

3.1. Contact Surface Morphologies, Wear Rates and Coefficients of Friction

The contact surface morphologies for all the samples tested at 298 and 493 K are shown in Figures 3a-f. At 298 K, the contact surface of the NC Ni-NP SiC coating exhibited only a few shallow scratches (Figures 3a,c), while notable surface damage and large scratches along the sliding direction were observed on the NC Ni-MP SiC coating (Figure 3b).

At 493 K, severe wear damage was observed on the NC Ni film's contact surface (Figure 3d). The damage was less in the case of the NC Ni-MP SiC coating (Figure 3e).

The lowest surface damage at 493 K, however, was observed on the contact surface of the NC Ni-NP SiC coating (Figure 3f).

The wear rates of the NC Ni film and NC Ni composite coatings after sliding for 500 cycles at 298 and 493 K are plotted in Figure 4. At 298 K, the wear rate of the NC Ni film was $6.17×10^{-6}$ mm^3/m, while the wear rate of the NC Ni-MP SiC coating was almost two orders of magnitude larger ($4.79×10^{-4}$ mm^3/m). The wear rate of the NC Ni-NP SiC coating ($1.31×10^{-5}$ mm^3/m) was in the same range as that of the NC Ni film.

At 493 K, the wear rate of the NC Ni film increased to $8.71×10^{-4}$ mm^3/m, more than two orders of magnitude larger than the wear rate at 298 K. In contrast, the effect of temperature on the wear rates for the composite coatings was smaller (i.e., W(NC Ni-MP SiC) = $5.74×10^{-4}$ mm^3/m and W(NC Ni-NP SiC) = $1.60×10^{-4}$ mm^3/m). At 493 K, reinforcing NC Ni with MP SiC reduced its wear rate by 34%, and reinforcing NC Ni with NP SiC reduced the wear rate by 82%.

Variations in the COF with the sliding cycles for the NC Ni and its composites at 298 and 493 K are shown in Figures 5a-f. At 298 K, the COF curves of the NC Ni film and the NC Ni-NP SiC coating had lower and smoother (less fluctuation) trends compared to that of the NC Ni-MP SiC coating. This difference was more evident at the beginning of the sliding tests. At 493 K, the COF curves of the coatings had a similar beginning, and a sudden drop was noted in the trends of all three curves. However, in the case of the NC Ni-NP SiC coating, this drop occurred at lower sliding cycles (around 250 cycles) and was more pronounced. This sample had a lower and smoother COF curve thereafter.

The average steady-state COFs (average of the COF values measured after sliding for 400-500 cycles) of all the samples are plotted and compared in Figure 6. At 298 K, the

steady-state COFs of both the NC Ni (0.33±0.03) and NC Ni-NP SiC coatings (0.35±0.04) were notably lower than that of the NC Ni-MP SiC coating (0.47±0.09). At 493 K, the steady-state COF of the NC Ni-NP SiC coating (0.42±0.02) was significantly lower than those of the NC Ni (0.55±0.05) and the NC Ni-MP SiC coating (0.60±0.08).

3.2. Microstructural Evolution during Sliding Wear

Cross-sectional FIB images of the coatings after the wear tests are presented in Figures 7a-f. At 298 K, a deformed layer with a thickness of 206±16 nm could be seen on top of the NC Ni's worn surface in the section shown in Figure 7a. The NC Ni-NP SiC coating revealed the same type of microstructure, with a 288±23 nm thick deformed layer on top (Figure 7c). The deformed layer on the surface of the NC Ni-MP SiC coating, however, was thicker (639±38 nm), and a tribolayer had formed on top of the deformed layer (Figure 7b). Small fragments of NC Ni, as well as SiC particles were embedded inside this tribolayer, indicating that it formed as a result of the agglomeration and compaction of a relatively large amount of debris particles, generated by the abrasive effect of the large SiC particles that detached from the coating during the sliding wear test. This abrasive wear was the source of the NC Ni-MP SiC coating's high wear rate (Figure 4).

At 493 K, the deformed layer of the NC Ni film had a thickness of 1,236±74 nm (Figure 7d), 5 times thicker than it was at 298 K. This correlates with the sharp increase in the wear rate of the NC Ni coating when the wear test temperature was increased from 298 K to 493 K (Figure 4), possibly caused by a transition in the deformation mechanism from grain boundary diffusion to grain boundary sliding [16]. The effect that temperature

had on the microstructures of the composite coatings was different. At 498 K, similar to the tests performed at room temperature, a tribolayer formed on top of the deformed layer in the NC Ni-MP SiC coating (Figure 7e). The cross-sectional FIB image of the NC Ni-NP SiC coating worn at 493 K is seen in Figure 7f. Incorporating NP SiC in NC Ni could significantly reduce the microstructural damage (i.e., 46% reduction in the thickness of the deformed layer to 671±40 nm), leading to an 82% reduction in the wear rate compared to the unreinforced NC Ni at the same temperature (Figure 4).

Bright-field and dark-field cross-sectional TEM images of the deformed layer in the NC Ni film and the NC Ni-NP SiC coating are shown in Figures 8a-d. The grains were elongated and moved towards the sliding direction in the subsurface region of the unreinforced NC Ni coating (Figures 8a,b), a phenomenon that was less pronounced in the case of the NC Ni-NP SiC coating (Figures 8c,d). A high resolution TEM image of the subsurface microstructure in the unreinforced NC Ni tested at 493 K is presented in Figure 9 that shows new recrystallized grains formed at the grain boundaries during the high temperature wear test. Also, grain boundary sliding is known to be the preferred deformation mechanism in this material at high temperatures [16]. The recrystallization of new grains, as well as the grain boundary sliding deformation mechanism could possibly be hindered by the nanoparticles in the NC Ni-NP SiC composite coating during the high temperature sliding wear tests, resulting in a significant reduction (i.e., 82% as seen in Figure 4) in this coating's wear rate, compared to the unreinforced NC Ni film. More work on the nanoscale interactions between nanoparticles and NC Ni grains is needed to shed light on the details of the mechanisms involved in the deformation of this material at elevated temperatures.

4. CONCLUSIONS

1. Increasing the sliding test temperature from 298 K to 493 K resulted in an increase in wear rate of more than two orders of magnitude (from 6.17×10^{-6} mm^3/m to 8.71×10^{-4} mm^3/m) and a 67% increase in the COF of the NC Ni coating, possibly caused by a transition in the deformation mechanism from grain boundary diffusion to grain boundary sliding.

2. Incorporating SiC particles in the NC Ni did not result in any significant increase in the hardness of this material. However, the SiC particles did play substantial roles in the tribological performances of the coatings.

3. At 298 K, the NC Ni-MP SiC coating had a higher wear rate and COF compared to both the NC Ni film and the NC Ni-NP SiC coating, due to the abrasive wear caused by the large SiC particles that detached from the coating's surface during the wear test.

4. Reinforcing NC Ni with SiC particles improved its high-temperature wear resistance. It was suggested that the recrystallization of new grains, as well as the grain boundary sliding deformation mechanism could possibly be hindered by the nanoparticles in the NC Ni-NP SiC composite coating, resulting in 82% and 24% reductions in the coating's high-temperature wear rate and COF, respectively.

REFERENCES

[1]   K.S. Siow, A.A.O. Tay, P. Oruganti, Mater. Sci. Tech. 20 (2004) 285.

[2]   R. Schwaiger, B. Moser, M. Dao, N. Chollacoop, S. Suresh, Acta Mater. 51 (2003) 5159.

[3]   K.S. Kumar, S. Suresh, M.F. Chisholm, J.A. Horton, P. Wang, Acta Mater. 51 (2003) 387.

[4]   K.S. Kumar, H. Van Swygenhoven, S. Suresh, Acta Mater. 51 (2003) 5743.

[5]   F. Dalla Torre, H. Van Swygenhoven, M. Victoria, Acta Mater. 50 (2002) 3957.

[6]   F. Ebrahimi, G.R. Bourne, M.S. Kelly, T.E. Matthews, Nanostruct. Mater. 11 (1999) 343.

[7]   C.A. Schuh, T.G. Nieh, T. Yamasaki, Scripta Mater. 46 (2002) 735.

[8]   D.H. Jeong, F. Gonzalez, G. Palumbo, K.T. Aust, U. Erb, Scripta Mater. 44 (2001) 493.

[9]   M. Shafiei, A.T. Alpas, Metall. Mater. Trans. A38 (2007) 1621.

[10] M. Shafiei, A.T. Alpas, Wear 265 (2008) 429.

[11] U. Klement, U. Erb, K.T. Aust, Nanostruct. Mater. 6 (1995) 581.

[12] U. Klement, U. Erb, A.M. El-Sherik, K.T. Aust, Mater. Sci. Eng. A203 (1995) 177.

[13] Y.M. Wang, S. Cheng, Q.M. Wei, E. Ma, T.G. Nieh, A. Hamza, Scripta Mater. 51 (2004) 1023.

[14] C. Xiao, R.A. Mirshams, S.H. Whang, W.M. Yin, Mater. Sci. Eng. A301 (2001) 35.

[15] F. Dalla Torre, H. Van Swygenhoven, R. Schaublin, P. Spatig, M. Victoria, Scripta Mater. 53 (2005) 23.

[16] W.M. Yin, S.H. Whang, R. Mirshams, C.H. Xiao, Mater. Sci. Eng. A301 (2001) 18.

[17] H.K. Lee, H.Y. Lee, J.M. Jeon, Surf. Coat. Tech. 201 (2007) 4711.

[18] J.H. Adair, T. Li, T. Kido, K. Havey, J. Moon, J. Mecholsky, A. Morrone, D.R. Talham, M.H. Ludwig, L. Wang, Mater. Sci. Eng. R23 (1998) 139.

[19] A. Hasnaoui, H. Van Swygenhoven, P.M. Derlet, Acta Mater. 50 (2002) 3927.

[20] Friction and Wear Testing, ASM, Materials Park, OH, 1997, pp. 124-128.
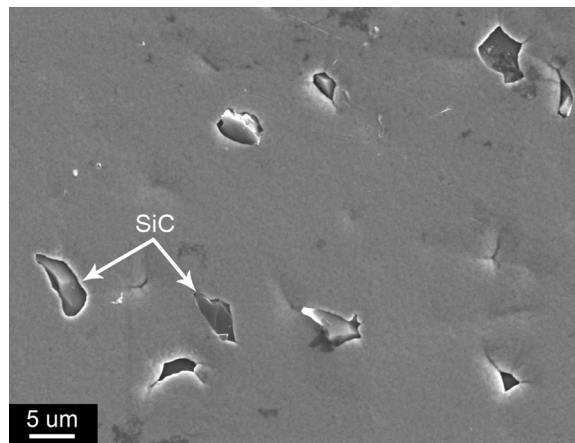
(a)
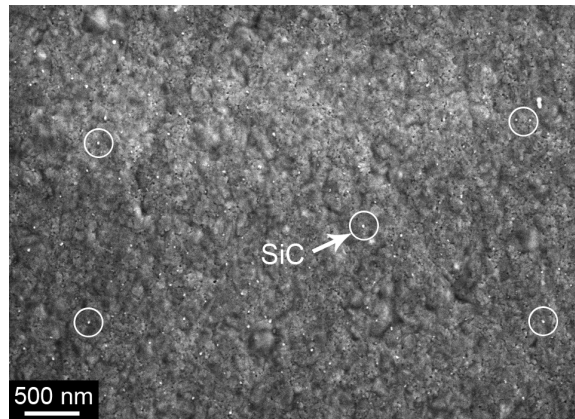
(b)

Figure 1. Secondary electron SEM surface images of (a) the NC Ni-MP SiC coating, and (b) the NC Ni-NP SiC coating.
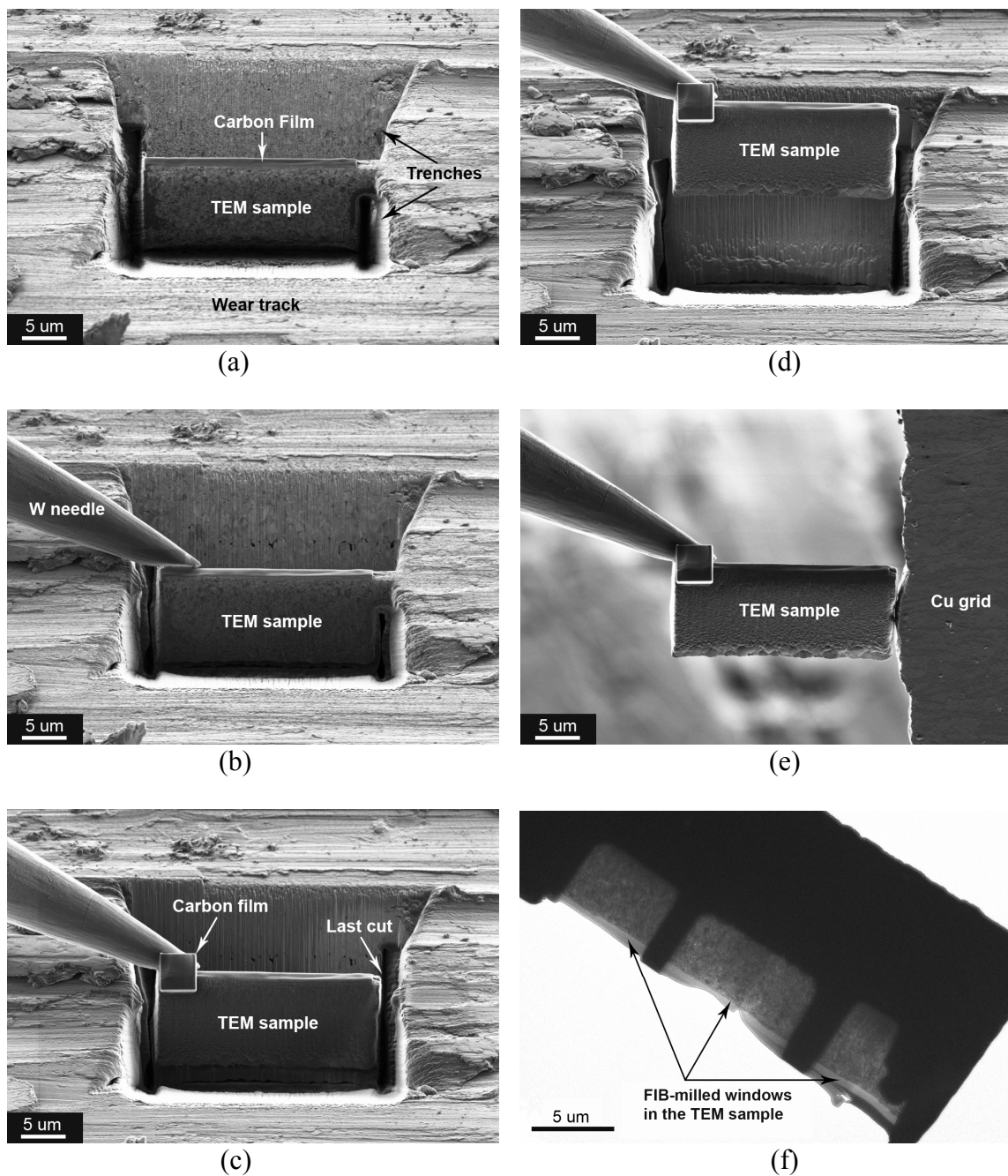
Figure 2. The main steps in preparing TEM samples using the "lift-out" FIB technique. (a) Two narrow trenches were ion-milled on both sides of the area of interest, protected by a carbon layer, to obtain a 1 μm thick plate. (b) A tungsten needle was positioned near the plate. (c) A thin layer of carbon was deposited on the interface of the plate and the needle, to attach them. (d,e) The plate was then lifted out, and (f) milled to a final thickness of about 100 nm using a low ion beam current of 10 pA.
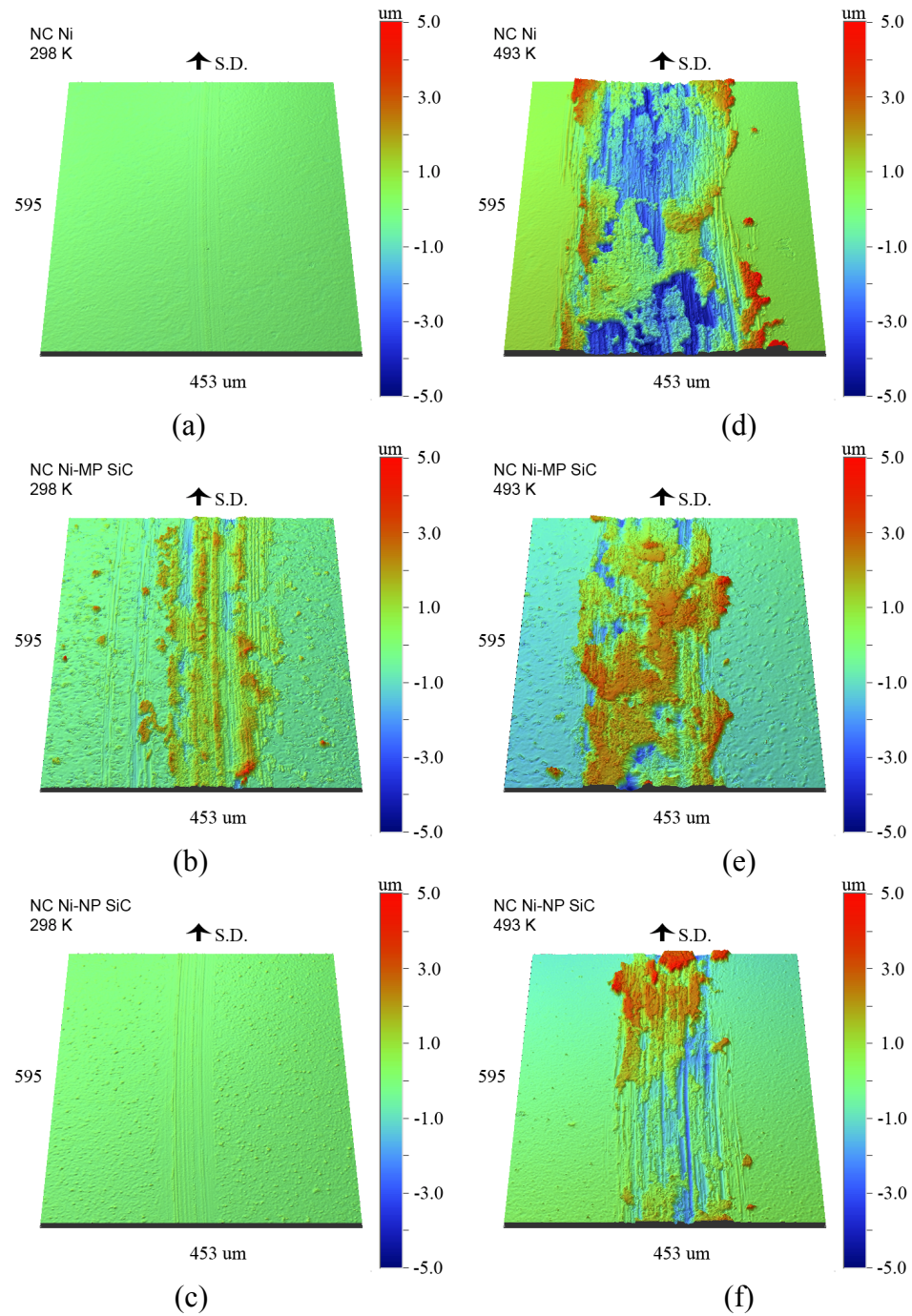
Figure 3. (a-c) Contact surface morphologies formed after sliding for 500 cycles at 298 K on: (a) the NC Ni film, (b) the NC Ni-MP SiC coating, and (c) the NC Ni-NP SiC coating. (d-f) The contact surface morphologies formed after sliding for 500 cycles at 493 K on: (d) the NC Ni film, (e) the NC Ni-MP SiC coating, and (f) the NC Ni-NP SiC coating.
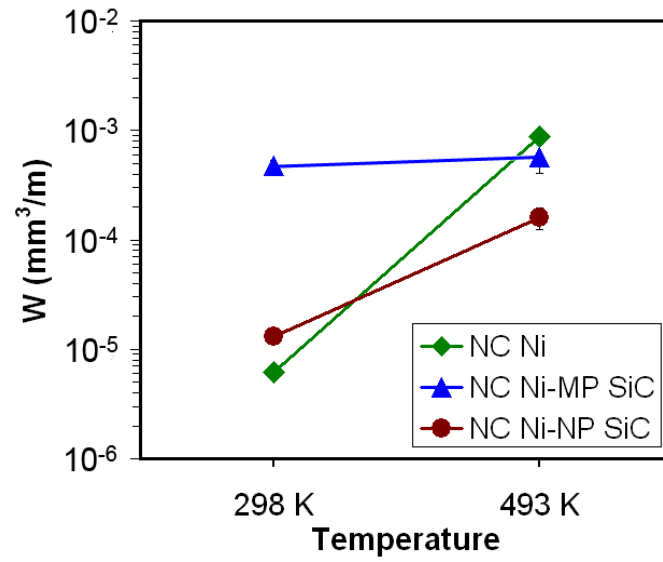
Figure 4. The wear rates of the unreinforced NC Ni and the NC Ni composite coatings measured after sliding for 500 cycles at 298 and 493 K.
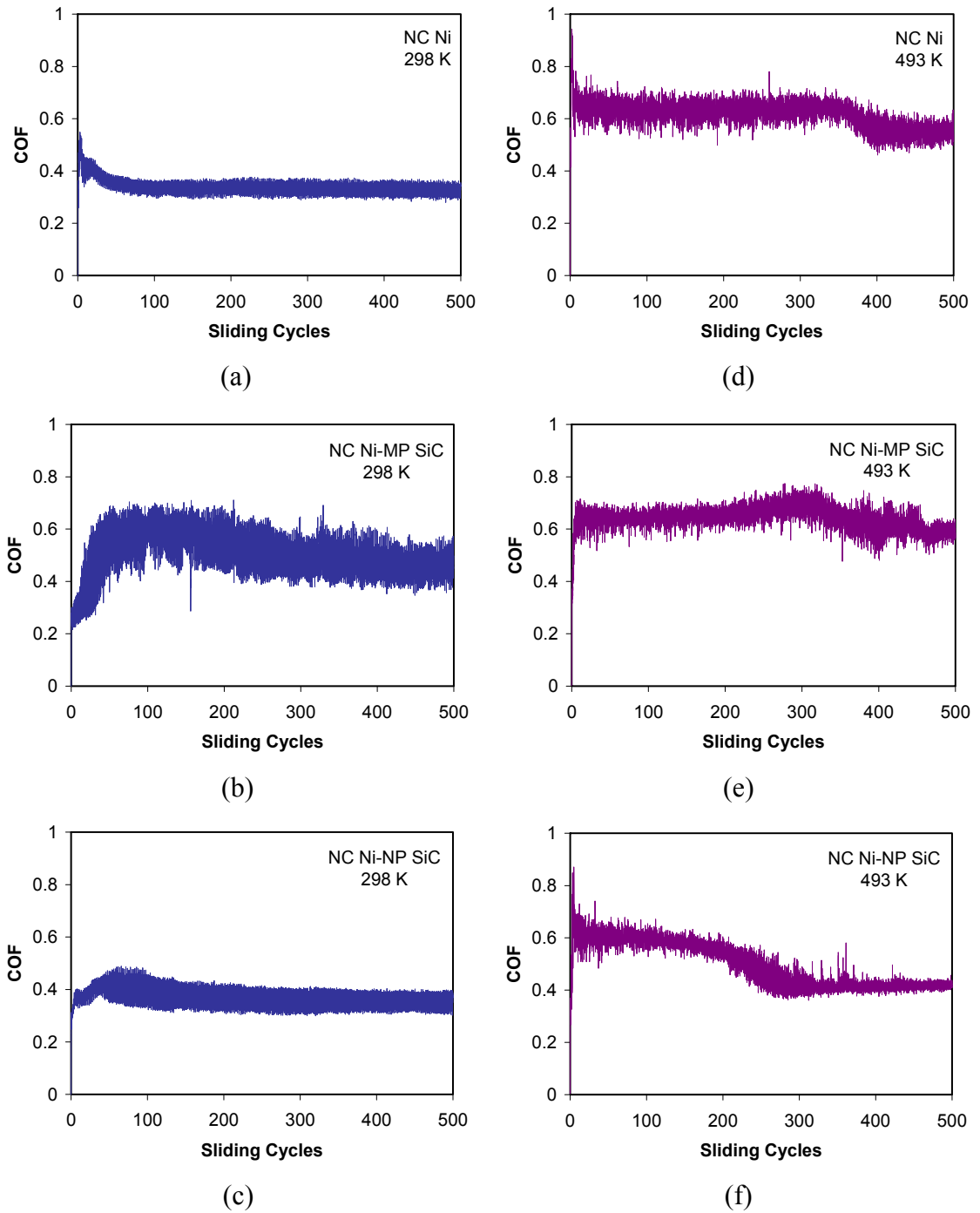
Figure 5. (a-c) Variations in COFs at 298 K for: (a) the NC Ni film, (b) the NC Ni-MP SiC coating, and (c) the NC Ni-NP SiC coating. (d-f) Variations in COFs at 493 K for: (d) the NC Ni film, (e) the NC Ni-MP SiC coating, and (f) the NC Ni-NP SiC coating.
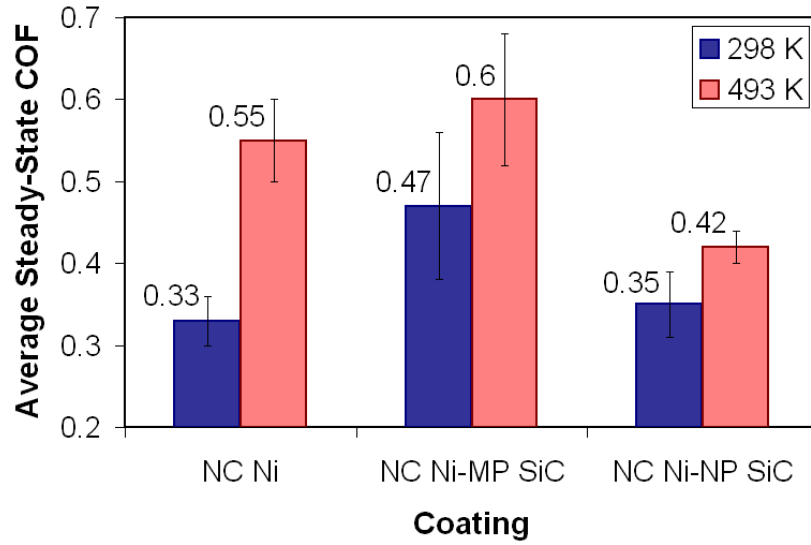
Figure 6. Average steady-state COFs for the NC Ni and NC Ni composite coatings after sliding for 500 cycles at 298 and 493 K.

(a)

(b)

114

Carbon Film

D.L.

1 um   Mag= 10KX   FIB Probe= 30KV:10pA   S.D. →

(c)

Carbon Film

D.L.

1 um   Mag= 10KX   FIB Probe= 30KV:10pA   S.D. →
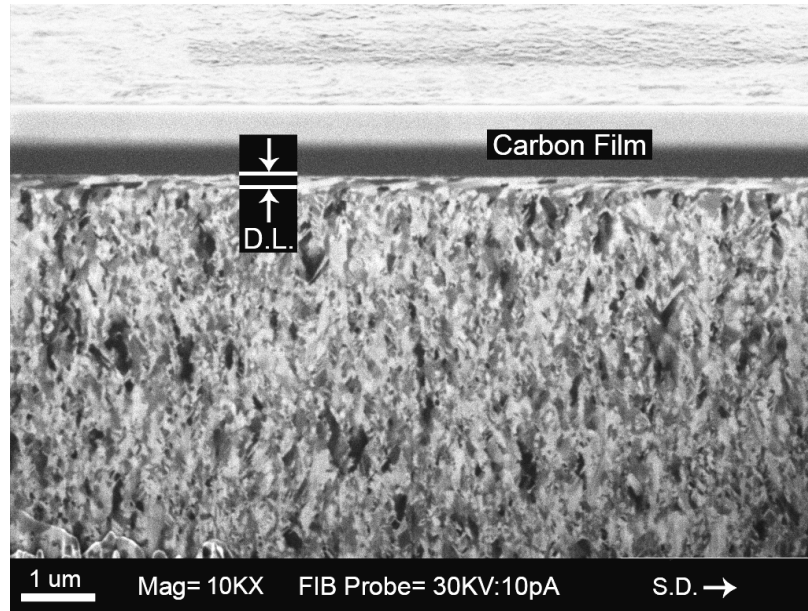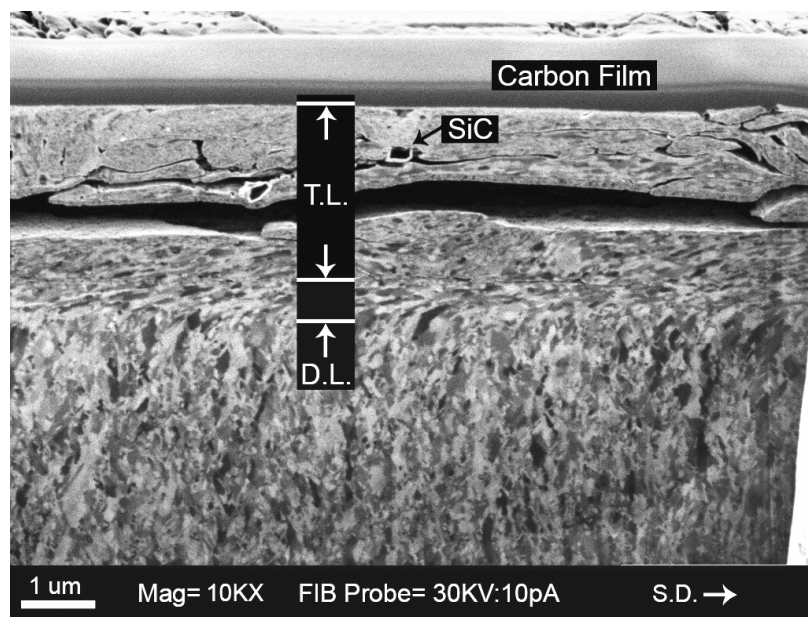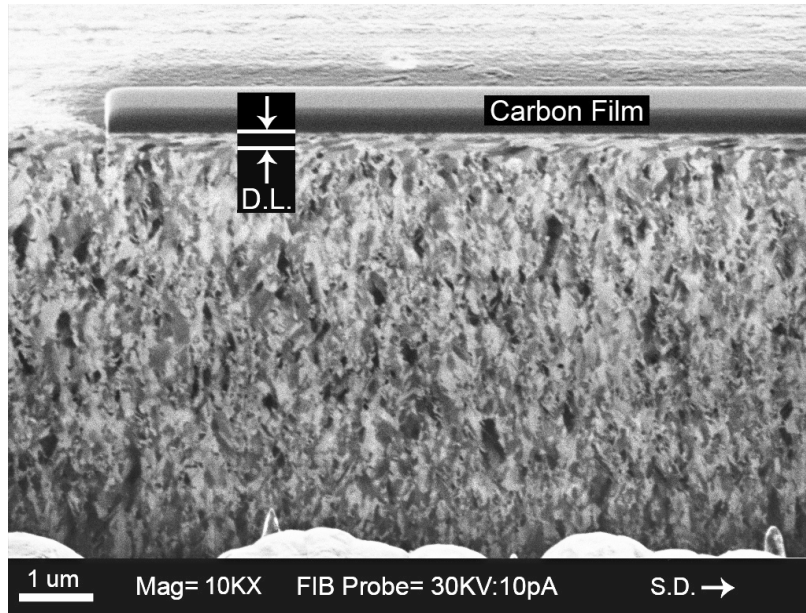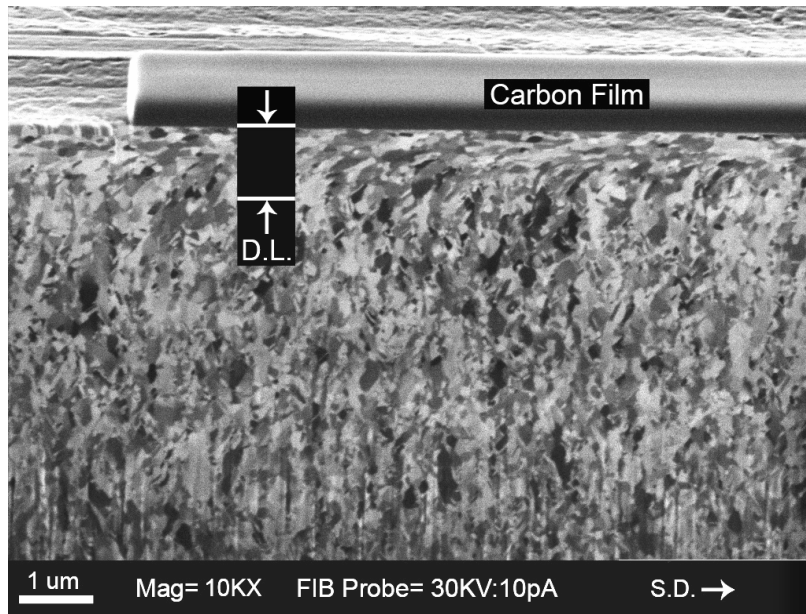
(d)
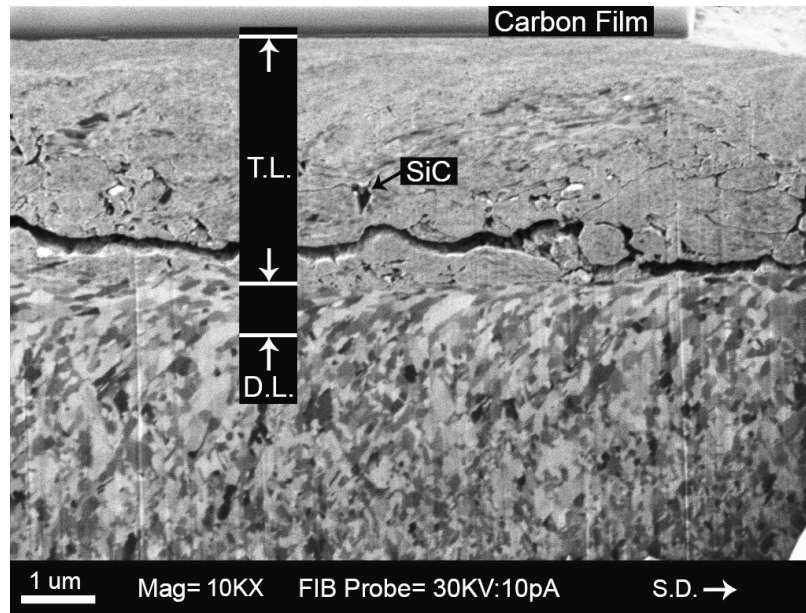
(e)
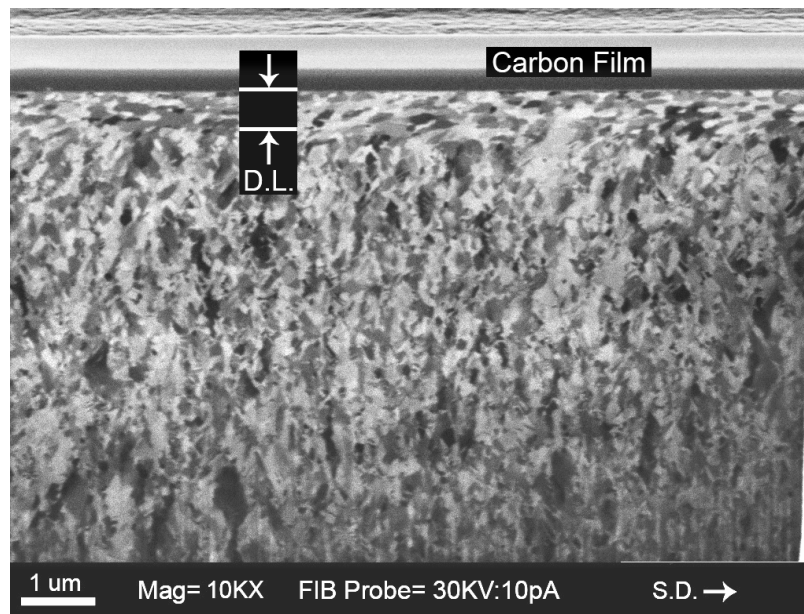
(f)

Figure 7. (a-c) Cross-sectional FIB images of the wear tracks formed after sliding for 500 cycles at 298 K on: (a) the NC Ni film, (b) the NC Ni-MP SiC coating, and (c) the NC Ni-NP SiC coating. (d-f) Cross-sectional FIB images of the wear tracks formed after sliding for 500 cycles at 493 K on: (d) the NC Ni film, (e) the NC Ni-MP SiC coating, and (f) the NC Ni-NP SiC coating. S.D.: sliding direction; D.L.: deformed layer; T.L.: tribolayer.

(a)

(b)

117
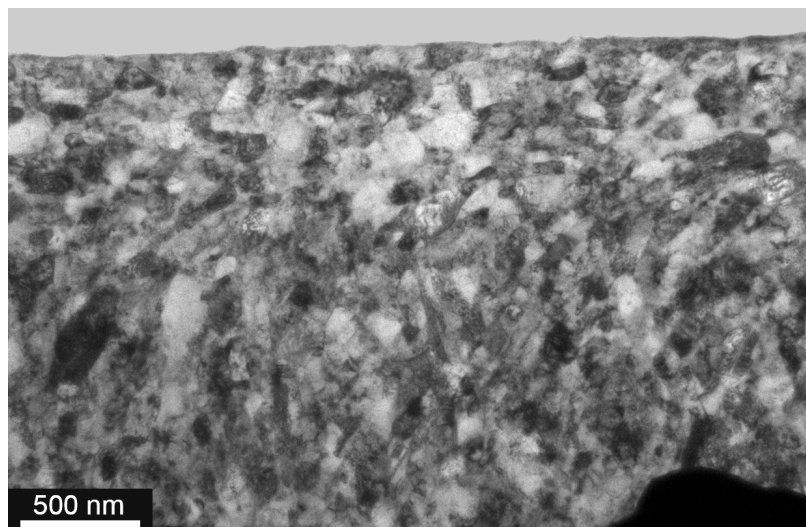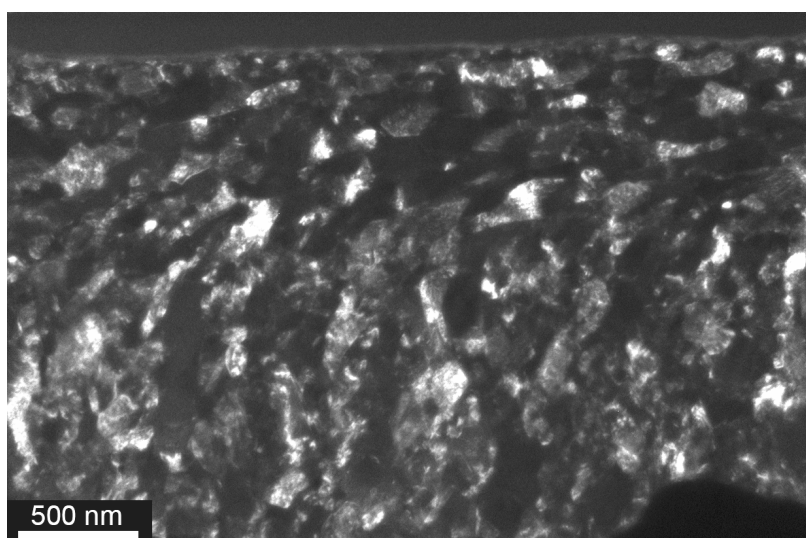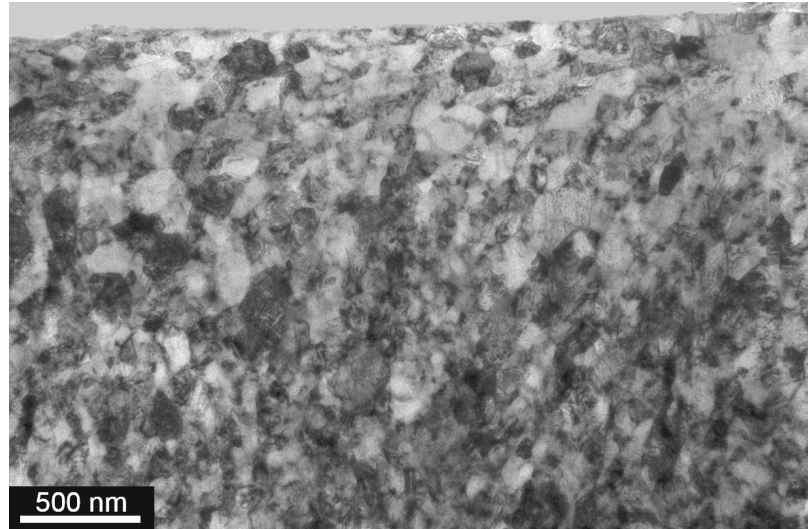
(c)
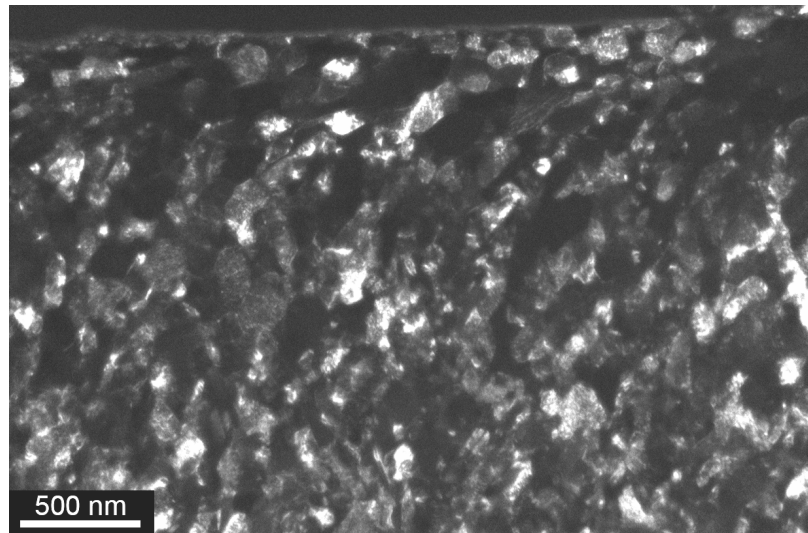
(d)

Figure 8. Bright-field and dark-field cross-sectional TEM images of the deformed layers formed after sliding for 500 cycles at 493 K on: (a,b) the unreinforced NC Ni coating, and (c,d) the NC Ni-NP SiC coating.
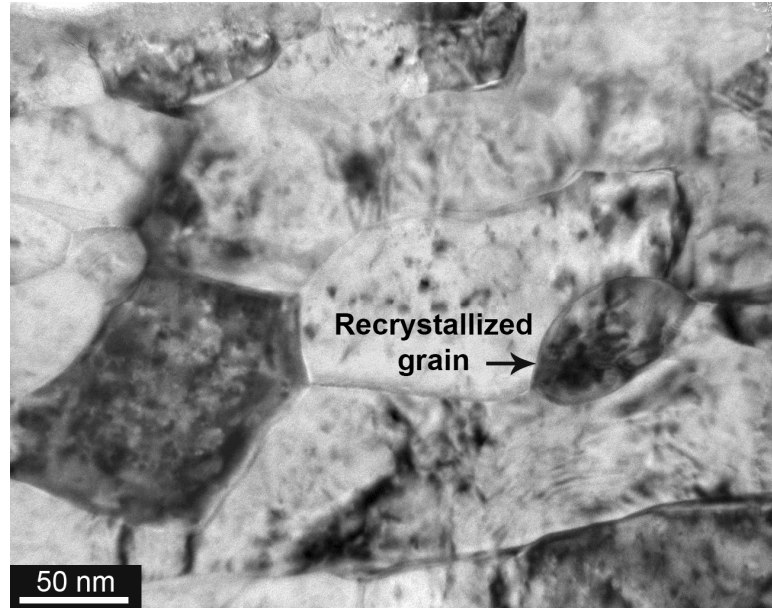
Figure 9. A high resolution TEM image of the subsurface microstructure in the unreinforced NC Ni tested at 493 K shows new grains recrystallized at grain boundaries during the high temperature wear test.

CHAPTER 5

FRICTION AND WEAR BEHAVIOUR OF NANOCRYSTALLINE COBALT

1. INTRODUCTION

New tribological surfaces with improved wear resistance can be designed employing nanocrystalline (NC) materials that exhibit higher strength and hardness compared to their microcrystalline (MC) counterparts. Electrolytic deposition allows production of NC metals with narrowly controlled grain size distribution in the range of 10-100 nm [1], and with low defect density [2]. Mechanical properties [3-6] and tribological behaviour [7-9] of electrodeposited NC Ni have been studied. Shafiei and Alpas [9] showed that an NC Ni with a grain size of 15 nm had 18% lower peak COF, almost two orders of magnitude smaller initial wear rate and 77% smaller steady-state wear rate compared to Ni with 20 μm grain size. There are a few reports on the mechanical properties of electrodeposited NC Co in the open literature [10, 11]. However, the tribological behaviour of NC Co has not received much attention. There is a need for further experimental work to characterize micromechanisms of wear in NC Co, and rationalize microscopic processes leading to surface damage. In this work, a pin-on-disc tribometer was employed to study friction and wear behaviour of NC Co in comparison to MC Co.

2. EXPERIMENTAL PROCEDURES

Electrodeposited NC Co sheets with 99.9% purity and grain size of 20±5 nm and annealed Co foils with grain size of 16±3 μm and the same purity were polished to 1 μm using a diamond suspension. Using an indentation load of 100 gf, the Vickers microhardnesses of the MC Co and NC Co were measured as 299±8 HV and 503±13 HV, respectively. A CSM pin-on-disc tribometer was used to measure the variations of coefficient of friction (COF) with sliding cycles under unlubricated sliding conditions in ambient air with 35% relative humidity. The tests were conducted under a normal load of 2 N at a sliding speed of 0.1 m/s. An Al_2O_3, ball (HV = 1,900±40) with 3.18 mm diameter was used as the counterface material. After the tests, the morphologies of the wear tracks were investigated by optical surface profilometry, optical microscopy, scanning electron microscopy (SEM) and energy dispersive spectroscopy (EDS). Volume losses were measured according to the procedure given in ASTM standard G99 [12]. Wear rates were calculated from the slopes of the volume loss vs. sliding cycles curves.

3. RESULTS AND DISCUSSION

3.1. Friction, Volume Loss and Wear Rate

Variations of COF with sliding cycles for the MC Co and NC Co are shown in Figure 1. The NC Co showed a COF peak of 0.57 at 300 cycles. A steady-state COF of 0.44 was observed in this sample after 600 cycles. In contrast, the COF of the MC Co increased without showing a peak, and after 500 cycles, a steady-state COF of 0.51 was reached. Although the initial COF of the NC Co was higher than that of the MC Co, its steady-state COF was lower.

The variations in the volume losses of the MC Co and NC Co with the sliding cycles are shown in Figure 2a. The volume losses of the MC Co were lower than those of the NC Co at all the sliding cycles. Figure 2b presents the wear rates of the samples. For both MC and NC Co, wear rates decreased rapidly as the sliding wear progressed. Although the wear rate of the NC Co was initially higher than that of the MC Co, the steady-state wear of the NC Co was milder than that of the MC Co. This behaviour correlates with the higher initial COF and the lower steady-state COF of the NC Co (Figure 1).

3.2. Wear Mechanisms

The morphologies of the wear tracks formed on the surfaces of the MC Co and NC Co after 1000 sliding cycles are shown in Figure 3 (optical surface profiles) and Figure 4 (optical micrographs). Worn surfaces of both MC and NC Co were characterized by continuous surface scratches. Although the hardness of the NC Co was higher than that of the MC Co, the surface damage to NC Co was more pronounced, i.e. the average width and depth of the NC Co's wear track after 1000 sliding cycles were larger than those of the MC Co's (Figures 3a,b). Large amounts of fine debris particles generated during the wear tests were seen scattered around the wear tracks (Figures 4a,b). Some debris particles were agglomerated and compacted by the counterface, and formed tribolayers on top of the contact surfaces of both MC and NC Co. However, the tribolayers covered larger areas on the NC Co's wear track.

Figure 5 shows the SEM micrographs and typical EDS spectra of the tribolayers formed on top of the wear tracks. In this study, EDS was used as a semi-quantitative method to compare oxygen content of the tribolayers. Also, EDS measurements were

performed in multiple locations along each wear track. The typical EDS spectra presented in Figure 5 show that the NC Co's tribolayer contained higher amount of oxygen compared to the MC Co's tribolayer.

The larger tribolayer area coverage in the NC Co and the larger amount of oxygen detected in this tribolayer, compared to the MC Co's tribolayer, are the results of the higher tendency of NC Co for oxidation. As nanocrystalline materials have a high density of grain boundaries which act as preferential nucleation sites for oxides [13] and the grain boundaries can provide faster diffusion paths for oxygen, they are susceptible to surface oxidation during sliding wear [9]. Higher rate of oxidational wear in NC Co resulted in higher initial surface damage in this material compared to the MC Co. Once the tribolayer was formed on top of the contact surfaces, the steady-state wear replaced the initial wear, reducing COF and wear rate in the NC Co (Figures 1 and 2b) as the oxide-rich tribolayers are harder than the original surfaces [9].

4. CONCLUSIONS

Although the hardness of the NC Co was higher than that of the MC Co, initial COF and wear rate were higher in this material due to the atmospheric effects. In order to observe the benefits of the high hardness afforded by NC structure, tests should be done in inert atmosphere.

REFERENCES

[1]   A.P. Zhilyaev, J. Gubicza, G. Nurislamova, A. Revesz, S. Surinach, M.D. Baro, T. Ungar, Phys. Stat. Sol. A198 (2003) 263.

[2]   L.L. Shaw, JOM 52 (2000) 41.

[3]   K.S. Kumar, H. Van Swygenhoven, S. Suresh, Acta Mater. 51 (2003) 5743.

[4]   F. Ebrahimi, G.R. Bourne, M.S. Kelly, T.E. Matthews, Nanostruct. Mater. 11 (1999) 343.

[5]   F. Dalla Torre, H. Van Swygenhoven, M. Victoria, Acta Mater. 50 (2002) 3957.

[6]   R. Schwaiger, B. Moser, M. Dao, N. Chollacoop, S. Suresh, Acta Mater. 51 (2003) 5159.

[7]   C.A. Schuh, T.G. Nieh, T. Yamasaki, Scripta Mater. 46 (2002) 735.

[8]   D.H. Jeong, F. Gonzalez, G. Palumbo, K.T. Aust, U. Erb, Scripta Mater. 44 (2001) 493.

[9]   M. Shafiei, A.T. Alpas, Metall. Mater. Trans. A38 (2007) 1621.

[10] A.A. Karimpoor, U. Erb, K.T. Aust, G. Palumbo, Scripta Mater. 49 (2003) 651.

[11] A.A. Karimpoor, U. Erb, Phys. Stat. Sol. A203 (2006) 1265.

[12] Friction and wear testing, ASM, Materials Park, OH, 1997, pp. 124-128.

[13] S.H. Kim, U. Erb, K.T. Aust, F. Gonzalez, G. Palumbo, Plat. Surf. Finish. May (2004) 68.

FIGURES
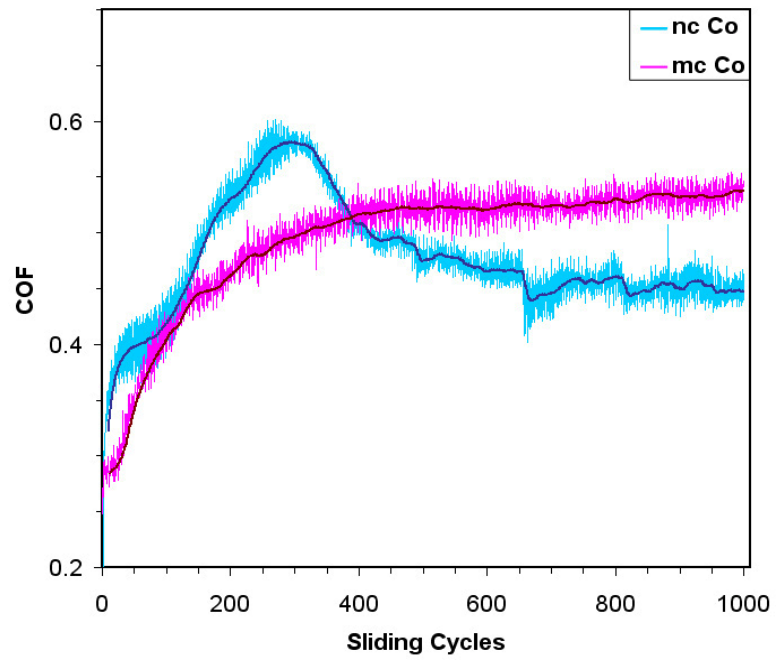
Figure 1. Variations of COF with sliding cycles in the MC Co and NC Co.
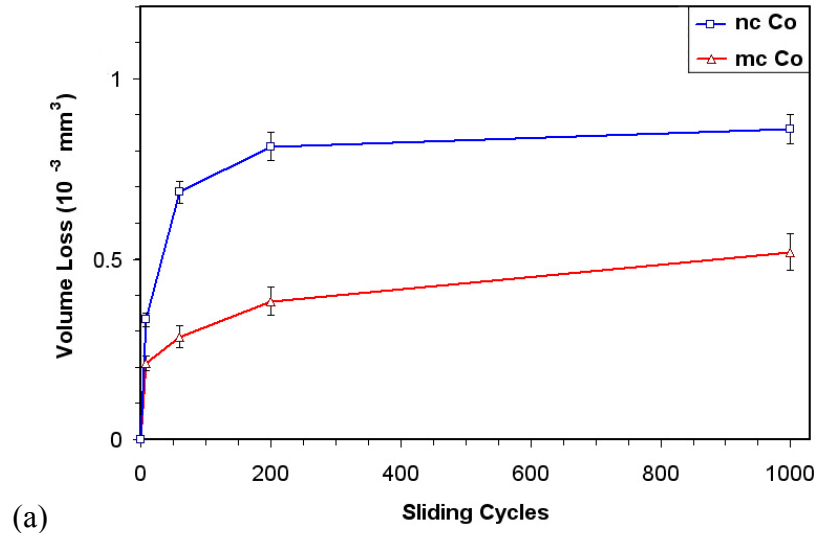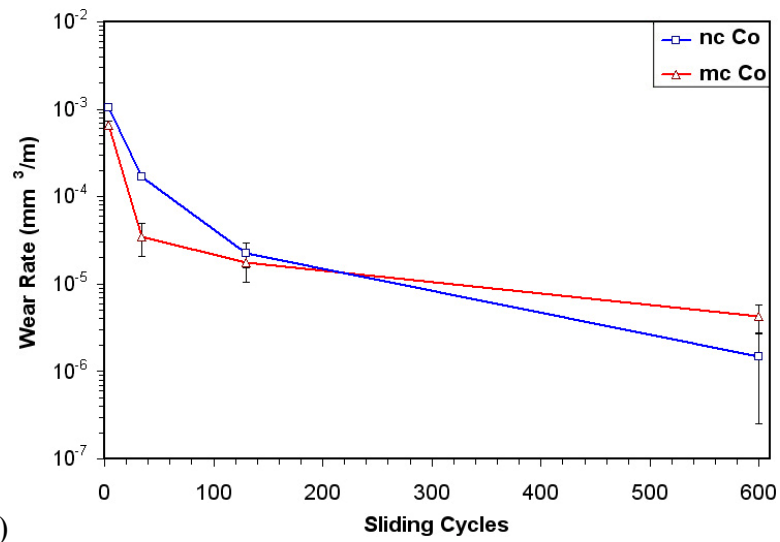
Figure 2. (a) Variation of volume loss with sliding cycles for the MC Co and NC Co. (b) Variations of wear rate with sliding cycles for the MC Co and NC Co.
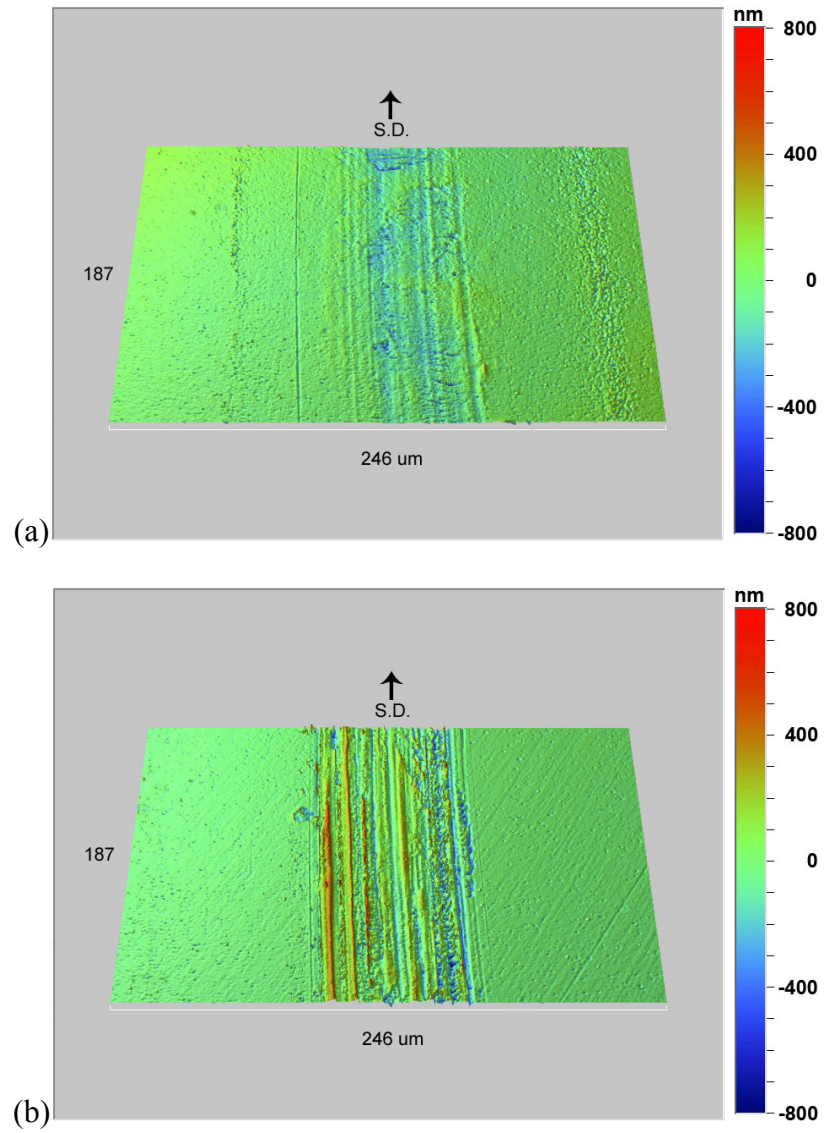
Figure 3. Optical surface profiles of the wear tracks after 1000 sliding cycles on: (a) MC Co, and (b) NC Co.
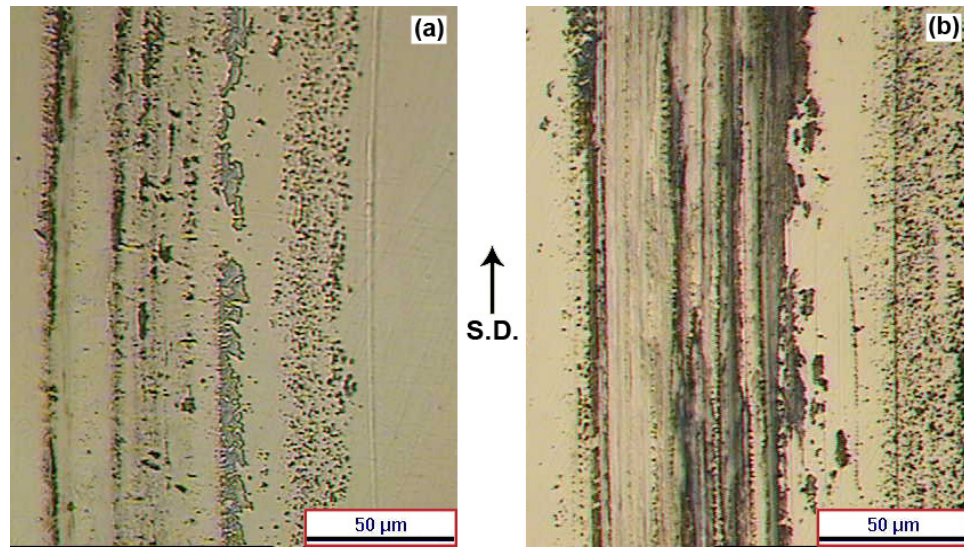
Figure 4. Optical micrographs of the wear tracks after 1000 sliding cycles on: (a) MC Co, and (b) NC Co.
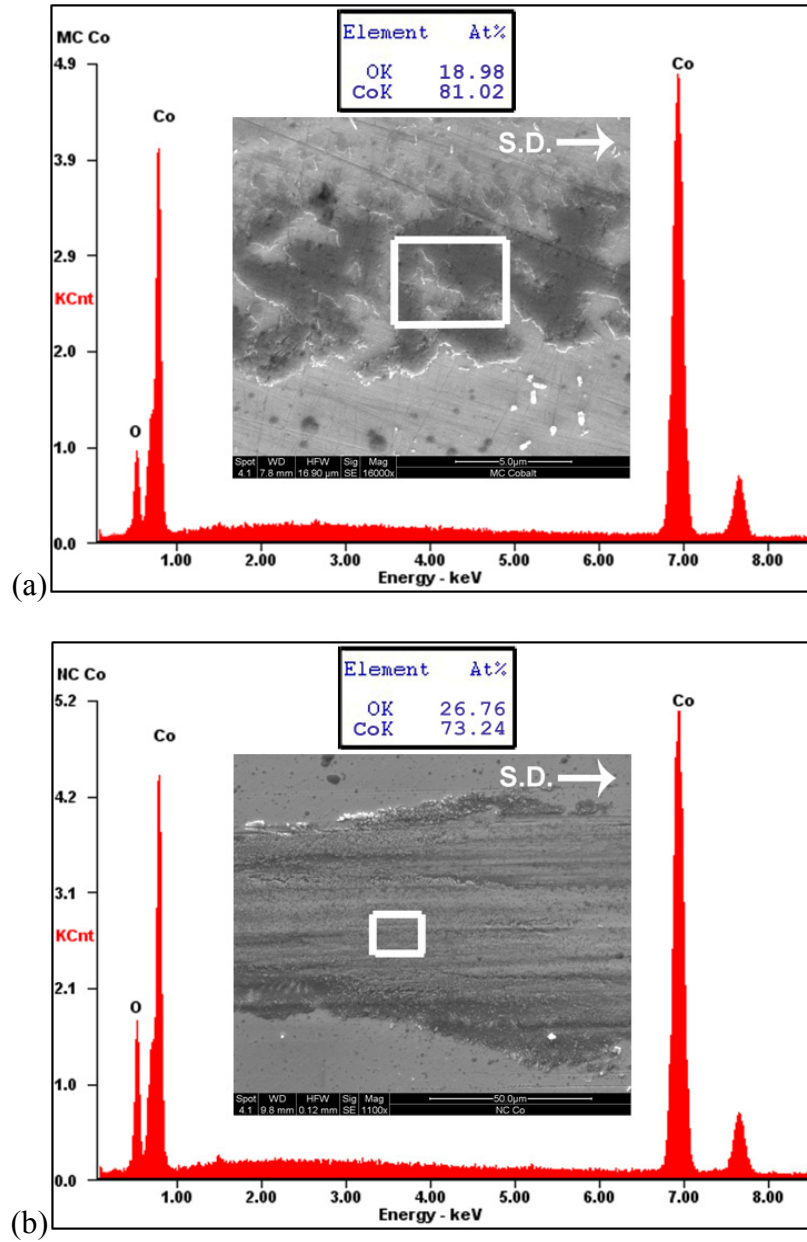
Figure 5. SEM micrographs and typical EDS spectra of the tribolayers formed on top of the wear tracks after 1000 sliding cycles for: (a) MC Co, and (b) NC Co.

CHAPTER 6

FABRICATION OF BIOTEXTURED NANOCRYSTALLINE NICKEL FILMS FOR THE REDUCTION AND CONTROL OF FRICTION

1. INTRODUCTION

Many sectors of industry display a growing need for the development of new methods for controlling frictional forces at submicron and nanometre scales. Reducing and/or controlling friction between moving parts in traditional industries, like automotive manufacturing, helps conserve energy and lower environmental pollutions. On the other hand, when the surface-to-volume ratio is large and applied loads are extremely small, the application of conventional lubrication techniques is not always effective in controlling the friction [1,2]. For example, the frictional properties of the moving components of micro-electro-mechanical systems (MEMS) are dominantly controlled by their surface texture and surface chemistry [1]. In recent years, several techniques have been developed to reduce frictional forces by topographically structuring contact surfaces. For instance, soft lithography techniques have been used to reduce friction by decreasing the real area of contact [3-5], and laser texturing has been employed to create microgrooves and microdimples that act as lubricant reservoirs [6-8].

The natural world offers multiple examples of surfaces that are optimized to control friction through a combination of surface texture, orientation and flexibility [9]. Various kinds of barbs and hooks found in biological systems [9], the attachment pads of the

130

cricket [9], the gripping feet of the gecko [10,11], and the textured snake skin [12] suggest that nature has adapted the most effective ways of controlling friction. Hence, enhancing frictional properties by fabricating engineering surfaces that mimic biotextures will prove a promising technological trend in future.

This chapter details the development of a simple replication technique that allows specific biotextures to be fabricated in the form of self-sustaining metallic films. For this purpose, two different biotextures, lotus leaf and boa's skin, were replicated to create metallic surface features that reduce and control frictional forces. One important aspect of the method presented here is that the metallic replicas were made of nanocrystalline (NC) Ni with a high hardness, a property that improved load-carrying ability of the surfaces.

2. EXPERIMENTAL PROCEDURES

Figure 1 illustrates the main steps involved in the technique developed to fabricate hard NC Ni replicas of biotextures, e.g. surface textures of lotus leaf and boa's skin. In the first step, the surface texture of the selected biological sample was replicated on a cellulose acetate film to obtain a negative impression of the texture (Figure 1a). In the next step, a thin layer of gold with a thickness of 90±30 nm was sputtered on the acetate film to provide a conductive surface (Figure 1b). The acetate film was then placed in an electrolytic cell to deposit an NC Ni layer on top of this film (Figure 1c). The electrodeposition parameters are listed in Table 1. The electrolyte was composed of 300 g/l $NiSO_4$, 45.0 g/l $NiCl_2$, 45.0 g/l HBO_3, 5.00 g/l saccharin and 0.25 g/l SNAP. Finally, the acetate film was dissolved in acetone to obtain a self-sustaining NC Ni film with a surface texture similar to the original biotexture (Figure 1d).

An NC Ni film was also deposited on a flat Cu foil using similar electrodeposition chemistry and parameters to compare frictional properties. The Cu substrate was dissolved in a solution containing 250 g/l CrO_3 and 15.0 ml/l sulphuric acid to obtain a flat NC Ni film with a thickness of 77±4 μm and a roughness of 11±2 nm.

The surface textures of the samples were studied using a scanning electron microscope (SEM), an optical interferometric surface profilometer and an optical digital microscope. A transmission electron microscope (TEM) was employed to study the microstructure of the NC Ni films. The grain size of the films was measured using the linear intercept method on several TEM micrographs. The Vickers microhardness of the NC Ni films was determined as the average of ten measurements using a load of 0.25 N.

The coefficients of friction (COF) of the NC Ni replica of the lotus leaf and the flat NC Ni film were measured using a pin-on-disc tribometer operating under a load of 1.0 N at a sliding speed of 0.01 m/s. An alumina (Al_2O_3) ball with a diameter of 3.18 mm and a hardness of 18.64±0.39 GPa was fixed at the end of a pin and used as the counterface.

To measure the COFs of the NC Ni replica of the boa's skin, an instrumented microscratch tester with a Rockwell-type diamond indenter tip was used. The tests were conducted under a normal load of 0.5 N at a sliding speed of 4.0 μm/s. All the friction tests were conducted in ambient air with 35% relative humidity.

3. RESULTS AND DISCUSSION

3.1. Nanocrystalline Nickel Replica of the Lotus Leaf: Reducing the Friction

The surface texture of the lotus leaf consists of microscopic protuberances covered by a needle-like nanostructure with a waxy surface composition. This multilevel surface

roughness is known as the source of the lotus leaf's superhydrophobic property [13-15]. However, this property was not of interest in this study. Instead, interest fell on investigating whether the reduction in real area of contact produced as a result of surface protuberances might reduce the COF. Figure 2a shows an SEM micrograph of the surface texture of the as-received lotus leaf. A negative impression of the lotus leaf's surface texture on the acetate film is seen in Figure 2b. Figure 2c displays an SEM micrograph of the positive replica of the lotus leaf's texture produced by electrodepositing NC Ni on the gold-sputtered acetate film. High magnification details of this replica are seen in Figure 2d. Also, an optical 3-D profile of the textured surface is presented in Figure 2e. The surface of the textured NC Ni consisted of conical protuberances with a base radius of 5.0 ± 1.0 μm and a tip radius of 2.5 ± 0.5 μm. The protuberances were 10.0 ± 2.0 μm in height and had a planar density of 4×10^{-3} μm^{-2}. The contact angle of water droplets on the textured NC Ni surface was measured as 91˚, indicating that this replica did not have superhydrophobic properties similar to the lotus leaf.

Figure 2f shows a bright-field TEM image of the NC Ni films. The average grain size of the films was measured as 30 ± 4 nm, and their Vickers microhardness was determined as 4.42 ± 0.14 GPa.

Figure 3a displays the contact surface morphology of the NC Ni replica of the lotus leaf after 200 sliding cycles. During the friction tests, the counterface deformed and flattened the protuberance tips producing needle-like wear debris with a length of 10.0 ± 2.0 μm and a width of 0.65 ± 0.05 μm (i.e., aspect ratio $\approx$ 15). The high magnification micrograph presented in Figure 3b shows that the shear strain applied to each protuberance extruded the material in the sliding direction, causing it to accumulate

at the back of the protuberance. The debris might have formed as a result of material detaching from the longitudinal wear grooves seen in Figure 3b.

COF vs. sliding cycle curves for the textured and the flat NC Ni films are compared in Figure 4. Initially, the COF of the flat NC Ni surface was 0.30±0.02, but it increased rapidly and reached a peak of 0.54±0.05 at 60 sliding cycles. Then, it started to decrease gradually until it approached a value of 0.41±0.03 at 200 cycles. The COF curve of the textured NC Ni, however, started from a lower value of 0.20±0.02, and then increased to a peak value of only 0.38±0.02 (i.e., 30% lower than the peak COF of the flat film) at 70 cycles. It decreased slightly after passing this maximum and reached 0.33±0.03 at 200 cycles. The COFs of both samples increased initially due to the tendency of the real area of contact to increase [16]. This could be expressed as the initial conformation of the NC Ni's surfaces to the ball's contact surface [17]. Since the sliding tests were performed in air, formation of oxidized tribolayers on the contact surface of the flat NC Ni film reduced the COF of this sample after the peak [18], producing a pronounced peak COF. Figure 5 shows the tribolayers formed after 200 sliding cycles on the flat NC Ni surface. In the case of the textured NC Ni, however, oxidized tribolayers could not form on the contact surface because the wear debris could be transferred to the spaces between the contact points, i.e. protuberances (Figure 3a). As a result, this sample's COF did not decrease significantly after the peak, resulting in a less pronounced peak COF.

The most important observation arising from the examination of the COF curves is that the COF of the textured NC Ni surface remained significantly lower than that of the flat NC Ni throughout the friction test. Similar experimental observations have been reported for polymeric surfaces with similar surface textures [3,4]. Considering Tabor's

analysis [16], the frictional force between a sliding counterface and a soft material consists of a shear component (S) and a ploughing component (P):

$$f = S + P = \tau A^{real} + HA'$$ (1)

where τ is the shear strength of the soft material, A^{real} is the real area of contact, H is the hardness of the soft material and A' is the cross-sectional area of the counterface's indentation onto the soft material.

However, for a hard material under sufficiently low contact pressures, macroscopic indentation of the counterface onto the surface (i.e., indentation-induced deformation) is insignificant, and deformation occurs only at microscopic scale, i.e., it is limited to the asperity tips. Under these conditions, the cross-sectional area of the indentation (A') can be considered equivalent to the total asperity contact area, i.e., the real area of contact (A^{real}). For the present configuration (an alumina ball sliding on a hard NC Ni surface) the wear mechanism precludes macroscopic indentation-induced deformation of the sample's surface by the counterface, as previously shown by the authors [18]. Therefore, it can be assumed that A' is of the same order as A^{real}. Thus, the frictional force can be approximated as:

$$f = (\tau + H)A^{real}$$ (2)

Equation 2 implies that when the material properties remain constant, the frictional force only depends on the real area of contact. Consequently:

$$\frac{f_{textured}}{f_{flat}} = \frac{A^{real}_{textured}}{A^{real}_{flat}}$$ (3)

On the other hand, under a constant normal load, Amontons-Coulomb law gives:

$$\frac{f_{textured}}{f_{flat}} = \frac{\mu_{textured}}{\mu_{flat}}$$ (4)

135

where $\mu_{textured}$ and μ_{flat} are the COFs of the textured and the flat surfaces, respectively. Comparing Equations 3 and 4 yields:

$$\frac{\mu_{textured}}{\mu_{flat}} = \frac{A_{textured}^{real}}{A_{flat}^{real}} \tag{5}$$

Therefore, the lower COF of the textured NC Ni compared to the flat NC Ni's COF correlates with its smaller real area of contact.

3.2. Nanocrystalline Nickel Replica of the Boa's Skin: Obtaining Anisotropic Frictional Properties

Snake skin is known to have an asymmetric texture that results in anisotropic frictional properties, enhancing forward motion while restricting backward and lateral motions [12]. Figure 6a shows an optical 3-D profile of the surface of the red tail boa's skin, and Figure 6b is an SEM micrograph of this skin. The texture consists of microscopic scales with an average size of 16±4 μm (in the head-to-tail direction) separated by asymmetric protrusions. An SEM micrograph of the negative impression of the skin's texture on the acetate film is seen in Figure 6c, and an SEM micrograph of the positive NC Ni replica of this sample is displayed in Figure 6d. Figure 6e shows a typical optical 2-D profile of the textured NC Ni's surface, in the direction corresponding to the tail to head direction, revealing that the replicated protrusions had an asymmetric shape similar to the original ones.

The average COFs measured in different directions on the textured NC Ni film are presented in Figure 7. The average COF was the lowest in the head-to-tail direction (i.e., 0.061±0.014). In the reverse direction, tail-to-head, the average COF was higher (i.e.,

136

0.087±0.011). The highest average COF, however, was observed in the lateral direction where it was measured as 0.105±0.005. This directional variation of COF was consistent with the observation previously reported for a softer microcrystalline (MC) Cu replica of the same skin [19].

The observed frictional anisotropy is a result of the asymmetric shape of the protrusions at the scales' ridges (Figure 6e). In the head-to-tail direction there was only small resistance to the motion of the diamond tip on the textured film, while the asymmetric protrusions acted as pointed obstacles against the tip sliding in the tail-to-head direction, resulting in a higher COF in this direction. In the lateral direction, the linear density of protrusions was higher than that in the tail-to-head direction, and hence the tip had to overcome more obstacles. As a result, the highest COF corresponded to the lateral direction. This type of structure may have potential applications in systems such as clutches, where a range of different COF values can be obtained in various directions.

4. SUMMARY AND CONCLUSIONS

A double-stage replication technique was developed to produce biotextured nanocrystalline (NC) Ni films with a grain size of 30±4 nm and a hardness of 4.42±0.14 GPa. Two biological surfaces with different morphologies, i.e. lotus leaf and boa's skin, were replicated. The main conclusions arising from this study are as follows:

1. The NC Ni replica of the lotus leaf showed a lower COF compared to a flat NC Ni film with the same microstructure and hardness. Overall, the lower COF values of the textured film correlated with its smaller real area of contact. Also, the textured film showed a less pronounced peak COF compared to the flat film as the transfer of the wear

debris to the spaces between the protuberances prohibited the formation of oxidized tribolayers that could reduce the frictional forces after the peak COF.

2. The NC Ni replica of the boa's skin displayed frictional anisotropy as a result of the asymmetric shape of the protrusions at the scales' ridges. Thus, the method presented in this study provides a simple and effective way of controlling the friction between surfaces in contact.

REFERENCES

[1]   M. Urbakh, J. Klafter, D. Gourdon, J. Israelachvili, Nature 430 (2004) 525.

[2]   M. Scherge, S. Gorb, Biological Micro- and Nano-tribology, Springer, Berlin, 2001.

[3]   B. He, W. Chen, Q. Wang, in: Proc. Int. Joint Tribol. Conf., San Antonio, TX, USA, 2006.

[4]   R.A. Singh, E. Yoon, H.J. Kim, J. Kim, H.E. Jeong, K.Y. Suh, Mater. Sci. Eng. C27 (2007) 875.

[5]   Z. Burton, B. Bhushan, Nano Lett. 5 (2005) 1607.

[6]   A. Blatter, M. Maillat, S.M. Pimenov, G.A. Shafeev, A.C. Simakin, E.N. Loubnin, Wear 232 (1999) 226.

[7]   M. Wakuda, Y. Yamauchi, S. Kanzaki, Y. Yasuda, Wear 254 (2003) 356.

[8]   G. Ryk, Tribol. Trans. 45 (2002) 444.

[9]   M. Scherge, S. Gorb, Tribol. Lett. 8 (2000) 1.

[10]   A.P. Russell, J. Zool. Lond. 176 (1975) 437.

[11]   K. Autumn, Y.A. Liang, S.T. Hsieh, W. Zesch, W.P. Chan, T.W. Kenny, R. Fearing, R.J. Full, Nature 405 (2000) 681.

[12]   J. Hazel, M. Stone, M.S. Grace, V.V. Tsukruk, J. Biomech. 32 (1999) 477.

[13]   C. Neinhuis, W. Barthlott, Ann. Botany 79 (1997) 667.

[14]   W. Barthlott, C. Neinhuis, Planta 202 (1997) 1.

[15]   Y.T. Cheng, D.E. Rodak, C.E. Wong, C.A. Hayden, Nanotechnology 17 (2006) 1359.

[16]   F.P. Bowden, D. Tabor, The Friction and Lubrication of Solids, Oxford University Press, 1986.

[17]   M. Shafiei, A.T. Alpas, in: Proc. World Tribol. Conf. III, Washington, D.C., USA, 2005.

[18]   M. Shafiei, A.T. Alpas, Metall. Mater. Trans. A38 (2007) 1621.

[19]   M. Shafiei, A.T. Alpas, in: Proc. Intern. Conf. Micro Nano Technol., Vienna, Austria, 2007.

TABLE

Table 1. NC Ni electrodeposition parameters.

Current Type	DC
Current Density	0.05 A/cm2
Anode Type	Platinum
Electrolyte pH	4.5
Electrolyte Temperature	45 °C
Electrodepositing Duration	45 min.

FIGURES

(a)

(b)

(c)

(d)

(d)
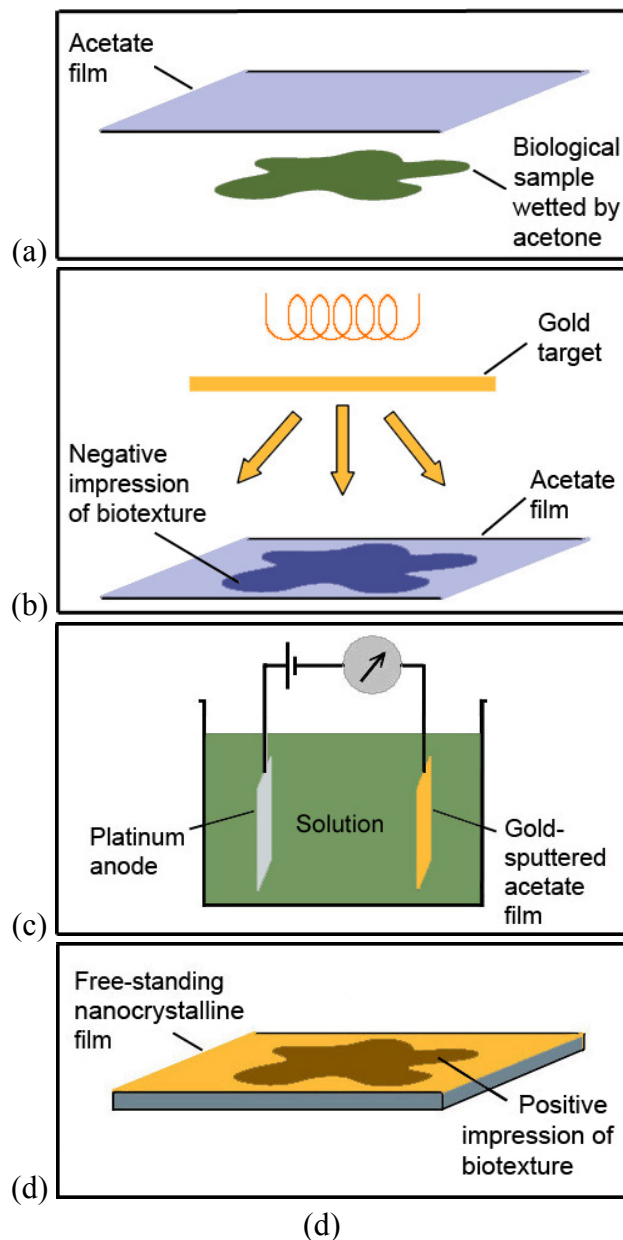
Figure 1. The main steps of the technique developed to fabricate hard NC metallic replicas of biotextures. (a): The surface texture of the biological sample is first replicated on an acetate film to obtain a negative impression of the biotexture. (b): A thin layer of gold is sputtered on the textured acetate film to provide a conductive surface. (c): A metallic layer, e.g. NC Ni, is electrodeposited on the top of the acetate film. (d): The acetate film is dissolved in acetone to obtain a free-standing replica of the biotexture.
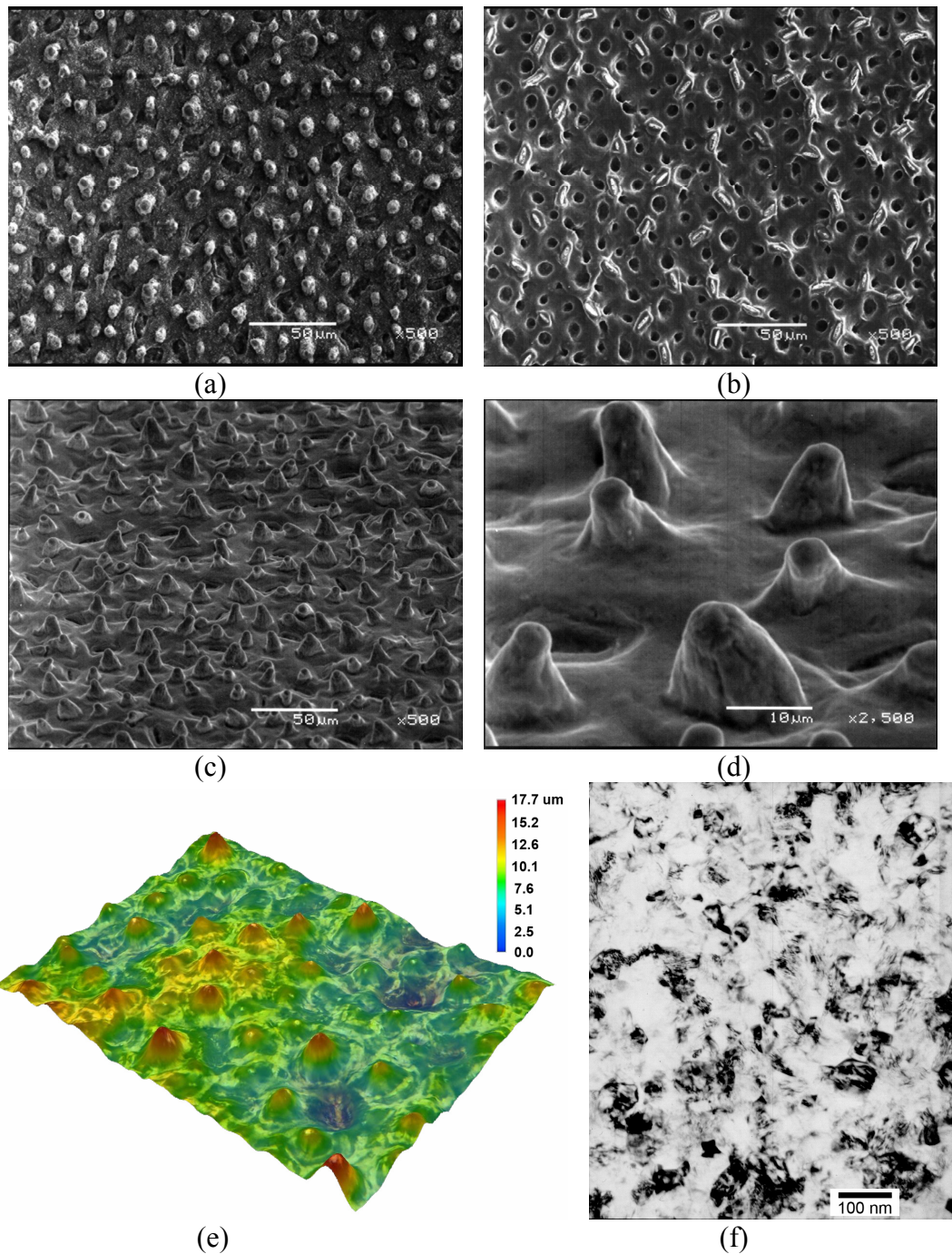
Figure 2. (a): An SEM micrograph of the surface texture of the lotus leaf. (b): An SEM micrograph of the negative impression of the leaf's texture on acetate film. (c): An SEM micrograph of the NC Ni replica of the lotus leaf. (d): A high magnification SEM micrograph of the texture shown in (c). (e): An optical 3-D profile of the NC Ni replica's surface. (f): A bright field TEM image of the NC Ni film.
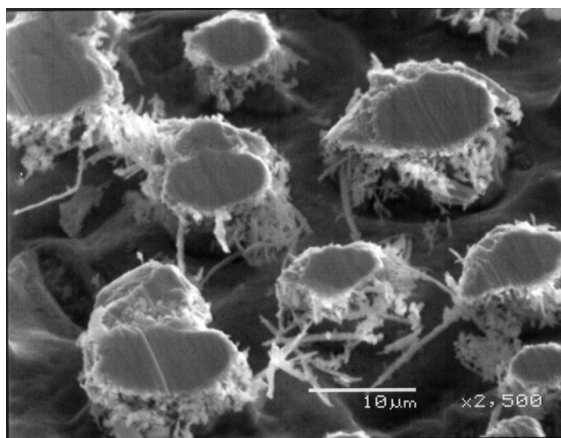
(a)
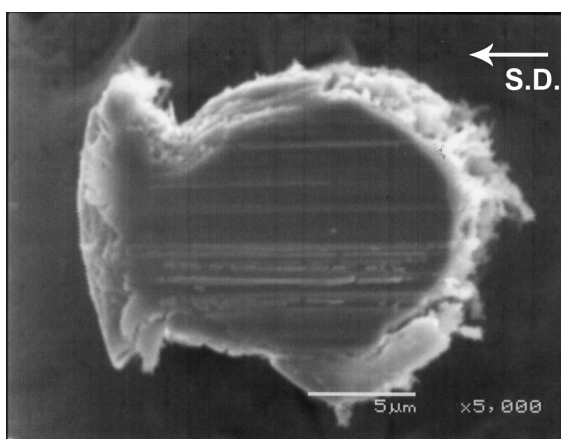
(b)

Figure 3. (a): The contact surface morphology of the NC Ni replica of the lotus leaf after 200 sliding cycles. The protuberance tips were flattened, and needle-like debris was scattered in the spaces between the protuberances. (b): A high magnification SEM micrograph of the texture shown in (a).
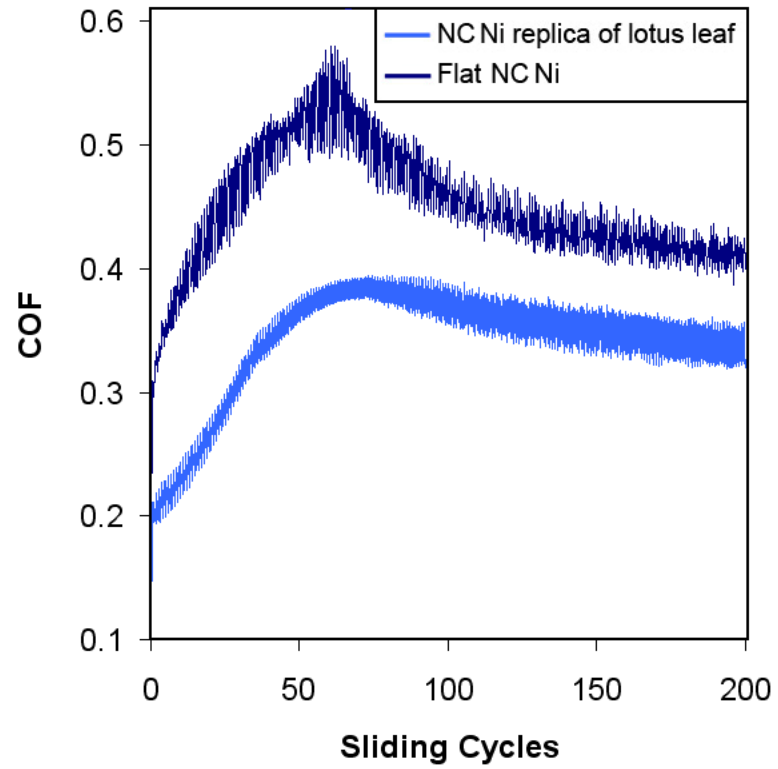
Figure 4. Variation of COF with sliding cycles measured on the NC Ni replica of the lotus leaf and the flat NC Ni film.
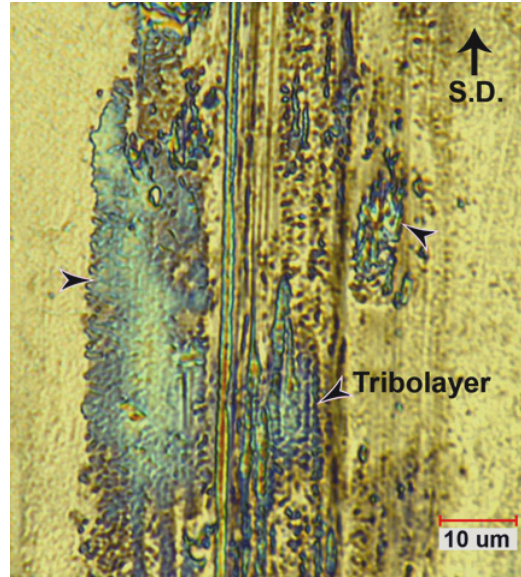
Figure 5. An optical micrograph of the worn surface of the flat NC Ni film after 200 sliding cycles. Arrows show tribolayers.
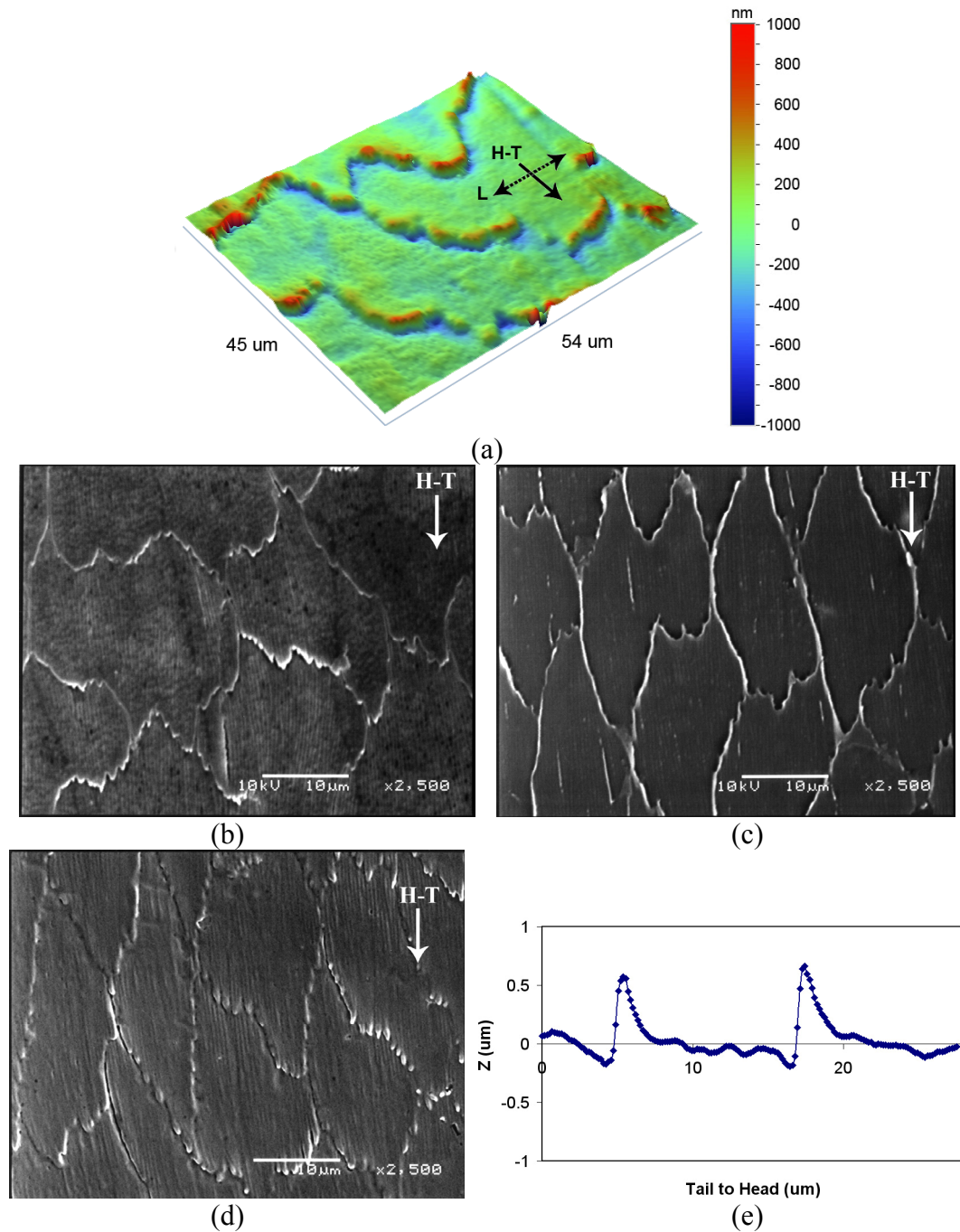
Figure 6. (a): An optical 3-D profile of the red tail boa's skin surface. The head-to-tail direction (H-T) is marked with a solid arrow, while the lateral direction (L) is shown with a dotted arrow. (b): An SEM micrograph of the boa's skin surface texture. (c): An SEM micrograph of the negative impression of the skin's texture on an acetate film. (d): An SEM micrograph of the NC Ni replica of the boa's skin. (e): A typical optical 2-D profile of the texture shown in (d).

146
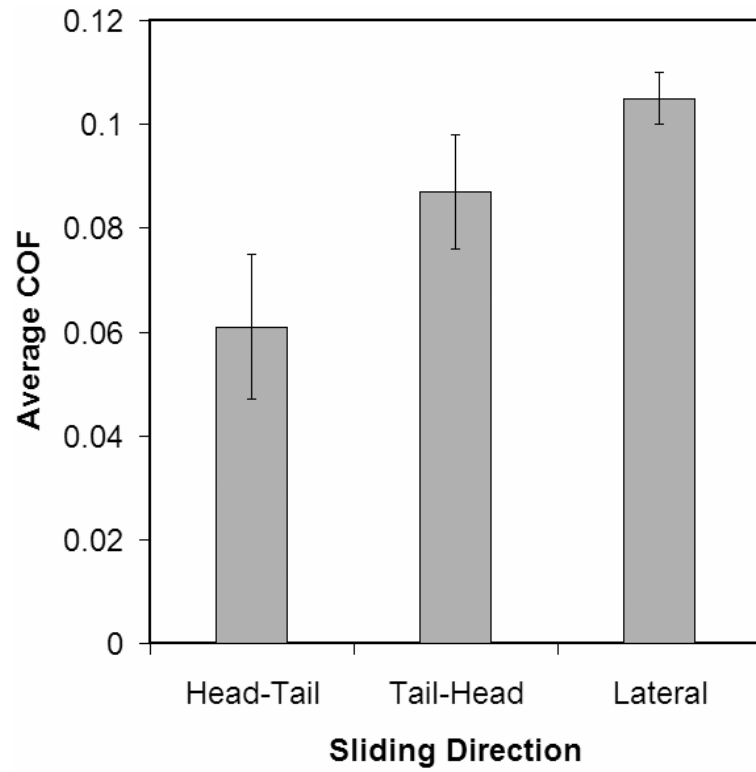
Figure 7. Average COFs of the NC Ni replica of the boa's skin measured in three different directions corresponding to the head-to-tail, tail-to-head and lateral directions.

CHAPTER 7

NANOCRYSTALLINE NICKEL FILMS WITH LOTUS LEAF TEXTURE FOR SUPERHYDROPHOBIC AND LOW FRICTION SURFACES

1. INTRODUCTION

The successful advancement of micro-electro-mechanical systems (MEMS) with miniature moving parts, including micromotors, gears and transmissions, mechanical discriminators and optical microswitches, relies on the development of new wear-resistant materials and surfaces with high hydrophobicity (water repellency) and low adhesion and friction [1-3]. Other possible applications for durable water repellent surfaces range from micro-fluidic devices [4] to bipolar plates in proton exchange membrane fuel cells (PEMFCs), because increasing hydrophobicity enhances the flow of both fluid and gas [5]. The objective of this work was to fabricate functional surfaces that simultaneously combined superhydrophobicity with high hardness and low coefficient of friction (COF).

The roughness of a surface has a significant effect on its wettability. The actual contact angle (θ) between a rough surface and a liquid droplet can be determined using [6]:

$$\cos\theta = r\cos\theta_T \tag{1}$$

where r is the roughness ratio (the actual surface area divided by the apparent surface area) and θ_T is the thermodynamic contact angle defined by [7]:

$$\cos\theta_T = \frac{\gamma_{sv} - \gamma_{sl}}{\gamma_{lv}} \tag{2}$$

where γ_{sv} is the solid-vapour surface energy, γ_{sl} is the solid-liquid interfacial energy and γ_{lv} is the liquid-vapour surface energy. As roughness increases, air can become trapped underneath the liquid locally, resulting in the formation of a composite surface with a large contact angle [8], a phenomenon that is described using the following theoretical equation [9]:

$$\cos\theta = f_S \cos\theta_T - f_{air} \tag{3}$$

where f_S is the fractional contact area between the liquid and the surface, and f_{air} is the fractional contact area between the liquid and the air underneath the droplet. On the other hand, increasing the roughness of a hard surface may also result in a reduction in friction by reducing the real area of contact with the counterface [10-13]. The relationship between COF and real area of contact can be expressed by the following equation [13]:

$$\frac{\mu_{textured}}{\mu_{smooth}} = \frac{A_{textured}^{real}}{A_{smooth}^{real}} \tag{4}$$

where $\mu_{textured}$ and μ_{smooth} are the COFs of the textured and smooth surfaces, and $A_{textured}^{real}$ and A_{smooth}^{real} are their corresponding real areas of contact. Therefore, by optimizing material properties and surface texture, it may be possible to design and fabricate superhydrophobic surfaces with low COFs.

The natural world offers multiple examples of surfaces with optimized wettability and frictional properties through a combination of surface texture and chemistry [14]. Some examples are the superhydrophobic lotus leaf [15], the water strider's leg [16], the cricket's attaching foot [17], the gecko's gripping foot [18,19], and the snake's textured

149

skin [20], all of which suggest that nature offers effective ways of controlling wettability and friction. The surface texture of the lotus leaf consists of microscopic protuberances covered in nanoscale, needle-like features with a waxy surface composition. This multilevel surface roughness is known as the source of the lotus leaf's superhydrophobicity [15,21,22]. A simple technique was developed previously by the authors [13] to produce nanocrystalline (NC) Ni films with a lotus leaf surface morphology. These films combined the microscale surface texture of the lotus leaf with the high hardness of the NC films, but the method failed to reproduce the nanoscale features. The method consisted of two steps:

i) replication of the lotus leaf surface texture on a cellulose acetate film to obtain a negative impression of the texture; and

ii) electrodeposition of NC Ni on the acetate film to obtain a hard replica of the leaf.

In the present study, this method was further developed by applying a short-duration electrodeposition and a PFPE solution treatment to the NC Ni lotus leaf replicas. In this way, microscale lotus leaf replicas with a nanoscale surface texture and a low surface energy were produced. Consequently, new surfaces with low friction and very high hydrophobicity, similar to that of the natural leaf but on a much harder surface, were obtained.

2. EXPERIMENTAL PROCEDURES

2.1. Fabrication

The main steps in the fabrication of NC Ni replicas from the lotus leaf are schematically illustrated in Figures 1a-e. In the first step (Figure 1a), the surface texture

of the lotus leaf was replicated on a cellulose acetate film to obtain a negative impression of the texture. In the next step (Figure 1b), a thin layer of Au (90±30 nm) was sputtered on the acetate film to provide a conductive surface. The Au-coated acetate film was then placed in an electrolytic cell for 45 minutes to deposit an NC Ni layer with a thickness of 77±4 μm (Figure 1c). The chemistry of the electrodeposition bath and the process parameters used are given elsewhere [13]. The acetate film was then dissolved in acetone to obtain a self-sustaining NC Ni replica of lotus leaf surface consisting of conical protuberances.

A short-duration secondary electrodeposition (SED) process was applied to modify the microscale surface texture. The bath composition and the parameters of the SED process were the same as those of the primary electrodeposition (PED) process, but with a much shorter duration (120 s and 300 s). Ni was then preferentially deposited on the tips of the protuberances due to the high local current densities there. Figure 1d illustrates the deposited Ni, which is in the shape of spherical cups with a smaller curvature than the initial tips of the protuberances. This morphology is termed as "Ni crown".

The surfaces were then dipped for 180 s in an ethoxysilane-terminated perfluoropolyether (PFPE) derived solution that consisted of 1 wt% Fluorolink® S10, 4 wt% water, 1 wt% acetic acid and 94 wt% isopropyl alcohol. They were then cured at 100°C for 30 minutes. The primary objective of this treatment was to reduce the surface energy (PFPE-derived coatings have very low surface energies [23]), but the low PH of the PFPE-derived solution could also result in the formation of a nanotextured surface by etching the "Ni crowns" (Figure 1e), which should further enhance the water repellency of the obtained surfaces.

For comparison, NC Ni films were also electrodeposited on Au-sputtered smooth acetate films (without lotus leaf texture) using the PED process. The acetate film was dissolved in acetone to obtain a smooth NC Ni film with a roughness of 11±2 nm and a thickness of 63±6 μm. Table 1 lists the specifications of all the fabricated films, and the designations used to identify them in the rest of the paper.

2.2. Characterization

The surface morphologies of the samples were studied using an FEI Quanta 200 FEG environmental scanning electron microscope (SEM) at a tilt angle of 40°. A JEOL 2010F transmission electron microscope (TEM) was employed to determine the average grain size of the NC Ni films by using the conventional linear intercept method on several TEM micrographs, and the Vickers microhardness of the NC Ni films was verified using a load of 0.25 N.

The static contact angles between the films' surfaces and 10 μL water droplets were measured using a Kruss DSA10L system. During these measurements, water was deposited on the surfaces at a rate of 0.33 μL/s.

The COFs of the textured surfaces were measured using a CSM pin-on-disc tribometer operating under a load of 1.0 N at a sliding speed of 0.01 m/s. An alumina (Al_2O_3) ball with a diameter of 3.18 mm and a hardness of 18.64±0.39 GPa was fixed at the end of a pin and used as the counterface. The friction tests were conducted in ambient air with 35% relative humidity.

To study the cross-sectional microstructures of the protuberances, focused ion beam (FIB) investigations were carried out using a Zeiss NVision 40 dual beam SEM/FIB

instrument. First, a thin layer of carbon was deposited on the area of interest to protect the surface features against beam damage during ion-milling. Then, a narrow trench was milled, using Ga-ion beam currents ranging from 13 nA to 700 pA at a voltage of 30 KV, to produce a smooth section perpendicular to the sample's surface. To minimize beam damage during observation, a low ion beam current of 10 pA was used. The dual beam angle in the SEM/FIB system this study used was 54°, which implies that the FIB images were recorded at a tilt angle of 54°.

3. RESULTS AND DISCUSSION

3.1. Microstructures and Morphologies

Figure 2a shows an SEM micrograph of the surface texture of lotus leaf, and Figure 2b shows the needle-like nanotexture covering the surface of a protuberance. A negative impression of the lotus leaf's surface texture on a cellulose acetate film (obtained by the replication method shown in Figure 1a) is seen in Figure 2c, and an enlarged view of a protuberance impression on this film is shown in Figure 2d. PED of NC Ni on this acetate film resulted in a hard replica of the leaf's surface texture, which is shown in Figure 2e (S1 in Table 1). The planar density of the conical protuberances was 4×10^3 mm^{-2}, and they had a height of 10.0 ± 2.0 μm, a tip radius of 2.5 ± 0.5 μm and a base radius of 5.0 ± 1.0 μm. Figure 2f provides an enlarged view of a protuberance on this sample, revealing that the replicated protuberances had the same height and overall shape as the protuberances in the original leaf, but that their surfaces were featureless (compare Figures 2b,f).

A cross-sectional FIB image of a protuberance on the electrodeposited NC Ni lotus leaf replica is presented in Figure 3a. This micrograph shows the columnar grain growth

from the Au layer towards the centre of the protuberance, where an equiaxed grain structure is recognizable. A bright field TEM image with the corresponding selected area electron diffraction (SAED) pattern obtained from the top of the equiaxed grain region is presented in Figure 3b. The average grain size of the NC Ni measured was 30±4 nm. The Vickers microhardness of the films was determined to be 4.42±0.14 GPa using a load of 0.25 N.

Figures 4a,b show the backscattered electron (BSE) and secondary electron (SE) micrographs of the NC Ni lotus leaf replica after it had been treated with the PFPE solution (S2). This treatment covered the surface with a thin, non-uniform film of PFPE, which was blistered in some areas (dark spots on the white Au layer in the BSE image in Figure 4a). However, it was unable to etch the surface of this sample to form a nanoscale texture (see Figure 4c for a higher magnification SE micrograph of a protuberance), because the surface was covered with a continuous Au film.

The BSE and SE micrographs of the lotus leaf's surface features after the 120 s SED process (S3) are shown in Figures 5a,b. The SED process formed "Ni crowns" (features of darker colour in the BSE micrograph shown in Figure 5a). These "Ni crowns" were formed on almost all of the protuberances, increasing their height to 14.0±2.0 μm and their tip radius to 6.0±0.5 μm. Some Ni spheres were also deposited between the protuberances. Figure 5c shows a higher magnification SE micrograph of a protuberance on this sample.

Figures 5d,e show the BSE and SE micrographs of the 120 s SED replica after it had been treated with the PFPE solution (S4). The surfaces between the protuberances are intact (not etched by the PFPE solution), because they were protected by the Au film.

This treatment has, however, created a nanoscale texture on the surfaces of the "Ni crowns" (see Figure 5f for a higher magnification SE micrograph of a protuberance).

The BSE and SE micrographs of the lotus leaf replica's surface features after the 300 s SED process (S5) are shown in Figures 6a,b. The SED Ni appears as clustered spheres of darker colour in the BSE micrograph shown in Figure 6a. Similar to the shorter-time SED process, "Ni crowns" were formed on the protuberances, but a large number of clustered Ni spheres could also be seen in the areas between these features. Figure 6c shows a higher magnification SE micrograph of a protuberance on this sample.

Figures 6d,e show the BSE and SE micrographs of the 300 s SED replica after it had been treated with the PFPE solution (S6). It is seen that this treatment has created a nanoscale texture on the surfaces of the clustered Ni spheres and the "Ni crowns" (see Figure 6f for a higher magnification SE micrograph of a protuberance).

Cross-sectional FIB image of a protuberance on the lotus leaf replica after the 120 s SED process and the PFPE solution treatment (S4) is displayed in Figure 7, which reveals the microstructures of the protuberance and its "Ni crown". Careful observation of this micrograph suggests that: i) the Ni grains are relatively larger inside the crown, which could be caused by the high current densities generated on the protuberances during the SED process; and ii) the surface of the "Ni crown" has been etched by the PFPE solution, creating a nanotextured surface.

3.2. Contact Angles

The water contact angles with the corresponding shapes of the water droplets on the NC Ni surfaces are presented in Figure 8a. The smooth NC Ni surface had a low contact

angle of $\theta(S7) = 64\pm2°$, whereas the replication of lotus leaf surface texture provided an NC Ni surface that had a contact angle of $\theta(S1) = 91\pm2°$. On the other hand, the PFPE treatment of the smooth surface lowered its surface energy, leading to an increase in its contact angle from $\theta(S7) = 64\pm2°$ to $\theta(S8) = 90\pm2°$. When these two effects (surface texture and low surface energy) were combined in S2, a contact angle of $\theta(S2) = 120\pm3°$ was recorded, which was 33% higher than those obtained by applying each of these two effects alone.

Depositing "Ni crowns" on the protuberances of the NC Ni lotus leaf replica did not lead to any significant increase in the contact angle. This is evident from comparing the contact angles of S1, S3 and S5 where $\theta(S1) = 91\pm2°$ and $\theta(S3) = \theta(S5) = 94\pm2°$.

The NC Ni lotus leaf replica with the 120 s SED process, followed by the PFPE treatment, displayed the highest contact angle of $\theta(S4) = 156\pm3°$. The SED process deposited microscale "Ni crowns" on the protuberances, and the PFPE solution treatment created a nanoscale surface texture with a low surface energy on those crowns. The combination of this multilevel surface roughness and low surface energy produced a synergy that resulted in a more than 140% increase in the NC Ni's contact angle. The PFPE-treated protuberances with nanotextured Ni crowns (S4) could readily sustain water droplets without allowing contact with the entire surface, forming superhydrophobic surfaces similar to that of the lotus leaf (Figure 8b).

It should be noted that increasing the SED process duration from 120 s to 300 s led to a small reduction in the contact angle, from $\theta(S4) = 156\pm3°$ to $\theta(S6) = 146\pm3°$. This reduction could be justified using Equation 3, which suggests that an increase in the fractional contact area of the liquid with the surface (f_S) would lead to a reduction in the

actual contact angle. After 120 s of SED, "Ni crowns" were formed on almost all of the protuberances. Continuing this process for a longer duration (i.e., 300 s in the case of S6) resulted in the deposition of clustered Ni spheres in the areas between the original protuberances. This increased the f_S and reduced the size of the microscopic air pockets optimized by nature in the lotus leaf.

3.3. Friction and Wear Properties

The morphology and microstructure of the worn protuberances on the NC Ni lotus leaf replica (S1) after sliding for 500 cycles are shown in Figures 9a,b. The alumina counterface plastically deformed and extruded the material at the protuberance tips in the sliding direction. This led to the accumulation of deformed material around the protuberances (Figure 9a). The wear debris particles might have been generated by the micro-ploughing action of the couterface, evident from the longitudinal wear grooves on the contact surface of each protuberance in Figure 9a. The continuous transfer of these wear debris particles to the spaces between the protuberances prevented the formation of tribolayers on the contact surfaces of the textured samples. Such tribolayers could readily form on the contact surfaces of the smooth samples [24].

Figure 9a also shows a trench that was milled by FIB, parallel to the sliding direction, to investigate the evolution in a protuberance's cross-sectional microstructure. As seen in Figure 9b, the grains on the contact surface were aligned towards the sliding direction. During each pass, the counterface extruded out the material that was deformed in the previous passes and accumulated it at the back of the protuberance, forming a curved arm of aligned grains after sliding for 500 cycles (Figure 9b).

COF versus sliding cycle curves for all of the NC Ni films are compared in Figures 10a-h, and their steady-state COFs are presented in Figure 11. The initial COFs measured for the textured surfaces (Figures 10a-f) were lower than those for the smooth surfaces (Figures 10g,h), a result that could be correlated with the smaller real area of contact in the textured surfaces, as explained by Equation 4. The steady-state COFs of the textured and the smooth NC Ni surfaces prior to the PFPE treatment (S1, S3, S5 and S7), however, were similar, and had a value of about 0.40. Also, the effect of the PFPE treatment on both the textured and the smooth surfaces was to significantly reduce their steady-state COFs to about 0.16 for S2, S4 and S8 (60% reduction), and to 0.29 in the case of S6 (24% reduction). Hence, for samples with similar surface energies (e.g., S1, S3, S5 and S7), the steady-state COFs of the textured surfaces (S1, S3 and S5) were similar to that of the smooth surface (S7).

After the initial high-COF period in the smooth NC Ni surfaces, the formation of tribolayers reduced the COFs of these surfaces, which resulted in a peak in their COF curves (Figures 10g,h). However, the initial COFs of the textured surfaces were lower (due to their smaller real area of contact), and no decline occurred in their steady-state COFs (because protective tribolayers could not form on their contact surfaces), resulting in the absence of COF peaks in the textured surfaces (Figures 10a-f). It is interesting to note that the NC Ni replicas with the 300 s SED process with or without the PFPE treatment (S5 and S6) almost displayed a peak in their COF curves (Figures 10e,f), due to the large number of clustered Ni spheres that existed between the original protuberances (Figures 6a,d). These extra surface features (compared to S3 and S4) increased the real area of contact with the counterface and prevented the transfer of the wear debris to the

areas between the original protuberances (encouraging the formation of tribolayers), both of which promoted the appearance of a small peak in the COF curve, though not as noticeable as in the case of the smooth surfaces (compare Figures 10e,f with Figures 10g,h). Moreover, compared to the original protuberances and their crowns, the Ni spheres between the protuberances were not strongly bonded to the surface. Consequently, the sliding-induced stresses could easily separate them from the surface and transform them from functional surface features into destructive third bodies in sliding wear, which would increase the steady-state COFs (compare Figure 10f with Figures 10b,d,h). Hence, the longer SED process in S6 (compared to S4) had a negative impact on its COF, similar to hydrophobicity.

The lowest COFs were exhibited by S2 and S4 (Figures 10b,d). It is important to note that the nanoscale surface texture of the protuberances, which played an important role in increasing the hydrophobicity in S4, was not useful in lowering the COF values of this sample further (compared to S2, which only had a microscale texture). The functionality of such nanoscale textures in nano-tribosystems, however, remains to be explored.

4. CONCLUSIONS

1. Lotus leaf surface-textured nanocrystalline (NC) Ni films, developed using replication of original biotexture, were modified by a selective electrodeposition and a PFPE solution treatment to produce surfaces with low coefficient of friction (COF = 0.16) and high hydrophobicity ($\theta = 156°$), similar to that of the natural lotus leaf but on a much harder surface (H = 4.42 GPa).

2. The superhydrophobicity of the NC Ni films was attributed to successful development of a multi-level surface roughness (where a nanoscale surface texture was superimposed on a microscale structure of protuberances) with a low surface energy.

3. The microscale protuberances reduced the real area of contact and removed the wear debris particles from the contact surfaces simultaneously, eliminating the initial high COF peaks observed when smooth NC Ni films were tested. Additionally, the PFPE treatment of the smooth and textured surfaces resulted in a 60% reduction in the steady-state COFs.

REFERENCES

[1]   B. Bhushan, J.N. Israelachvili, U. Landman, Nature 374 (1995) 607.

[2]   B. Bhushan, Tribology Issues and Opportunities in MEMS, Kluwer Academic Publishers, Dordrecht, Netherlands, 1998.

[3]   J.G. Kushmerick, M.G. Hankins, M.P. de Boer, P.J. Clews, R.W. Carpick, B.C. Bunker, Tribol. Lett. 10 (2001) 103.

[4]   K. Huikko, P. Ostman, K. Grigoras, S. Tuomikoski, V.M. Tiainen, A. Soininen, K. Puolanne, A. Manz, S. Franssila, R. Kostiainen, T. Kotiaho, Lab Chip 3 (2003) 67.

[5]   S.J. Lee, C.H. Huang, J.J. Lai, Y.P. Chen, J. Power Sources 131 (2004) 162.

[6]   R.N. Wenzel, Ind. Eng. Chem. 28 (1936) 988.

[7]   A.W. Adamson, A.P. Gast, Physical Chemistry of Surfaces, Wiley, New York, 1997, p. 353.

[8]   A. Tuteja, W. Choi, G.H. McKinley, R.E. Cohen, M.F. Rubner, Mater. Res. Soc. Bull. 33 (2008) 752.

[9]   A.B.D. Cassie, S. Baxter, Trans. Faraday Soc. 3 (1944) 16.

[10] B. He, W. Chen, Q. Wang, in: Proc. Int. Joint Tribol. Conf., San Antonio, TX, USA, 2006.

[11] R.A. Singh, E. Yoon, H.J. Kim, J. Kim, H.E. Jeong, K.Y. Suh, Mater. Sci. Eng. C27 (2007) 875.

[12] Z. Burton, B. Bhushan, Nano Lett. 5 (2005) 1607.

[13] M. Shafiei, A.T. Alpas, Mater. Sci. Eng. 28C (2008) 1340.

[14] M. Scherge, S. Gorb, Biological Micro- and Nano-tribology, Springer, Berlin, 2001.

[15] C. Neinhuis, W. Barthlott, Ann. Bot. 79 (1997) 667.

[16] X. Gao, L. Jiang, Nature 432 (2004) 36.

[17] M. Scherge, S. Gorb, Tribol. Lett. 8 (2000) 1.

[18] A.P. Russell, J. Zool. Lond. 176 (1975) 437.

[19] K. Autumn, Y.A. Liang, S.T. Hsieh, W. Zesch, W.P. Chan, T.W. Kenny, R. Fearing, R.J. Full, Nature 405 (2000) 681.

[20] J. Hazel, M. Stone, M.S. Grace, V.V. Tsukruk, J. Biomech. 32 (1999) 477.

[21] W. Barthlott, C. Neinhuis, Planta 202 (1997) 1.

[22] Y.T. Cheng, D.E. Rodak, C.E. Wong, C.A. Hayden, Nanotechnology 17 (2006) 1359.

[23] G. Gu, X. Shen, F. Qing, App. Surf. Sci. 253 (2007) 6980.

[24] M. Shafiei, A.T. Alpas, Metall. Mater. Transact. 38A (2007) 1621.

TABLE

Table 1. Summary of the fabricated NC Ni samples with different surface features and their designations used to identify them.

| Sample	Description	Surface Features
S1	NC Ni lotus leaf replica	Protuberances
S2	S1 treated with the PFPE solution	PFPE-treated protuberances
S3	NC Ni lotus leaf replica with the 120 s SED	Protuberances with Ni crowns
S4	S3 treated with the PFPE solution	PFPE-treated protuberances with nanotextured Ni crowns
S5	NC Ni lotus leaf replica with the 300 s SED	Protuberances with Ni crowns; Ni spheres
S6	S5 treated with the PFPE solution	PFPE-treated protuberances with nanotextured Ni crowns; nanotextured Ni spheres
S7	NC Ni deposited on a smooth replica surface	Smooth surface
S8	S7 treated with the PFPE solution	PFPE-treated smooth surface
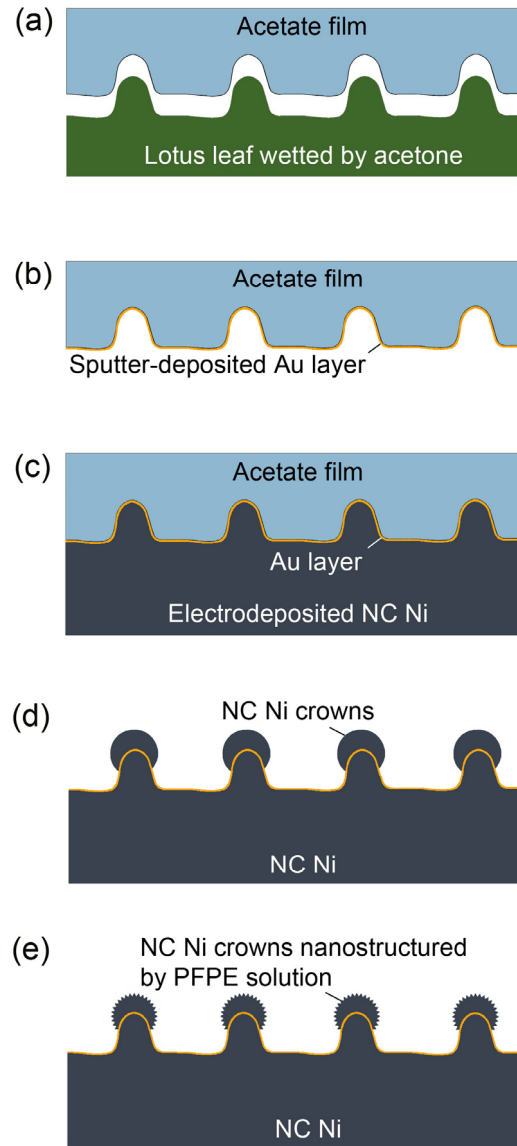
Figure 1. Schematic illustration of the main steps of the method developed to fabricate NC Ni lotus leaf replicas. (a): The surface texture of the lotus leaf was replicated on a cellulose acetate film to obtain a negative impression. (b): A thin layer of Au was sputtered on the textured acetate film to provide a conductive surface. (c): A layer of NC Ni was electrodeposited on the acetate film. (d): The acetate film was dissolved in acetone to obtain a free-standing replica of the lotus leaf, and then a short-duration SED process was applied to deposit "Ni crowns" on the protuberances' tips. (e): A PFPE solution treatment of the surface created a nanotextured layer on the "Ni crowns".
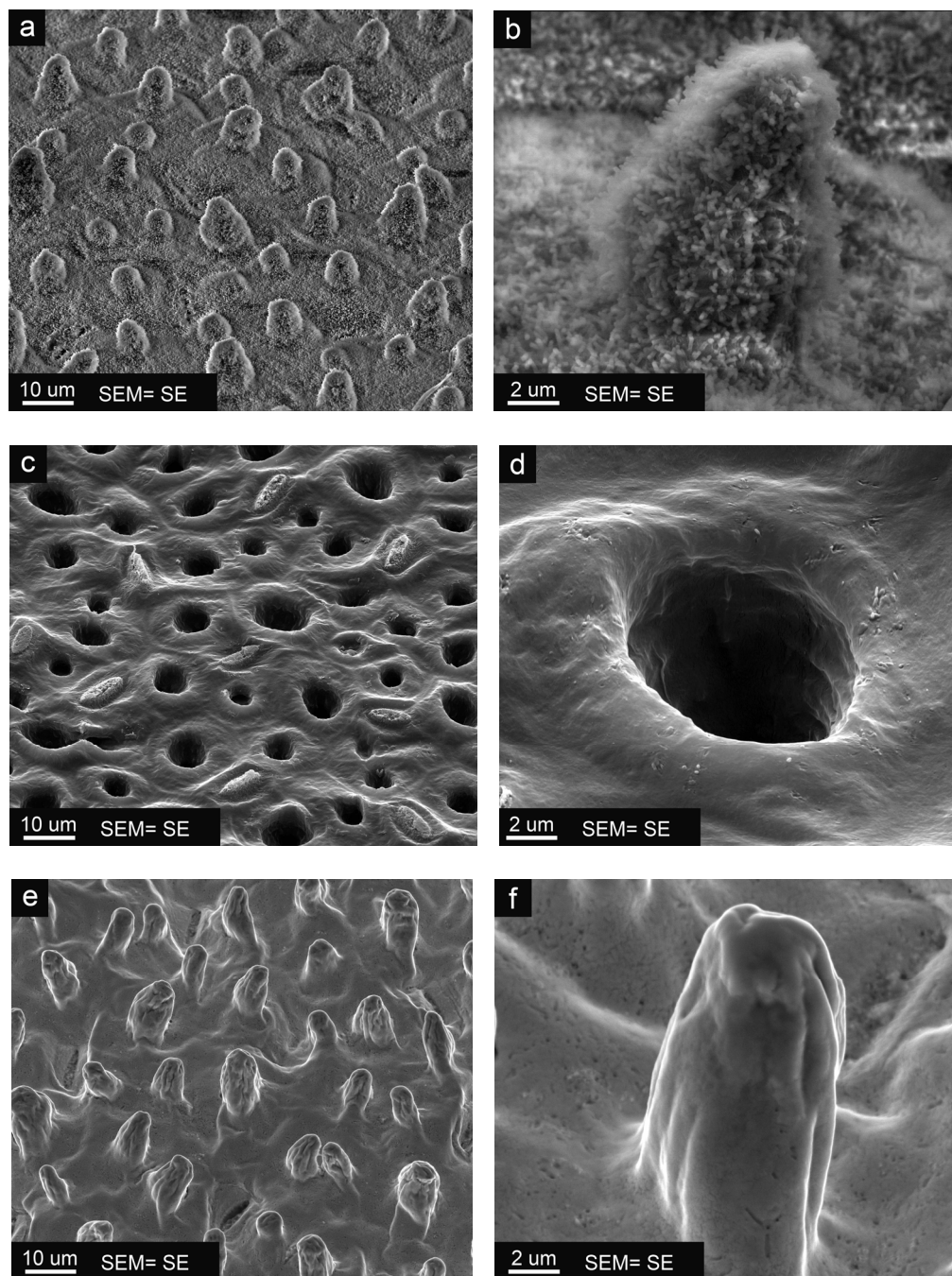
Figure 2. (a): An SEM micrograph of the surface texture of a carbon-coated lotus leaf. (b): The needle-like nanotexture covering the surface of a protuberance on the lotus leaf. (c): A negative impression of the lotus leaf's surface texture on a cellulose acetate film. (d): A higher magnification image of a protuberance's impression on the acetate film shown in (c). (e): NC Ni replica of the acetate film obtained by the PED process. (f): A higher magnification image of a protuberance on the NC Ni replica shown in (e).
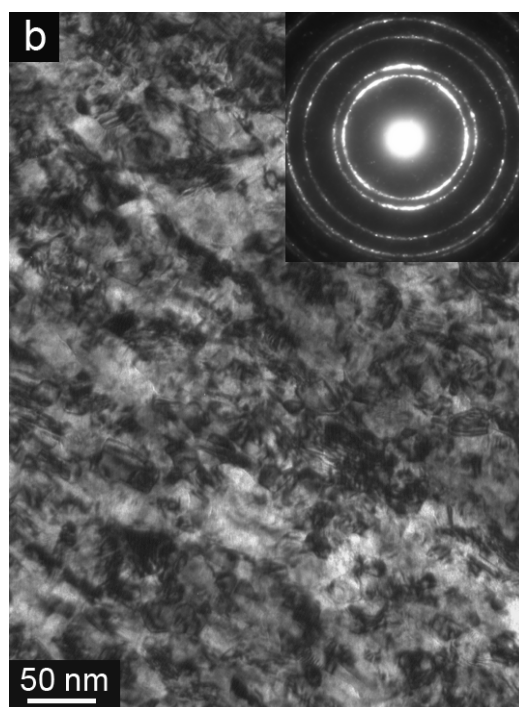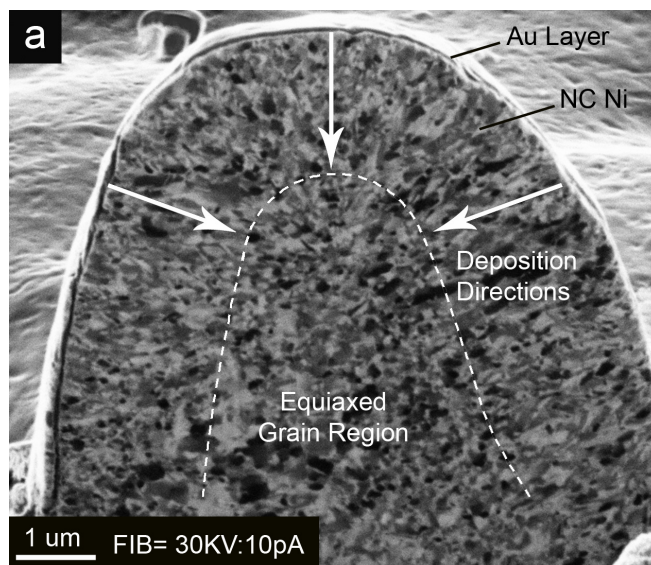
Figure 3. (a): A cross-sectional FIB image of a protuberance on the NC Ni lotus leaf replica (S1). (b): A bright field TEM image of the cross-section of the NC Ni deposits at the tip of a protuberance. The inset shows the corresponding SAD patterns.
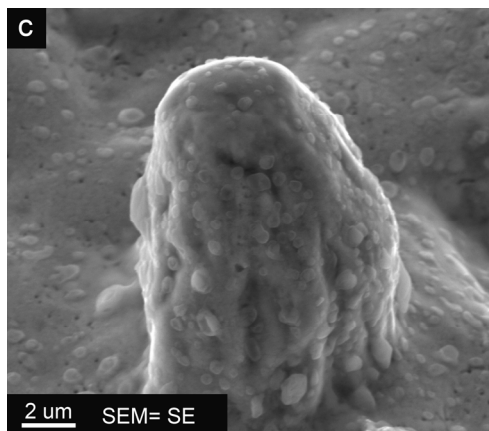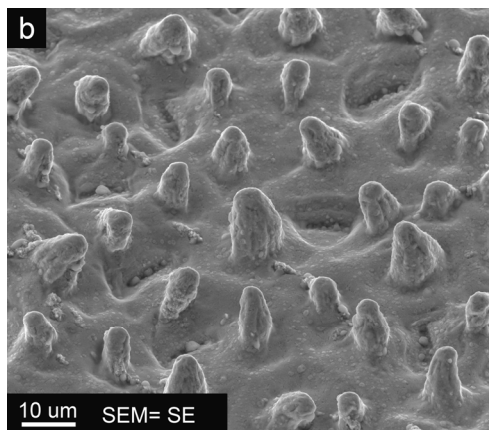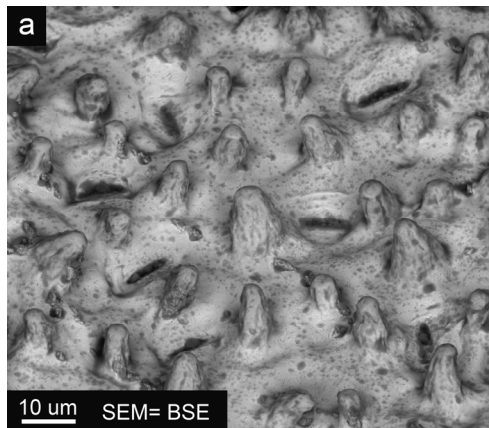
Figure 4. (a): A BSE image of the NC Ni lotus leaf replica after PFPE solution treatment (S2). (b): SE image of the surface shown in (a). (c): A higher magnification SE image of a protuberance on the surface shown in (b).
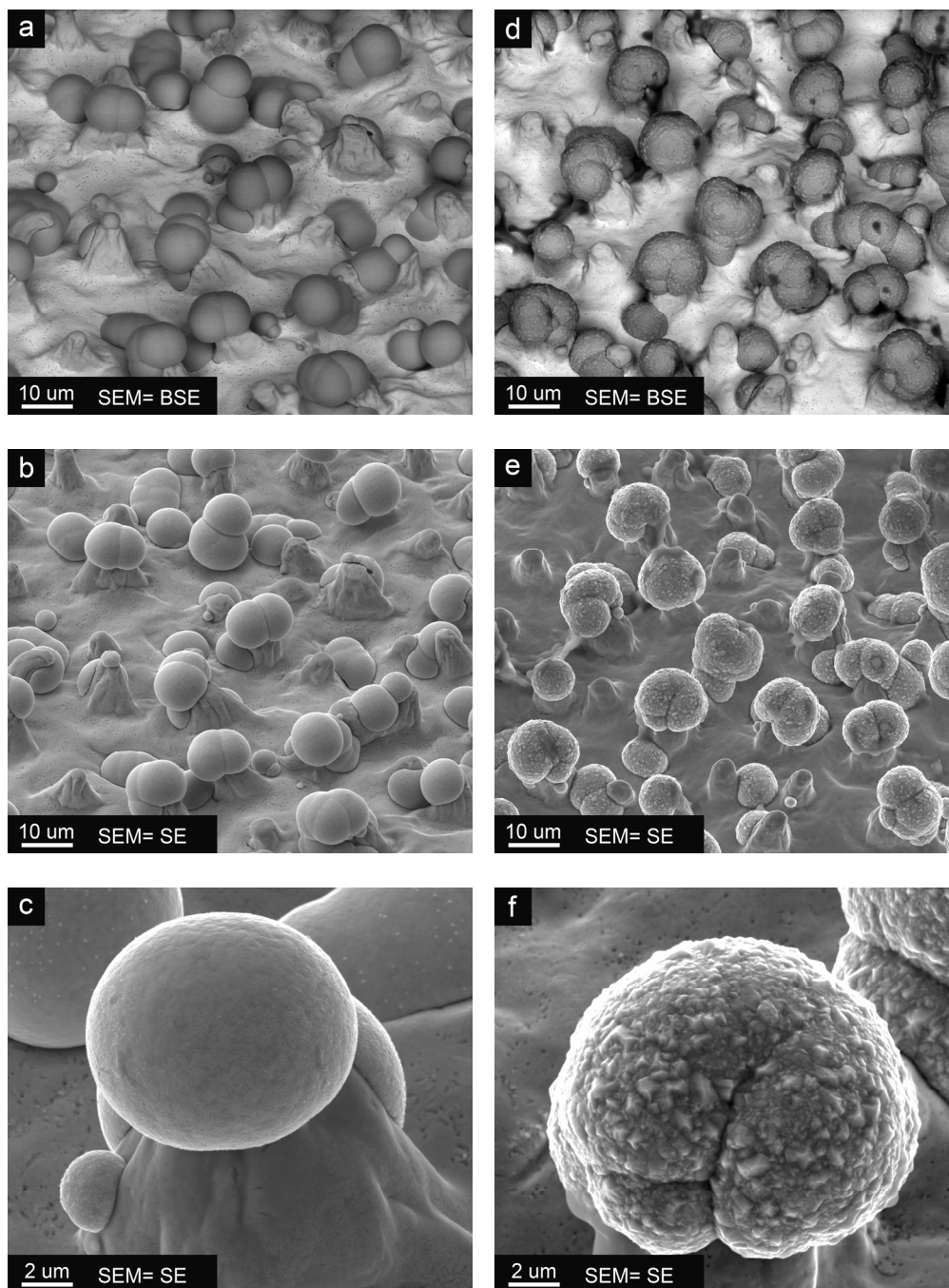
Figure 5. (a): A BSE image of the NC Ni lotus leaf replica after 120 s of SED process (S3). (b): SE image of the surface shown in (a). (c): A higher magnification SE image of a protuberance on the surface shown in (b). (d): A BSE image of NC Ni lotus leaf replica after 120 s of SED process and the PFPE solution treatment (S4). (e): SE image of the surface shown in (d). (f): A higher magnification SE image of a protuberance on the surface shown in (e).
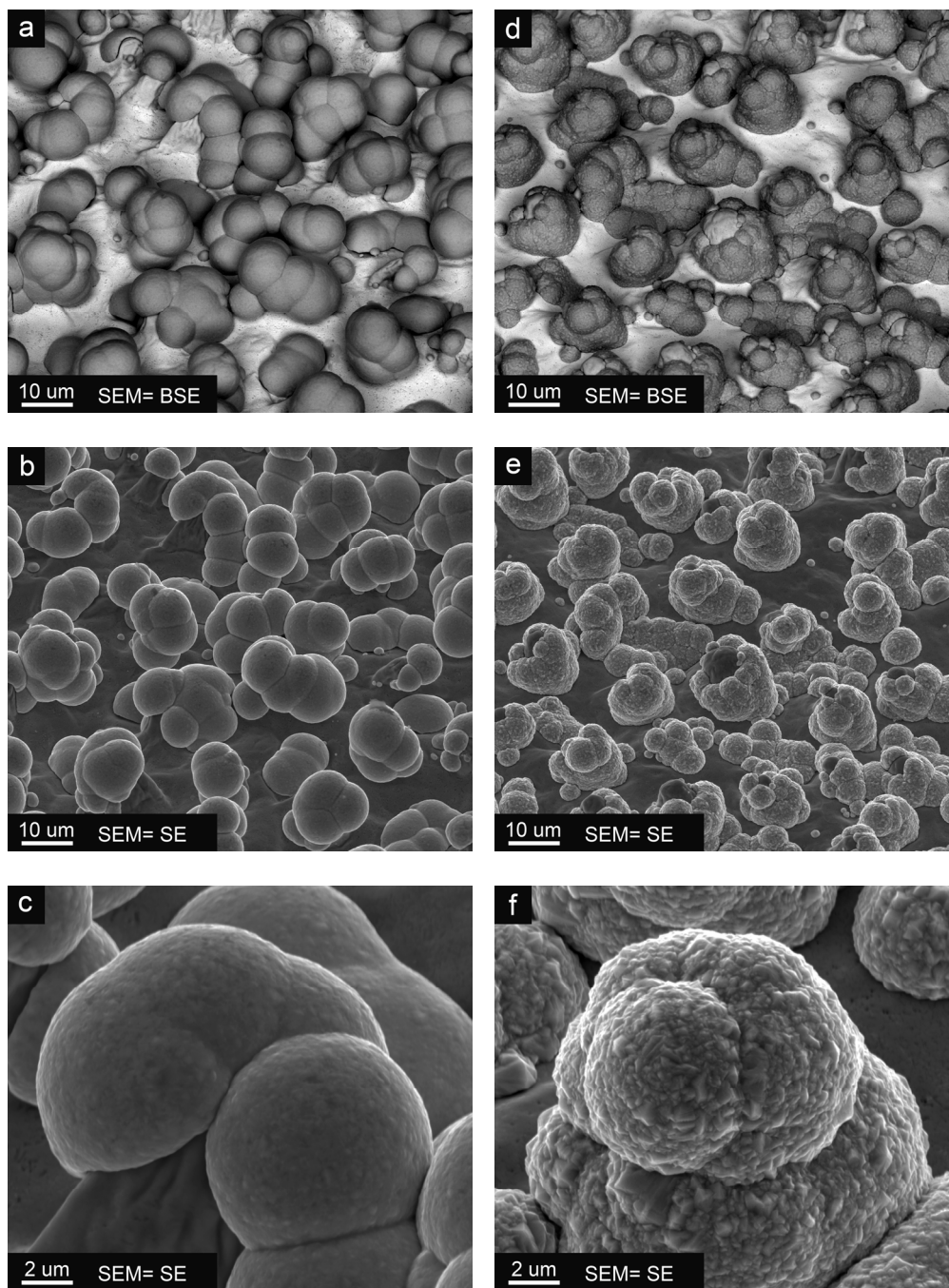
Figure 6. (a): A BSE image of the NC Ni lotus leaf replica after 300 s of SED process (S5). (b): SE image of the surface shown in (a). (c): A higher magnification SE image of a protuberance on the surface shown in (b). (d): A BSE image of NC Ni lotus leaf replica after 300 s of SED process and the PFPE solution treatment (S6). (e): SE image of the surface shown in (d). (f): A higher magnification SE image of a protuberance on the surface shown in (e).
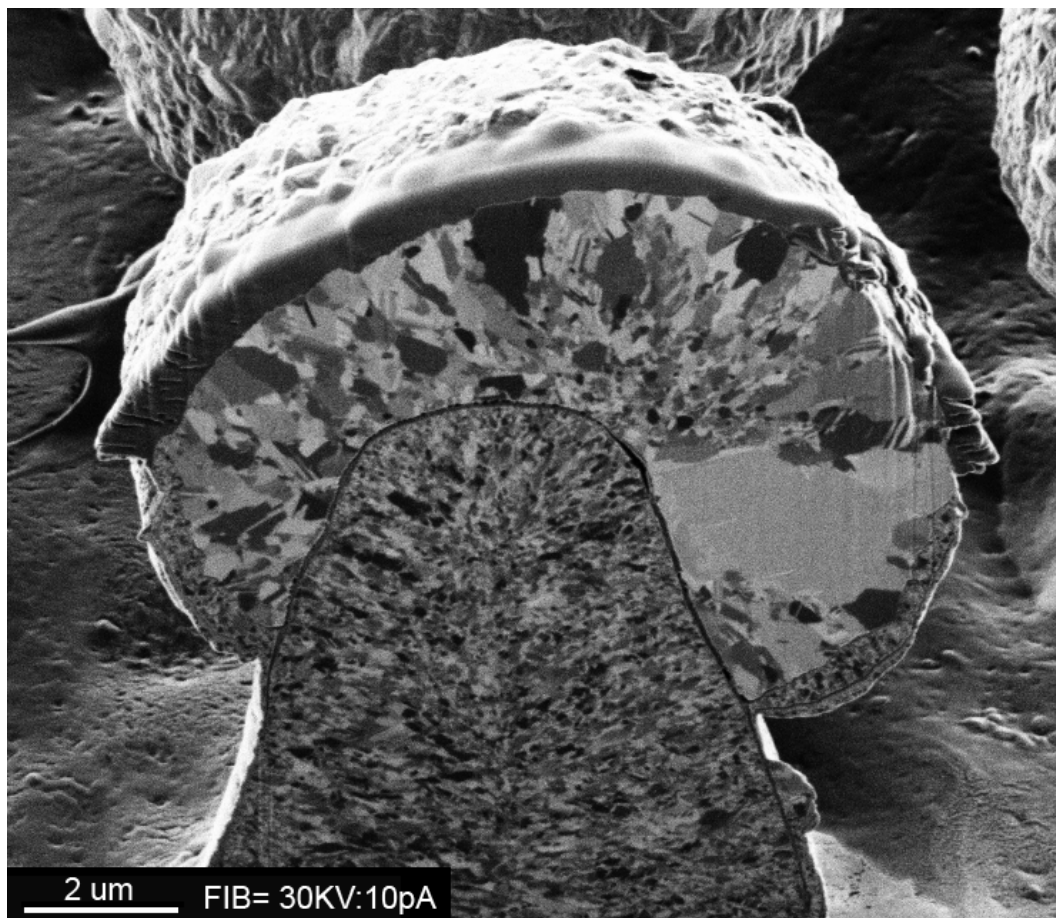
Figure 7. A cross-sectional FIB image of a protuberance on the lotus leaf replica after 120 s of SED process and the PFPE solution treatment (S4), which reveals the microstructures of the protuberance and its "Ni crown".
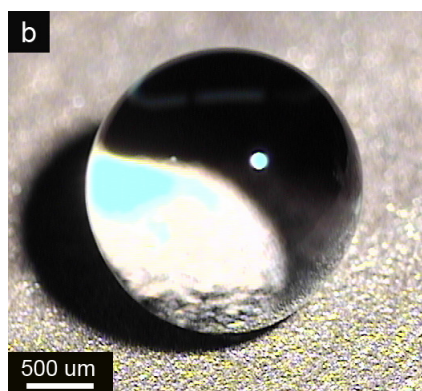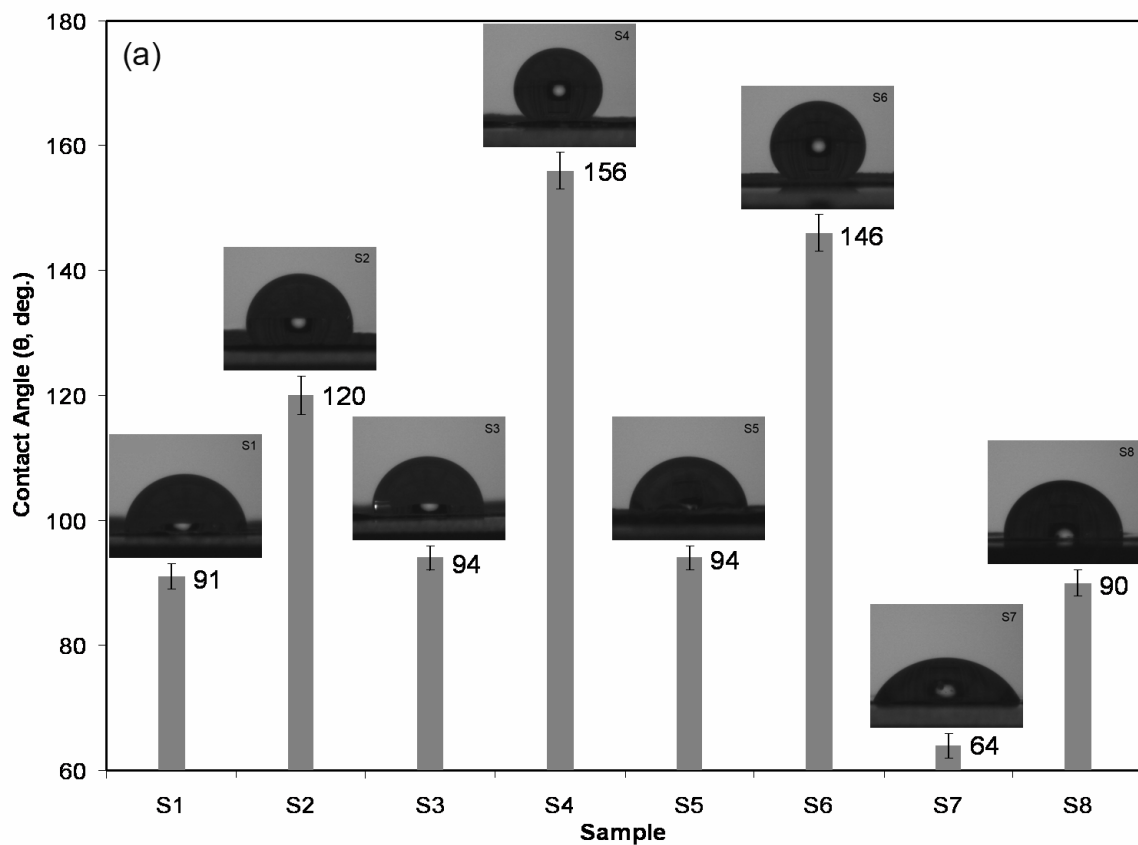
Figure 8. (a) Comparison of the water contact angles and the shapes of the water droplets on the NC Ni surfaces. S1: NC Ni lotus leaf replica; S2: S1 after the PFPE solution treatment; S3: NC Ni lotus leaf replica after the 120 s SED process; S4: S3 after the PFPE solution treatment; S5: NC Ni lotus leaf replica after the 300 s SED process; S6: S5 after the PFPE solution treatment; S7: NC Ni deposited on smooth replica surface; S8: S7 after the PFPE solution treatment. (b): An optical image of a large water droplet on the surface of S4.
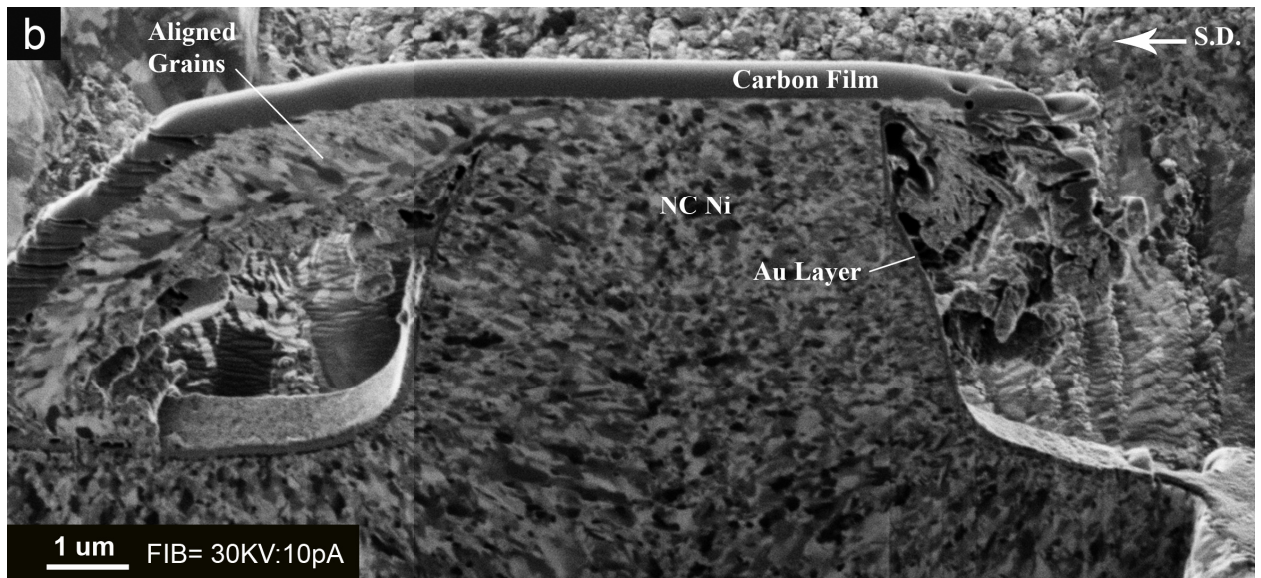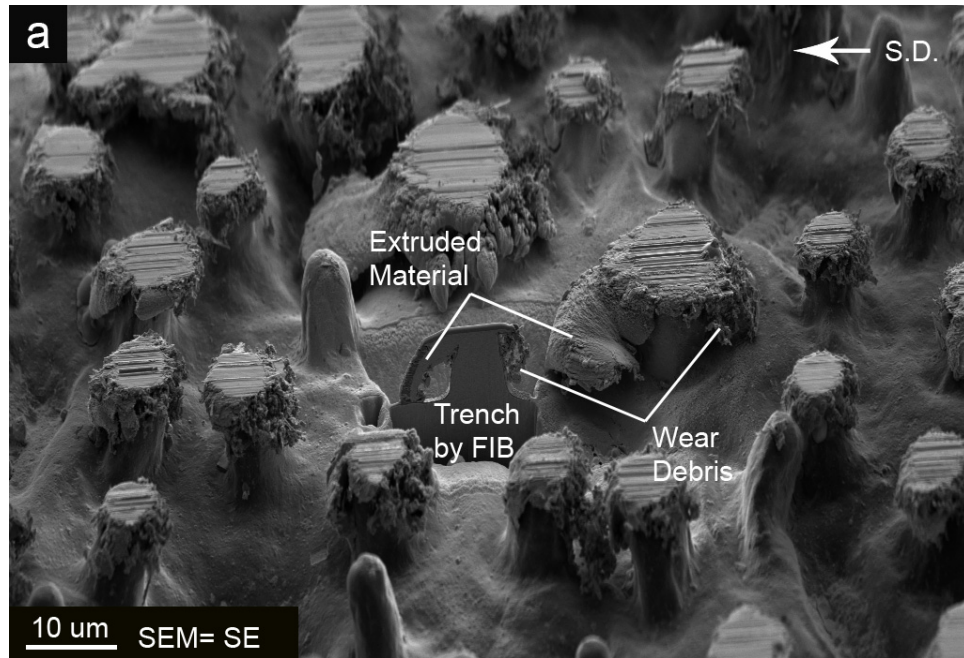
Figure 9. (a): An SE image of the wear track formed on the NC Ni lotus leaf replica (S1) after sliding for 500 cycles. A trench has been milled at the centre of this area to reveal a protuberance's cross-section parallel to the sliding direction for microstructural analysis by FIB. (b): A cross-sectional FIB image of the worn protuberance shown in (a).

174

(e) S5

(f) S6
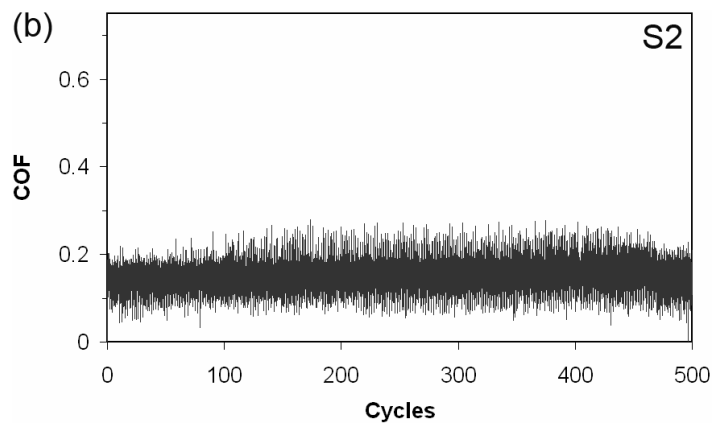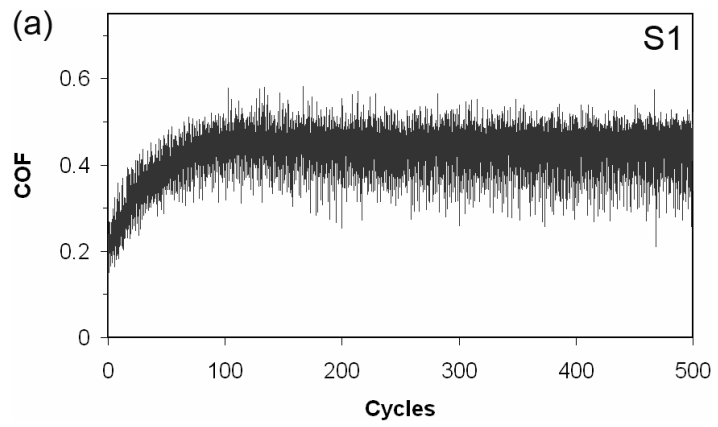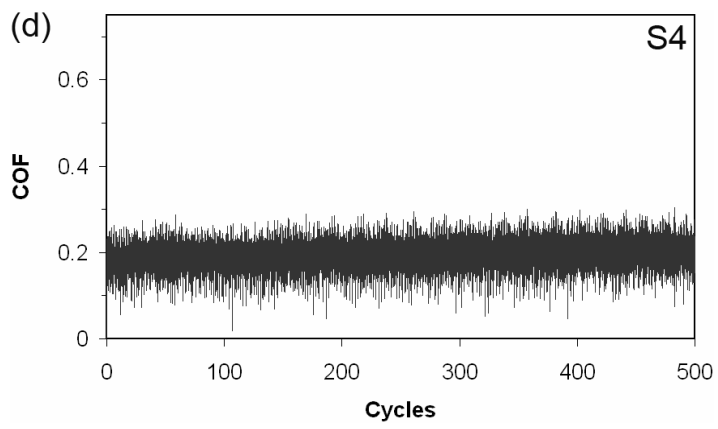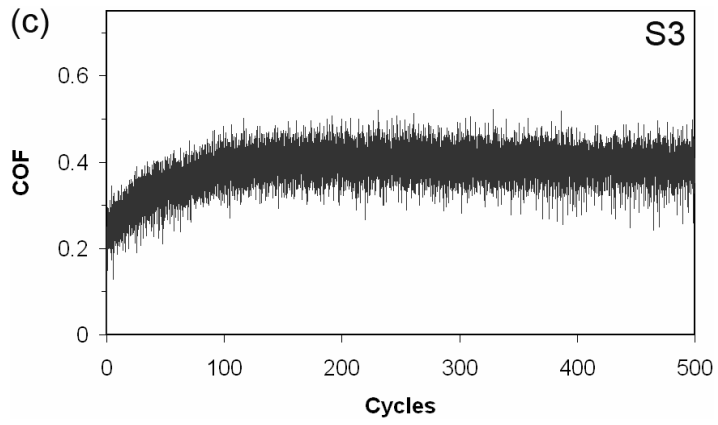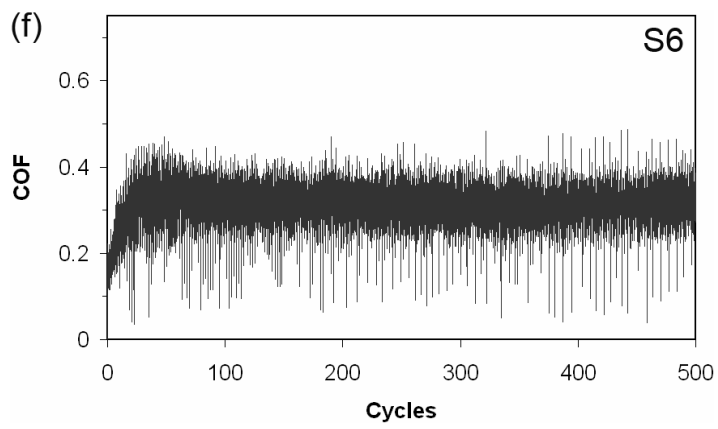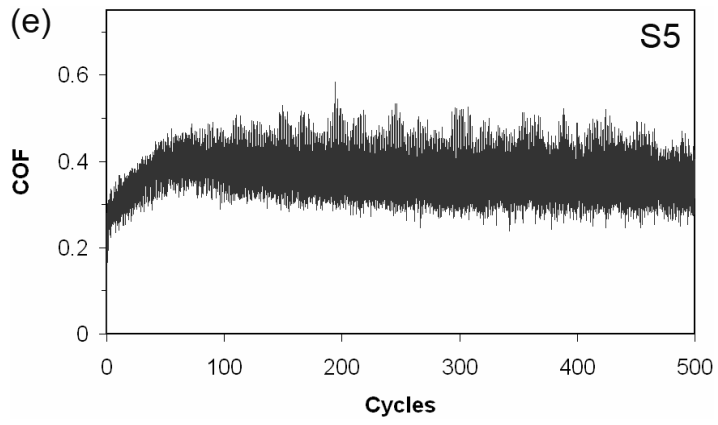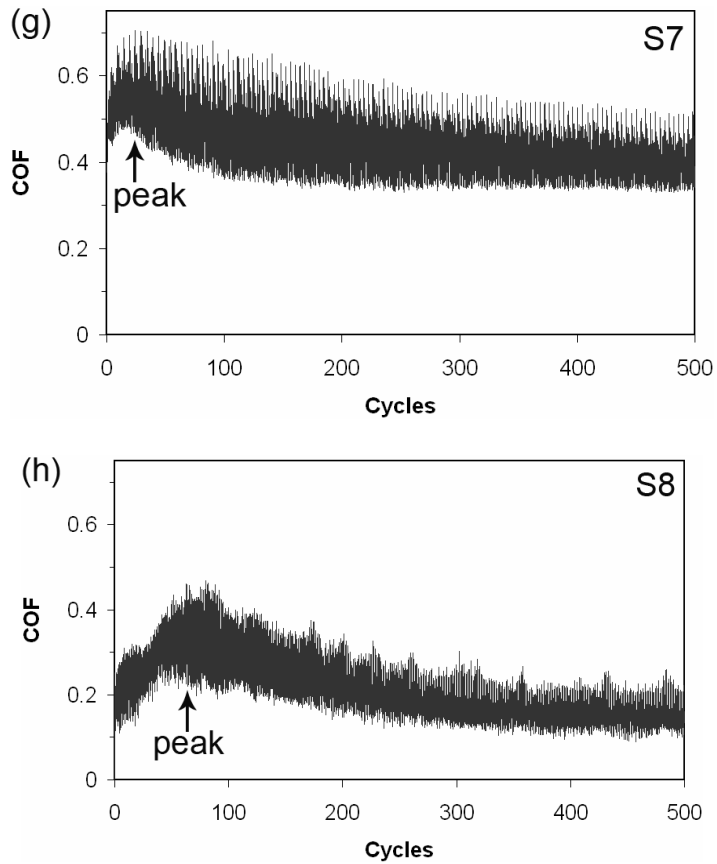
Figure 10. COF vs. sliding cycle curves of: (a): NC Ni lotus leaf replica (S1). (b): S1 after the PFPE solution treatment (S2). (c): NC Ni lotus leaf replica after 120 s of SED process (S3). (d): S3 after the PFPE solution treatment (S4). (e) NC Ni lotus leaf replica after 300 s of SED process (S5). (f): S5 after the PFPE solution treatment (S6). (g): NC Ni deposited on smooth replica surface (S7). (h): S7 after the PFPE solution treatment (S8).
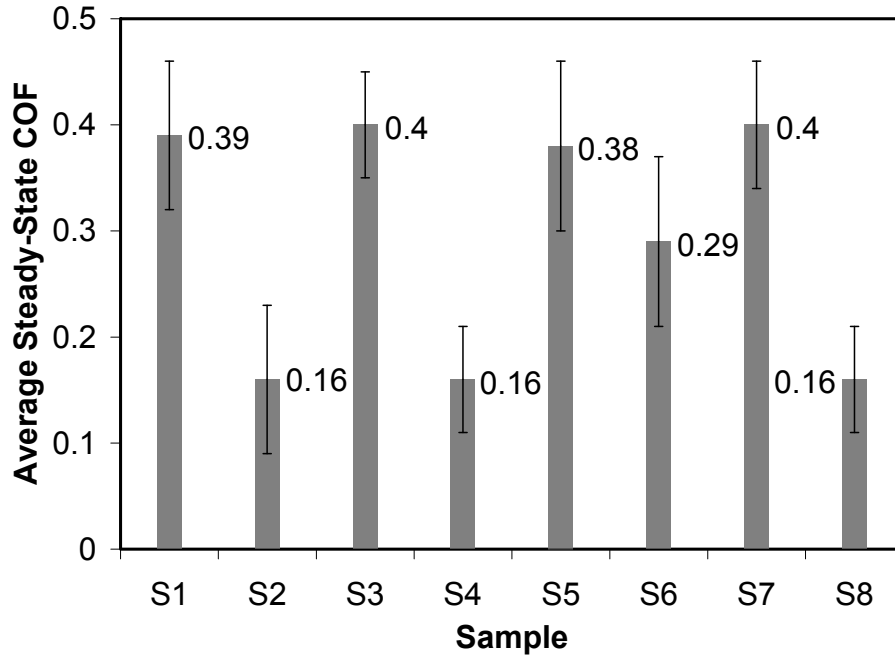
Figure 11. The average steady-state COFs of the NC Ni surfaces. S1: NC Ni lotus leaf replica; S2: S1 after the PFPE solution treatment; S3: NC Ni lotus leaf replica after the 120 s SED process; S4: S3 after the PFPE solution treatment; S5: NC Ni lotus leaf replica after the 300 s SED process; S6: S5 after the PFPE solution treatment; S7: NC Ni deposited on smooth replica surface; S8: S7 after the PFPE solution treatment.

CHAPTER 8

GENERAL DISCUSSIONS AND CONCLUSIONS

The objective of this dissertation was to develop new wear-resistant materials with superhydrophobic surfaces and low friction by combining the high strength and hardness of nanocrystalline (NC) materials with the surface textures found in biological systems. This was accomplished through the following steps:

i) Friction and wear properties of electrodeposited NC Ni and NC Co were investigated. For the NC Ni, microscopic processes leading to generation of wear debris and surface damage in different testing environments were characterized in detail. Surface deformation in the NC Ni was studied by performing nanoindentation tests. Additionally, effects of sliding speed and temperature on the friction and wear behaviour of the NC Ni were delineated in separate studies.

ii) Using replication and electrodeposition techniques, self-sustaining NC Ni replicas of the surface textures of a lotus leaf and a snake skin were fabricated for the reduction and control of friction.

iii) The surface texture of the NC Ni lotus leaf replicas was modified using a short-duration electrodeposition process, followed by a perfluoropolyether (PFPE) solution treatment, to increase hydrophobicity and to lower the friction of this NC metal.

The key conclusions arising from this dissertation are as follows:

1. In studying tribological properties of NC metals, attention must be given to the effects of testing environment. The role of the surface oxidation on the initial and steady-

state wear behaviour of NC Ni and NC Co was studied in this dissertation. In ambient atmosphere, the formation of continuous, oxidized tribolayers on top of the steady-state wear tracks prevented the ploughing of the NC Ni's surface by the counterface, resulting in an 18% lower peak coefficient of friction (COF), two orders of magnitude lower initial wear rate and a 77% lower steady-state wear rate compared to a microcrystalline (MC) Ni. In contrast, higher rate of oxidational wear in NC Co resulted in higher initial surface damage in this material compared to an MC Co. Once tribolayers formed on top of the contact surfaces, they reduced the steady-state COF and wear rate in the NC Co. Therefore, it can be concluded that for an NC metal with a hardness slightly higher than that of its MC counterpart (e.g., NC Co) the higher rate of surface oxidation, particularly during the initial stage of sliding, can result in larger surface damage. The negative effect of surface oxidation can be offset by the outstanding potential of grain boundaries in increasing the hardness of face centred cubic (FCC) metals like in the case of the NC Ni.

2. The grain-boundary-induced deformation mechanisms are more difficult to operate at higher strain rates, and thus in NC metals with a high density of grain boundaries, the surface damage and wear rate decrease significantly when the sliding speed increases. Based on this experimental observation, a modified Archard equation, in which the wear coefficient and the wear exponent were functions of sliding speed, was proposed to predict wear rates of NC Ni at various sliding speeds.

3. Increasing the sliding test temperature from 298 K to 493 K resulted in an increase in wear rate of more than two orders of magnitude and a 67% increase in the COF of the NC Ni coating, which was attributed to the activation of grain boundary sliding mechanism at the elevated temperature. Although reinforcing NC Ni with SiC

nanoparticles (NP SiC) did not result in any significant change in the NC Ni's hardness or wear rate at room temperature, it remarkably improved the NC Ni's high-temperature wear resistance. It was suggested that the recrystallization of new grains, as well as the grain boundary sliding deformation mechanism observed during the high-temperature sliding tests could possibly be hindered by the nanoparticles in the NC Ni-NP SiC composite coating.

4. Replicating the surface textures of biological samples, namely boa's skin and lotus leaf, on the NC Ni produced hard, durable surfaces with controlled and reduced frictional properties. The NC Ni replica of boa's skin displayed frictional anisotropy as a result of the asymmetric shape of the protrusions at the scales' ridges. The microscale protuberances in the NC Ni lotus leaf replica reduced the real area of contact and removed the wear debris particles from the contact surfaces simultaneously, eliminating the initial high COF peaks observed when smooth NC Ni films with the same microstructure and hardness were tested. It was showed that the transfer of the wear debris to the spaces between the protuberances prohibited the formation of oxidized tribolayers on the contact surfaces of the textured surface. Additionally, the successful development of a multi-level surface roughness (where a nanoscale surface texture was superimposed on a microscale structure of protuberances) with a low surface energy by using a selective electrodeposition followed by a PFPE solution treatment resulted in a low COF (0.16) and a high hydrophobicity (156°) similar to the natural leaf but on a much harder surface (4.42 GPa).

SUGGESTIONS FOR FUTURE WORK

1. The effects of surface oxidation, sliding speed and testing temperature on the tribological behaviour of other nanocrystalline (NC) materials including hexagonal close-packed (HCP) metals need to be investigated.

2. The microstructural instability of NC materials at high temperatures remains a significant disadvantage for these materials. It is suggested that the deformation and wear micromechanisms of NC materials at high temperatures be explored further to develop new strategies for strengthening these materials at elevated temperatures. More progress needs to be made on the reinforcement strategies by focussing on the nanoscale interactions between nanoparticles and NC grains.

3. It is suggested that the replication method developed in this dissertation be used for fabricating replicas of other biological surface textures to modify surface properties of NC materials. Along this line, reproductions of shark skin for reducing the friction, wings of butterfly and cicada for increasing the hydrophobicity, and dragonfly's eye for obtaining NC surfaces with antireflective properties are proposed.

4. The biotextured NC films described in this dissertation were originally developed for the microscale applications like micro-electro-mechanical systems (MEMS). New techniques need to be developed for the mass production of large NC sheets with biological surface textures for various industrial applications.

APPENDICES

APPENDIX A: MEASUREMENT OF THE WIDTH OF THE WEAR TRACK

A Wyko NT-1100 optical interferometer was used to obtain 2-D profiles at four locations around a circular wear track. The width of the track was then measured at each location, as shown in Figure A1, and the average of these measurements was recorded as the width of the wear track.
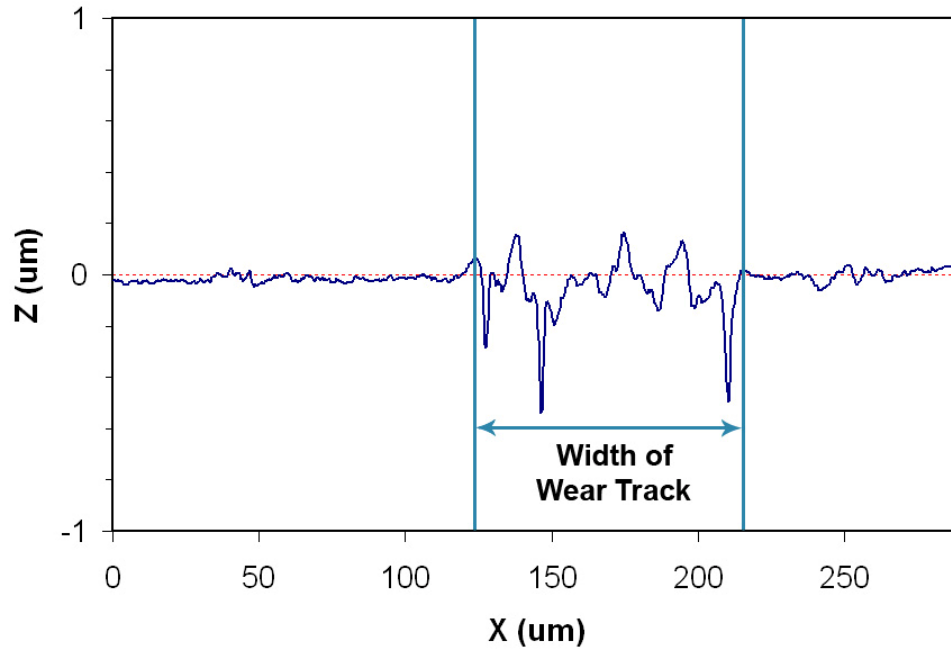

Figure A1. A typical 2-D profile of the wear track formed on NC Ni after 1000 sliding cycles in air.

APPENDIX B: CALCULATION OF ACTUAL RADIUS OF PROJECTED CONTACT AREA

Equations B1-B4 were used to determine the actual radius of the projected contact area, a_c', for both MC Ni and NC Ni at different loads. First the indentation contact depth, h_c, was determined using [B1]:

$$h_c = 0.25\left(h + 3h_i\right)$$
(B1)

where h is the indentation depth immediately before partial unloading and h_i is the indentation depth extrapolated to zero load along the linear fit of the upper one-third of the unloading curve [B2,B3]. Ignoring the effects of piling-up and sinking-in on the indentation geometry, the radius of the projected contact area can be calculated as [B4]:

$$a_c = \sqrt{2r_{ind}h_c - h_c^2}$$
(B2)

where r_{ind} is the indenter's radius. After complete unloading, the indentation contact depth, h_c, is replaced with the residual depth, h_f.

However, the piling-up and sinking-in of the material around the indentation point modify the real contact area. In order to account for this effect, a dimensionless parameter c^2 has been defined as [B4]:

$$c^2 = \frac{h_c'}{h_c} \cong \left(\frac{a_c'}{a_c}\right)^2 \qquad \begin{cases} c^2 > 1 \ \text{ for } \text{piling-up} \\ \\ c^2 < 1 \ \text{ for } \text{sinking-in} \end{cases}$$
(B3)

where h_c' is the actual contact depth, and a_c' is the actual radius of the projected contact area. Various equations have been used to relate c^2 to the strain hardening exponent, n [B5]. Hill et al. [B6] derived an analytical relation between c^2 and n using a nonlinear elastic constitutive model for the indented material:

$$c^2 = 2.5\left(\frac{2-n}{4+n}\right) \tag{B4}$$

Assuming $n = 0$ for both samples, Equation B4 gives $c^2 = 1.25$. It should be noted that frictional effects on the amount of piling-up / sinking-in have been neglected in Equation B4.

REFERENCES

[B1] J.H. Ahn, D. Kwon, J. Mater. Res. 16 (2001) 3170.

[B2] M.F. Doerner, W.D. Nix, J. Mater. Res. 1 (1986) 601.

[B3] W.C. Oliver, G.M. Pharr, J. Mater. Res. 7 (1992) 1564.

[B4] B. Taljat, T. Zacharia, Int. J. Solids Struct. 35 (1998) 4411.

[B5] H. Lee, J.H. Lee, G.M. Pharr, J. Mech. Phys. Solids 53 (2005) 2037.

[B6] R. Hill, B. Storakers, A.B. Zdunek, Proc. R. Soc. Lond. A436 (1989) 301.

APPENDIX C: COPPYRIGHT RELEASES FROM PUBLICATIONS

<u>Chapter 2</u>

License Number:	2178260489827
License date:	Apr 29, 2009
Licensed content publisher:	Springer
Licensed content publication:	Metallurgical and Materials Transactions A
Licensed content title:	Friction and Wear Mechanisms of Nanocrystalline Nickel in Ambient and Inert Atmospheres
Licensed content author:	Mehdi Shafiei and Ahmet T. Alpas
Licensed content date:	Jul 1, 2007
Volume number:	38
Issue number:	7
Type of Use:	Thesis/Dissertation
Portion:	Full text
Number of copies:	4
Title of your dissertation:	Biotextured Nanocrystalline Materials with Superhydrophobic Surfaces and Controlled Friction and Wear
Estimated size (pages):	216

Chapter 3

Chapter 5

Dear Mr. Shafiei:

It is our pleasure to grant you permission to use ASME paper "Friction and Wear Behaviour of Nanocrystalline Cobalt," by Mehdi Shafiei, Ahmet T. Alpas, International Joint Tribology Conference 2007, Paper Number IJTC2007-44131, cited in your letter for inclusion in a Doctoral Thesis entitled <u>Biotextured Nanocrystalline Materials with Superhydrophobic Surfaces and Controlled Friction and Wear</u> to be published by University of Windsor/Library and Archives Canada. As is customary, we ask that you ensure full acknowledgment of this material, the author(s), source and ASME as original publisher on all printed copies being distributed.

Many thanks for your interest in ASME publications.

Sincerely,

Beth Darchi
Permissions & Copyrights
ASME, 3 Park Avenue
New York, NY 10016
T: 212-591-7700
F: 212-591-7841
E: darchib@asme.org

Chapter 6

License Number:	2161540913581
License date:	Apr 03, 2009
Licensed content publisher:	Elsevier
Licensed content publication:	Materials Science and Engineering: C
Licensed content title:	Fabrication of biotextured nanocrystalline nickel films for the reduction and control of friction
Licensed content author:	Mehdi Shafiei and Ahmet T. Alpas
Licensed content date:	1 December 2008
Volume number:	28
Issue number:	8
Pages:	7
Type of Use:	Thesis / Dissertation
Portion:	Full article
Format:	Both print and electronic
You are the author:	Yes
Are you translating?	No
Expected publication date:	May 2009
Elsevier VAT number:	GB 494 6272 12
Billing type:	Invoice
Company:	Mehdi Shafiei
Billing address:	Mechanical, Automotive & Materials Engineering
	University of Windsor
	Windsor, ON N9B 3P4
	Canada

PUBLICATIONS

Refereed Journal Publications

- M. Shafiei and A.T. Alpas, High-Temperature Friction and Wear Mechanisms of Nanocrystalline Nickel Composite Coatings, Surface & Coatings Technology (to be submitted).

- M. Shafiei and A.T. Alpas, Nanocrystalline Nickel Films with Lotus Leaf Texture for Superhydrophobic and Low Friction Surfaces, Applied Surface Science (to be submitted).

- M. Shafiei and A.T. Alpas, Fabrication of Biotextured Nanocrystalline Nickel Films for the Reduction and Control of Friction, Materials Science and Engineering C28 (2008) 1340-1346.

- M. Shafiei and A.T. Alpas, Effect of Sliding Speed on Friction and Wear Behaviour of Nanocrystalline Nickel Tested in an Argon Atmosphere, Wear 265 (2008) 429-438.

- M. Shafiei and A.T. Alpas, Friction and Wear Mechanisms of Nanocrystalline Nickel in Ambient and Inert Atmospheres, Metallurgical and Materials Transactions A38 (2007) 1621-1631.

Refereed Conference Publications

- M. Shafiei and A.T. Alpas, Superhydrophobic Nanocrystalline Nickel Films Inspired by Lotus Leaf, Proceedings of the 2008 Materials Research Society Fall Meeting, Boston, MA, USA, December 2008 (in press).

- M. Shafiei and A.T. Alpas, Friction and Wear Behaviour of Nanocrystalline Cobalt, Proceedings of the STLE/ ASME International Joint Tribology Conference, San Diego, CA, USA, October 2007, Paper # 44131.

- M. Shafiei and A.T. Alpas, Anisotropic Frictional Properties of a Copper Film Replica of Snake Skin with Nanoscale Texture, Proceedings of the 2nd Vienna International Conference on Micro- and Nanotechnology, Vienna, Austria, March 2007, 323-326.

- M. Shafiei and A.T. Alpas, Friction and Wear Behaviour of Nanocrystalline Nickel, Proceedings of the World Tribology Congress III, Washington, DC, USA, September 2005, Paper # 64315.

VITA AUCTORIS

Mehdi Shafiei was born in 1978 in Isfahan, Iran. He earned a B.A.Sc. degree from the Isfahan University of Technology in 2001 and an M.A.Sc. degree from the Amirkabir University of Technology (Tehran Polytechnic) in 2004, both in Materials Engineering. He is currently a candidate for the Ph.D. degree in Engineering Materials at the University of Windsor and hopes to graduate in June 2009.